Engineering and Applied Science Theses & Dissertations

McKelvey School of Engineering

Spring 5-15-2019

Ultrasound-guided Optical Techniques for Cancer Diagnosis: System and Algorithm Development

Atahar Kamal Mostafa
Washington University in St. Louis

Follow this and additional works at: https://openscholarship.wustl.edu/eng_etds

Part of the Biomedical Engineering and Bioengineering Commons

Recommended Citation

WASHINGTON UNIVERSITY IN ST. LOUIS

Department of Biomedical Engineering

Dissertation Examination Committee:
Quing Zhu, Chair
Mark Anastasio
Adam Bauer
Hong Chen
Yuan-Chuan Tai

Ultrasound-guided Optical Techniques for Cancer Diagnosis: System and Algorithm
Development

By

Atahar Kamal Mostafa

A dissertation presented to
The Graduate School
of Washington University in
partial fulfillment of the
requirements for the degree
of Doctor of Philosophy

May 2019
St. Louis, Missouri

Table of Contents

List of Figures

completion of cycle 1, but was unchanged in size from the end of cycle 2 to before surgery. Right panel: tHb concentration maps obtained at the corresponding time points. Each map shows six sub-images marked as slice 1 to 6 and each sub-image shows spatial x and y distribution (9 cm by 9 cm) of tHb concentration reconstructed from 0.5 cm to 3.0 cm depth range from the skin surface. The spacing between the sub-images in depth is 0.5 cm. The color bar is tHb in micromoles per liter. The tHb reduced from 83.3 mol/L measured before treatment to 69.0, 55.3, 37.9 mol/L measured before completion of cycle 1, cycle 2, and cycle 3. A reduction of 17.2%, 33.6%, 54.5% occurred at the end of cycle 1, 2 and 3, respectively. The hemoglobin level remains unchanged to the end of the treatment before surgery. This patient had a complete pathologic response with no residual tumor, Miller-Payne grade 5. 30

List of Tables

Acknowledgments

I like to express my gratitude to Professor Quing Zhu for her guidance, support and patience. Her enthusiasm and dedication towards cancer research motivated me to do my best for the technology development. Along with the academic guidance, I found her very kind and supportive at any of my difficult situations in last five years. I am sincerely thankful to her for all her help and support.

I also like to thank my dissertation committee members Mark Anastasio, Yuan-Chuan Tai, Hong Chen and Adam Bauer for their help and guidance during my Ph.D.

I also like to acknowledge the support that I have received from my friends and colleagues from Ultrasound and Optical Imaging Laboratory. I want to specifically thank to Hamed Vavadi, Hai Li, Feifei Zhou, K M Shihab Uddin, Guang Yang, Eghbal Amidi for their constant support and guidance; without their support it would be impossible for me to complete this research.

<div align="right">Atahar Kamal Mostafa</div>

Washington University in St. Louis

May 2019

This dissertation is dedicated to my wife Iffat Mahmud, my mother F.J.A. Sultana Begum, and

my father Md. Golam Mostafa for their unconditional love and supports.

ABSTRACT OF THE DISSERTATION

Ultrasound-guided Optical Techniques for Cancer Diagnosis: System and Algorithm

Development

By

Atahar Kamal Mostafa

Doctor of Philosophy in Biomedical Engineering

Washington University in St. Louis, May, 2019

Dr. Quing Zhu, Chair

Worldwide, breast cancer is the most common cancer among women. In the United States alone, the American cancer society has estimated that there will be 271,270 new breast cancer cases in 2019, and 42,260 lives will be lost to the disease. Ultrasound (US), mammography, and magnetic resonance imaging (MRI) are regularly used for breast cancer diagnosis and therapy monitoring. However, they sometimes fail to diagnose breast cancer effectively. These shortcomings have motivated researchers to explore new modalities. One of these modalities, diffuse optical tomography (DOT), utilizes near-infrared (NIR) light to reveal the optical properties of tissue. NIR-based DOT images the contrast between a suspected lesion's location and the background tissue, caused by the higher NIR absorption of the hemoglobin, which characterizes tumors. The limitation of high light scattering inside tissue is minimized by using ultrasound image to find the tumor location.

This thesis focuses on developing a compact, low-cost ultrasound guided diffuse optical tomography imaging system and on improving optical image reconstruction by extracting the tumor's location and size from co-registered ultrasound images. Several electronic components have been redesigned and optimized to save space and cost and to improve the user experience. In

terms of software and algorithm development, manual extraction of tumor information from ultrasound images has been replaced by using a semi-automated ultrasound image segmentation algorithm that reduces the optical image reconstruction time and operator dependency. This system and algorithm have been validated with phantom and clinical data and have demonstrated their efficacy. An ongoing clinical trial will continue to gather more patient data to improve the robustness of the imaging algorithm.

Another part of this research focuses on ovarian cancer diagnosis. Ovarian cancer is the most deadly of all gynecological cancers, with a less than 50% five-year survival rate. This cancer can evolve without any noticeable symptom, which makes it difficult to diagnose in an early stage. Although ultrasound-guided photoacoustic tomography (PAT) has demonstrated potential for early detection of ovarian cancer, clinical studies have been very limited due to the lack of robust PAT systems.

In this research, we have customized a commercial ultrasound system to obtain real-time co-registered PAT and US images. This system was validated with several phantom studies before use in a clinical trial. PAT and US raw data from 16 ovarian cancer patients was used to extract spectral features for training and testing classifiers for automatic diagnosis. For some challenging cases, the region of interest selection was improved by reconstructing co-registered Doppler images. This study will be continued in order to obtain quantitative tissue properties using US-guided PAT.

1 Introduction to Cancer Imaging

1.1 Introduction

In modern medical practice, imaging is essential in diagnosing disease and monitoring treatment response. Ultrasound, MRI, X-ray, and nuclear imaging are frequently used in hospital settings to image properties of the human body that are related to disease. All of these modalities use different methods to monitor the physical or functional properties of tissue. Ultrasound employs high-frequency sound waves to image mechanical properties. MRI captures the spin of tissue molecules to provide functional information. X-ray imaging exploits different degrees of energy absorption to show the contrast among different tissues. Several categories of nuclear imaging use radiative contrast agents to observe the functionality of a particular organ. Although each of these imaging techniques has its particular strengths and drawbacks, singly and collectively they are widely used for cancer diagnosis and treatment monitoring.

In recent decades, optical imaging techniques in particular have become widely used for medical research and preclinical and clinical evaluations. Several optical imaging modalities, for example, optical coherence tomography, endoscopy, and spectroscopy, have become popular tools in the standard point of care. For cancer imaging, physicians and researchers take advantage of the high-resolution imaging capabilities of optical imaging. Diffuse optical tomography uses the light absorption of hemoglobin to provide a contrast between the background and cancer regions. It has already demonstrated considerable potential in cancer diagnosis and treatment monitoring. Photoacoustic tomography, another optical imaging technology which uses the light absorption of hemoglobin, combines its information with the physics of ultrasound propagation to obtain

both the mechanical and functional properties of the target tissue. This thesis discusses ultrasound-guided diffuse optical tomography and photoacoustic tomography and their applications in cancer imaging. It is organized into the following four chapters.

The reminder of this chapter briefly reviews medical imaging technologies, as well as diagnosis and treatment monitoring for breast and ovarian cancers.

Chapter 2 discusses the theory and application of ultrasound-guided diffuse optical tomography for breast cancer diagnosis, along with the system development and algorithm improvement for this technology.

Chapter 3 focuses on photoacoustic tomography, and includes the system's development and algorithms for diagnosis of ovarian cancer

Chapter 4 summarizes the above three chapters and discusses several remaining challenges at the frontiers of ultrasound-guided diffuse optical tomography and photoacoustic tomography.

1.2 Popular Medical Imaging Techniques

The ability to image the internal organs of the human body started with the discovery of the X-ray by Wilhelm Röntgen in 1895[1]. The absorption variations of X-ray energy in different tissues create contrast in an X-ray image, enabling the non-invasive imaging of human organs. Since its invention, X-ray imaging has proved a very reliable way to examine bones and diagnose diseases. Computed tomography (CT) is an advanced version of X-ray imaging in which a 3-D image is generated using multiple sources and detectors around the subject. Different contrast agents can also be used to increase the contrast among different tissues.

Ultrasound imaging gained popularity for medical applications in the late 1950s [2]. High-frequency sound waves are transmitted into the human body, and the reflected waves from tissue

boundaries are recorded using an ultrasound transducer for later processing and image reconstruction. Used mainly to image the mechanical properties of tissue, ultrasound imaging provides a low-cost and versatile means to examine internal organs. Ultrasound is non-invasive, does not require any contrast agent, and, when used prudently, does not have any adverse effect on the patient's body. Doppler imaging and elastography are variants of ultrasound imaging that examine different mechanical properties of organs and tissues.

MRI was developed in the last century after Raymond Damadian discovered the difference in the magnetic relaxation times of different tissues. In MRI, the subject is placed in a strong magnetic field and the spins of the molecules inside the tissue are aligned with the direction of the applied magnetic field. When the excitation is removed, the molecules release the absorbed energy at different rates, depending on their properties. The resulting contrast between different soft tissues provides very high resolution images that are suitable for cancer diagnosis[3].

Optical imaging, the most common form of medical imaging technology, is widely used in disease diagnosis, prevention, and treatment[4]. Endoscopy, optical coherence tomography, photoacoustic imaging, diffuse optical imaging, and spectroscopy are a few examples of medical optical imaging that have been developed in the last few decades. In the field of optical tomography, which is the focus of this dissertation, researchers have been advancing different techniques for the last two decades. Like ultrasound and X-ray, optical tomography provides a non-invasive means to examine the functionality of human organs and tissues. It uses the visible spectrum of electromagnetic waves and is implemented a wide variety of imaging techniques. Some optical imaging techniques are often combined with conventional imaging modalities to improve the performance of both imaging techniques.

1.3 Breast Cancer

Although breast cancer starts with a breast tumor, which presents as a lump inside the breast, not all breast lumps are life-threatening. The breast is a complex structure of fat, ducts, lobules, and stroma on top of the chest wall muscle. Still, any lump detected in the breast could be a possible life-threatening cancer. In the case of malignant tumors, cancer cells create abnormal breast lumps and, at a later stage, spread to other parts of the body through the ducts and bloodstream, in a process called metastasis. In metastasis stage, breast cancer becomes deadly. According to the National Breast Cancer Foundation, one in eight women will be diagnosed with breast cancer in their lifetime, making this the most common form of cancer among women [5]. It is estimated that every year more than 250,000 women are diagnosed with breast cancer and more than 40,000 die from it. So, early diagnosis and treatment are important to cure breast cancer and save lives [6].

Aggressive cell growth inside the breast causes malignant tumors. During tumor development, new micro blood vessels grow near the tumor zone to supply nutrition to the growing tissues, in a process called angiogenesis [7]. Because of angiogenesis, a malignant tumor site usually contains more hemoglobin than the surrounding tissue. However, in benign breast tumors the hemoglobin concentration is much lower because benign tumors are usually fluid-filled cysts or inflammations of lobules, mammary ducts, and stroma. Thus, they contain fewer microvessels than malignant tumors, and this difference can be utilized in breast cancer diagnosis using optical imaging modalities.

1.3.1 Breast Cancer Diagnosis and Treatment Monitoring

For breast cancer diagnosis and treatment monitoring, different imaging methods have been employed, including mammography, ultrasound imaging (US), and magnetic resonance imaging (MRI). Mammography is the most commonly used method for breast cancer diagnosis. However, in dense breasts it has relatively low sensitivity in early cancer diagnosis [3]. US provides better results than mammography but still provides many false positives and results in many unnecessary biopsies [8]. MRI has superior sensitivity in breast cancer detection and diagnosis, but its high cost makes it less useful for continuous treatment monitoring [9]. Dynamic contrast-enhanced MRI and positron emission tomography (PET) are very successful in treatment monitoring and have demonstrated their efficacy in early identification of breast cancer patients who are not responding to chemotherapy, but their equipment is expensive and they require the injection of contrast agents, which prevents them from being used repeatedly for monitoring patients during treatment[10][11].

Diffuse optical tomography (DOT) is a noninvasive imaging technique that uses near-infrared (NIR) light to assess the optical properties of tissue. NIR light has minimum absorption in water, so this technique can image up to 4 cm deep tissue in reflection geometry. The NIR wavelength range (~700 to 900 nm) is also optimally sensitive to both oxygenated and deoxygenated hemoglobin, which are two main chromophores of blood[12]. The hemoglobin concentration of tissue is related to angiogenesis, thus imaging the hemoglobin concentration provides useful information for breast cancer diagnosis. DOT has shown promising results in assessing breast cancer because of its sensitivity to oxygenated and deoxygenated hemoglobin [13]. Moreover, DOT also has demonstrated great potential in the assessment of tumor vasculature response to neoadjuvant chemotherapy [14]. DOT systems are portable, low cost, and require no contrast

agents, which make them an ideal alternative to currently used modalities for breast cancer diagnosis and monitoring in clinical settings.

1.4 Ovarian Cancer

Ovarian cancer has the lowest 5-year survival rate (50% or less) of all the gynecologic cancers [6]. Because of the high mortality associated with ovarian cancer, most women screened with an ovarian abnormality will undergo oophorectomy, even though they have at most a 2% risk of having ovarian cancer [15]. With the current screening and diagnostic abilities, most women (70%) with ovarian cancer will be diagnosed at Stage III or IV (widespread intra-abdominal disease), where the 5-year survival rate is less than 30%. By contrast, Stage I cancers have a 5-year survival rate of 80-90%. Hereditary ovarian cancer is diagnosed approximately 7-14 years earlier than cancer caused by sporadic mutations [16][17], which increases the potential cost/benefit ratio of its early diagnosis. Technology capable of reliably diagnosing ovarian cancer in earlier stages or prior to the development of invasive disease could reduce the high mortality and the large economic impact of this disease, particularly in high-risk women. Perhaps an even larger benefit would be that many women could avoid surgery because they could be assured that an ovarian mass was not cancer.

1.4.1 Ovarian Cancer Diagnosis

Because ovarian cancer lacks reliable symptoms and efficacious screening techniques, it is predominantly diagnosed in Stages III and IV. Currently, there is no single test for ovarian cancer, and the combination of serum marker CA125 screening (sensitivity of <50% [18],[19]), transvaginal ultrasound (US) (3.1% positive predictive value [20]), and pelvic exams (sensitivity of only 30%) yields low positive predictive value. CT scans have been studied extensively for

ovarian cancer detection, and multiple studies confirm that CT has a sensitivity of 45%, a specificity of 85%, a positive predictive value of 80%, and a negative predictive value of 50%. However, it is poor in the detection of metastases of < 2 cm. [21]. A 2003 publication [22] suggested that MRI was superior to CT for characterizing malignant features of an ovarian mass, and MRI is often used when US is not diagnostic. However, MRI is costly and typically used as a secondary imaging method. Positron emission tomography (PET), using 18F-FDG as a tracer, can detect malignant cancers with altered glucose metabolism and has been used for the assessment of lymph node involvement [23], evaluation of pretreatment staging, and treatment response and detection of cancer metastases. However, it has limited value in lesion localization in early stages of ovarian cancer because of the difficulty in distinguishing between the signal from early-stage cancers and the background uptake signals coming from the normal tissue [24]. Thus, we still need better techniques to interrogate the ovary and rule out cancer.

Photoacoustic tomography (PAT) is an emerging technique in which a short-pulsed laser beam penetrates diffusively into a tissue sample [25]. Transient acoustic waves, or photoacoustic waves, arise from thermoelastic expansion resulting from a transient temperature rise (on the order of 10mK), and are then measured around the sample by US transducers. The acquired photoacoustic waves are used to reconstruct, at ultrasound resolution, the optical absorption distribution, which reveals optical contrast that is directly related to the microvessel density of tumors or tumor angiogenesis [7]. If two optical wavelengths are used, photoacoustic waves can be used to reconstruct the distribution of tumor hypoxia, which is an important indicator of tumor metabolism and therapeutic response. These functional parameters are critical in the initial diagnosis of a tumor and the assessment of tumor response to treatment. Due to intense light scattering in tissue, to date, pure optical methods require direct contact with the ovary, which necessitates an invasive

access procedure [26]. Photoacoustic techniques minimize the deleterious effects of intense light scattering by measuring ultrasonic waves generated from the ovarian tissue; they, therefore, have great potential to non-invasively reveal tumor functional information. The penetration depth of PAT is scalable with ultrasound frequency. In the diagnostic frequency range of 3 to 8 MHz, the penetration depth in tissue can reach 4-5 cm using NIR light [27], which is comparable with the penetration depth used in conventional transvaginal US. Several studies have proven that photoacoustic imaging could be an effective tool for the early diagnosis of ovarian cancer [28].

References:

[1]   W. C. Röntgen, "On a New Kind of Rays," *Science*, vol. 3, no. 59, pp. 227–231, 1896.

[2]   P. G. Newman and G. S. Rozycki, "The History of Ultrasound," vol. 78, no. 2, pp. 179–195, 1998.

[3]   S. J. Lord *et al.*, "A systematic review of the effectiveness of magnetic resonance imaging (MRI) as an addition to mammography and ultrasound in screening young women at high risk of breast cancer," *Eur. J. Cancer*, vol. 43, no. 13, pp. 1905–1917, 2007.

[4]   J. C. Hebden, S. R. Arridge, and D. T. Delpy, "Optical imaging in medicine: I. Experimental techniques," *Phys. Med. Biol.*, vol. 42, no. 5, pp. 825–840, 1997.

[5]   "National Breast Cancer Foundation," *National Breast Cancer Foundation*, 2019. [Online]. Available: http://nbcf.org.au/about-national-breast-cancer-foundation/about-us/.

[6]   "American Cancer Society - Cancer Facts & Statistics," *American Cancer Society*, 2019. [Online]. Available: https://cancerstatisticscenter.cancer.org/#/.

[7]   B. P. Schneider and K. D. Miller, "Angiogenesis of Breast Cancer," *J. Clin. Oncol.*, vol. 23, no. 8, pp. 1782–1790, 2005.

[8]   W. A. Berg, A. I. Bandos, E. B. Mendelson, D. Lehrer, R. A. Jong, and E. D. Pisano, "Ultrasound as the primary screening test for breast cancer: Analysis from acrin 6666.," *J. Natl. Cancer Inst.*, vol. 108, no. 4, pp. 1–8, 2016.

[9]   S. L. Heller and L. Moy, "MRI Breast Screening Revisited," *J. Magn. Reson. Imaging Contrast-enhanced*, 2019.

[10] O. Humbert *et al.*, "18F-FDG PET-Derived Tumor Blood Flow Changes After 1 Cycle of Neoadjuvant Chemotherapy Predicts Outcome in Triple-Negative Breast Cancer," *J. Nucl. Med.*, vol. 57, no. 11, pp. 1707–1712, 2016.

[11] R. M. L. Warren *et al.*, "Can breast MRI help in the management of women with breast cancer treated by neoadjuvant chemotherapy?," *Br. J. Cancer*, vol. 90, no. 7, pp. 1349–1360, 2004.

[12] D. Boas *et al.*, "Imaging the Body with Diffused Optical Tomography," *IEEE Signal Process. Mag.*, vol. 18, no. 6, pp. 57–75, 2001.

[13] Q. Zhu *et al.*, "Early-Stage Invasive Breast Cancers : Potential Role of Optical Tomography with US Localization Methods : Results :" *Radiology*, vol. 256, no. 2, pp. 367–378, 2010.

[14] Q. Zhu *et al.*, "Identifying an early treatment window for predicting breast cancer response to neoadjuvant chemotherapy using immunohistopathology and hemoglobin parameters," *Breast Cancer Res.*, vol. 20, no. 1, pp. 1–17, 2018.

[15] "Clinical Summary: Cervical Cancer: Screening - US Preventive Services Task Force," *U.S. Department of Health and Human Services*, 2018. [Online]. Available:

https://www.uspreventiveservicestaskforce.org/Page/Document/ClinicalSummaryFinal/cervical-cancer-screening.

[16]   L. Mæhle *et al.*, "High risk for ovarian cancer in a prospective series is restricted to BRCA1/2 mutation carriers," *Clin. Cancer Res.*, vol. 14, no. 22, pp. 7569–7573, 2008.

[17]   D. Morgan, H. Sylvester, F. L. Lucas, and S. Miesfeldt, "Cancer prevention and screening practices among women at risk for hereditary breast and ovarian cancer after genetic counseling in the community setting," *Fam. Cancer*, vol. 8, no. 4, pp. 277–287, 2009.

[18]   V. Nossov *et al.*, "The early detection of ovarian cancer: from traditional methods to proteomics. Can we really do better than serum CA-125?," *Am. J. Obstet. Gynecol.*, vol. 199, no. 3, pp. 215–223, 2008.

[19]   J. Tammela and S. Lele, "New modalities in detection of recurrent ovarian cancer," *Curr. Opin. Obstet. Gynecol.*, vol. 16, no. 1, pp. 5–9, 2004.

[20]   M. Goozner, "Personalizing ovarian cancer screening.," *J. Natl. Cancer Inst.*, vol. 102, no. 15, pp. 1112–1113, 2010.

[21]   A. Shaaban and M. Rezvani, "Ovarian Cancer: Detection and Radiologic Staging," *Top. Magn. Reson. Imaging*, vol. 21, no. 4, pp. 247–259, 2010.

[22]   S. Funt and H. Hricak, "Ovarian Malignancies," *Top. Magn. Reson. Imaging*, vol. 14, no. 4, pp. 329–338, 2003.

[23]   R. E. Bristow, R. L. Giuntoli, H. K. Pannu, R. D. Schulick, E. K. Fishman, and R. L. Wahl, "Combined PET/CT for detecting recurrent ovarian cancer limited to retroperitoneal lymph nodes," *Gynecol. Oncol.*, vol. 99, no. 2, pp. 294–300, 2005.

[24]   R. Kumar, A. Chauhan, S. Jana, and S. Dadparvar, "Positron emission tomography in gynecological malignancies," *Expert Rev. Anticancer Ther.*, vol. 6, no. 7, pp. 1033–1044, 2006.

[25]   R. A. Kruger, P. Liu, Y. Fang, and R. Appledorn, "Photoacoustic ultrasound (PAUS)-reconstruction tomography," *Med. Phys.*, vol. 22, no. 10, pp. 1605–1609, 1995.

[26]   L. P. Hariri *et al.*, "Laparoscopic optical coherence tomography imaging of human ovarian cancer," *Gynecol. Oncol.*, vol. 114, no. 2, pp. 188–194, 2009.

[27]   J. Gamelin *et al.*, "Curved array photoacoustic tomographic system for small animal imaging," *J. Biomed. Opt.*, vol. 13, no. 2, pp. 024007-1–10, 2008.

[28]   S. Nandy *et al.*, "Evaluation of ovarian cancer: Initial application of coregistered photoacoustic tomography and US," *Radiology*, vol. 289, no. 3, 2018.

2 Ultrasound Guided Diffuse Optical Tomography

2.1 Diffuse Optical Tomography

Diffuse optical tomography (DOT) is a noninvasive technique which uses near-infrared (NIR) light to image optical properties of tissue. Due to the low water absorption in the NIR spectrum, the light can penetrate several centimeters inside soft tissue, i.e., breast and brain. Reflected or transmitted light measured at the tissue surface is used to reconstruct tomographic images[1][2]. DOT has demonstrated huge potential in cancer diagnosis and treatment monitoring by mapping hemoglobin concentration, which is related to vasculature content and tumor angiogenesis. It is possible to measure oxygenated, deoxygenated and total hemoglobin concentrations using multiple wavelengths. It also provides information regarding oxygen saturation, lipid and water concentration. These measurements could be effectively used to diagnose cancers vs. benign lesions and monitor treatment response because malignant tumors typically have higher hemoglobin content as compared to benign lesions and the hemoglobin changes differ between treatment responders and non-responders [3]–[7].

Diffuse optical tomography can be classified into three categories based on the type of source signal. They are: time domain, frequency domain, and direct current diffuse optical tomography [8]. Time domain DOT uses short light pulses and records the broadened reemitted signal. Amplitude modulated light is used as a source in frequency domain DOT and reemitted signal has reduced modulation depth. Carrier signal usually has several hundreds of MHz frequency for frequency domain DOT. Direct current or continuous wave DOT uses a fixed amplitude light source, which may be modulated with low-frequency carriers to improve noise performance. Time

domain DOT provides the most information; however, it requires an expensive detector and longer data acquisition time. Continuous wave DOT is low-cost but provides less information compared to the other two categories. Frequency domain DOT has optimum cost and performance in providing useful information, which makes it the popular choice among researchers who are working in the DOT domain.

DOT suffers from intensive light scattering inside the tissue and scattering causes uncertainty in reconstructed target location and inaccuracy of target quantification. These problems can be largely overcome by using other imaging techniques to guide the DOT for localization and reconstruction. US, Mammography, MRI guided DOT [7][9][10] have been investigated for various applications with a promising outcome. US-guided DOT has been developed by our group, and its utility in cancer diagnosis and treatment monitoring has demonstrated from several clinical studies [7][11].

2.2 Ultrasound-guided DOT

In the US-guided DOT approach, co-registered US images are captured and size and depth information of the tumor has to be incorporated in DOT reconstruction as a Region of Interest (ROI). A dual-zone mesh image reconstruction [12] is used to segment the ROI and background region with finer and coarse mesh sizes respectively. This scheme effectively reduces the total number of voxels with unknown optical absorption for imaging reconstruction, which is an underdetermined problem. Additionally, the total absorption of each voxel is reconstructed and divided by the voxel size to provide accurate absorption distributions. Since lesion absorption is higher than background in general, the total absorption, which is the product of voxel size and lesion absorption, of a lesion in a smaller voxel is about the same scale of total absorption of

background in a larger voxel. Therefore, the inversion is well-conditioned and converges in fewer iterations.

Absorption map of each wavelength was reconstructed using the dual-mesh approach with lesion parameters obtained from the co-registered US. Because the spatial resolution of diffused light is weaker than that of US, the ROI is chosen to be at least two to three times larger than that seen by using US in x-y dimensions. In addition, because the depth localization of diffused light is very poor, a tighter ROI in the depth dimension is set using the co-registered US. The weight matrix was computed using the fitted optical properties of each patient's normal contralateral breast. The scattered field U_{sd} measured from the lesion area was related to the internal absorption coefficients $\Delta\mu_a$ using the following equation:

$$[U_{sd}]_{m\times 1} = [W_L, W_B]_{m\times N}[M_L, M_B]^T{}_{N\times 1}$$

Where $m = s \times d$ the total number of source-detector pairs, W_L, W_B are the weight matrix for lesion and background regions respectively. M_L and M_B are the total absorption of the lesion and background respectively; can be expressed using the following two equations:

$$[M_L] = \left[\int_{1_L} \Delta\mu_a^\lambda(r')d^3r', \ldots\ldots \int_{N_L} \Delta\mu_a^\lambda(r')d^3r', \right]$$

And

$$[M_B] = \left[\int_{1_B} \Delta\mu_a^\lambda(r')d^3r', \ldots\ldots \int_{N_B} \Delta\mu_a^\lambda(r')d^3r', \right]$$

To obtain the unknown absorption information, the conjugate gradient method was used to solve the inverse problem formulated as minimize $\|U_{sd} - WM\|^2$, where $\|.\|$ is the Euclidean norm. Since this is an ill-posed problem due to the limited source and detection pairs and correlated diffused scattering field, the dual mesh technique utilizes the tumor location and size information extracted from co-registered US images for reconstruction to partially resolve this problem [12].

In our US-guided DOT, we are using four wavelengths that gives us the ability to estimate oxygenated (oxyHb) and deoxygeneated hemoglobin (deoxyHb) in the tumor region. We can estimate these two parameters for each voxels using the following equations:

$$
\begin{bmatrix} \mu_a^{\lambda_1}(r') \\ \mu_a^{\lambda_2}(r') \\ \mu_a^{\lambda_3}(r') \\ \mu_a^{\lambda_4}(r') \end{bmatrix} = \begin{bmatrix} \varepsilon_{Hb}^{\lambda_1} & \varepsilon_{HbO_2}^{\lambda_1} \\ \varepsilon_{Hb}^{\lambda_2} & \varepsilon_{HbO_2}^{\lambda_2} \\ \varepsilon_{Hb}^{\lambda_3} & \varepsilon_{HbO_2}^{\lambda_3} \\ \varepsilon_{Hb}^{\lambda_4} & \varepsilon_{HbO_2}^{\lambda_4} \end{bmatrix} \times \begin{bmatrix} deoxyHb(r') \\ oxyHb(r') \end{bmatrix}
$$

$$
\begin{bmatrix} deoxyHb(r') \\ oxyHb(r') \end{bmatrix} = \begin{bmatrix} \varepsilon_{Hb}^{\lambda_1} & \varepsilon_{HbO_2}^{\lambda_1} \\ \varepsilon_{Hb}^{\lambda_2} & \varepsilon_{HbO_2}^{\lambda_2} \\ \varepsilon_{Hb}^{\lambda_3} & \varepsilon_{HbO_2}^{\lambda_3} \\ \varepsilon_{Hb}^{\lambda_4} & \varepsilon_{HbO_2}^{\lambda_4} \end{bmatrix}^{-1} \times \begin{bmatrix} \mu_a^{\lambda_1}(r') \\ \mu_a^{\lambda_2}(r') \\ \mu_a^{\lambda_3}(r') \\ \mu_a^{\lambda_4}(r') \end{bmatrix}
$$

Where, $\mu_a^{\lambda_x}(r')$ are absorption coefficients obtained at imaging voxel r' for a particular wavelength (x=730,780,800,830 nm). $\varepsilon_y^{\lambda_x}$ (y=Hb or HbO$_2$) is wavelength dependent extinction coefficient. The total hemoglobin concentration and oxygen saturation can be estimated using the following two equations:

$$
totalHb(r') = deoxyHb(r') + oxyHb(r')
$$

$$Y\% = \frac{oxyHb(r')}{totalHb(r')}$$

2.3 Compact and Robust US-guided DOT System Design

Our group is working on ultrasound guided frequency domain diffused optical tomography for over two decades. Chen et al. reported the first generation of ultrasound guided DOT in 2001 [13]. This system used only two wavelengths as light sources. It has 12 sources and 8 detectors and guided by a 2-D ultrasound system, developed in the lab. This system provides promising results with phantom study thus motivated the lab to develop the next version of the US-DOT system.

In the second version of the US-DOT system [14], the lab made ultrasound system was replaced by a commercial ultrasound system, which is readily available in the examination site. A combined probe holder was designed to integrate the ultrasound guidance for optical imaging. This version was reported in 2006 and it has the option for selecting one of the three available modulation frequencies. This version used three different wavelengths for light delivery to improve the estimation of oxygenated hemoglobin information. This system was used in a clinical study and successfully employed for diagnosing benign and malignant breast tumors. A software developed using LabView programming controlled this 2nd generation DOT system.

Ten years after the second generation DOT, a new version of the DOT system was developed to improve the performance of the previous generation [11]. Since no obvious advantage was not achieved with the option with multiple modulation frequencies, in this version, only one modulation frequency (140 MHz) was used. To further improve the performance in oxygen saturation estimation, this system was equipped with a source of four different wavelengths. C++ based custom made software was used to control the data acquisition; however, data processing

option was not available in the custom software. A customized data acquisition board was also designed in the lab to provide better flexibility during the experiment. This system was used to collect almost 300 patient data from three different hospitals in Connecticut, USA. This data provides an effective means to evaluate the DOT system performance for neoadjuvant chemotherapy monitoring.
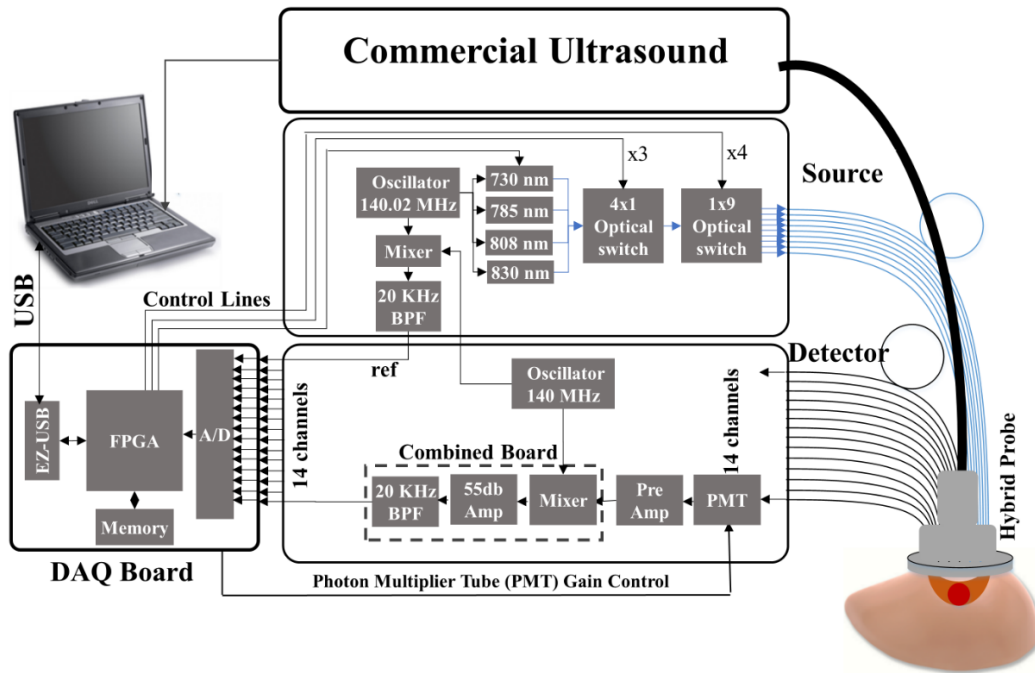
Figure 2. 1 Block diagram of the ultrasound-guided DOT system. The DOT system consists of source and detection subsystems controlled by a laptop through a FPGA.

To make the US-DOT technology suitable in the clinical settings, a new version of the US-DOT system was required to provide better user-friendliness and robust data acquisition ability. In 2018, we reported this latest version of the US-DOT system, which was intended to design for clinician [15]. In this prototype, four laser diodes of wavelengths 730, 785, 808 and 830 nm were sequentially switched by 4 x 1 and 1 x 9 optical switches to 9 source positions on a hand-held probe. Fourteen photomultiplier tubes (PMT) receive the reflected light from each source location simultaneously. After signal conditioning, the data is saved on the hard disk through the

16

customized data acquisition board. The entire data acquisition requires about 3 to 4 seconds.   The

sources and detectors were placed between 3.52 and 8.5 cm in the distance on the probe thus

provides us a reliable signal up to 5 cm depth.   The system used heterodyne detection with the

laser diodes modulated at 140.02 MHz, and the detected signals were mixed with the 140 MHz

reference signal to separate the 20 kHz signal for optical image reconstruction. The output of the

mixer at each channel was further amplified and filtered at 20 KHz before passing to analog to

digital converter (ADC).   An instrument case satisfying the medical safety standards was custom-

designed and manufactured by Nexus LLC. Figure 2.1 shows the diagram of the system and Figure

2.2 shows the clinical set-up at the Radiology Breast Imaging Clinics of Washington University

School of Medicine in St Louis.

Hybrid probe
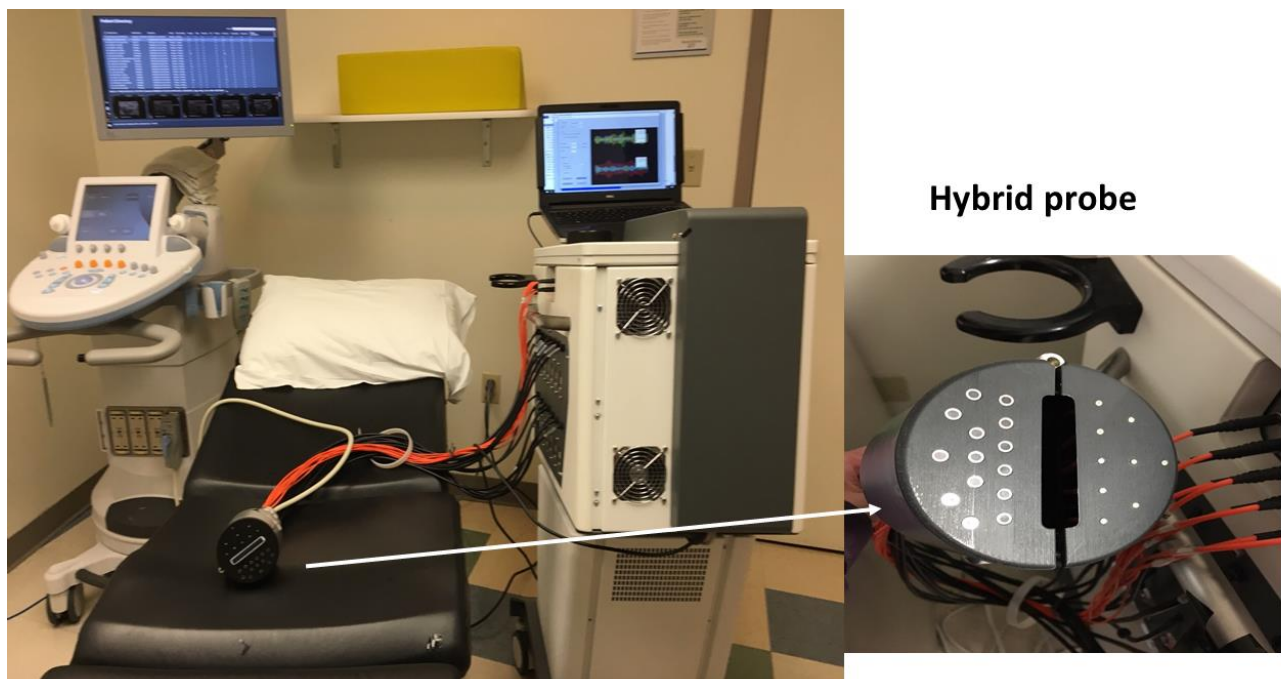
Figure 2. 2 Photograph of the US-guided DOT system used with a commercial US system. The system is used at the Radiology Department of Breast Imaging Clinics of Washington University School of Medicine in St Louis.

2.3.1 Electronic Component Design

Combined Mixer, Amplifier, and Filter

A custom-made detection circuit has been designed and built to miniaturize the detection subsystem of the fourth generation DOT system. As this system has high frequencies (140MHz and 140.02 MHz), the design needs to be robust to minimize the coherence noise at 20 kHz. The primary challenge of designing this combined board was to reduce the multi-frequency interferences. A three-layered printed circuit board (PCB) has been designed to meet this challenge. Inserting a ground layer between the top and bottom layer reduced the interference. All traces of a layer (top or bottom) carrier signal with a single frequency to provide better interference immunity. Grounded (GND) through holes has been placed on both sides of the signal carrying traces to provide better signal confinement. All these improvements result in a combined frequency mixer, second-stage amplifier, and the bandpass filter in one miniaturized board to reduce the size of the detection channel. A gain-adjustable second stage amplifier has been designed to provide flexibility in controlling the dynamic range of the detection system.
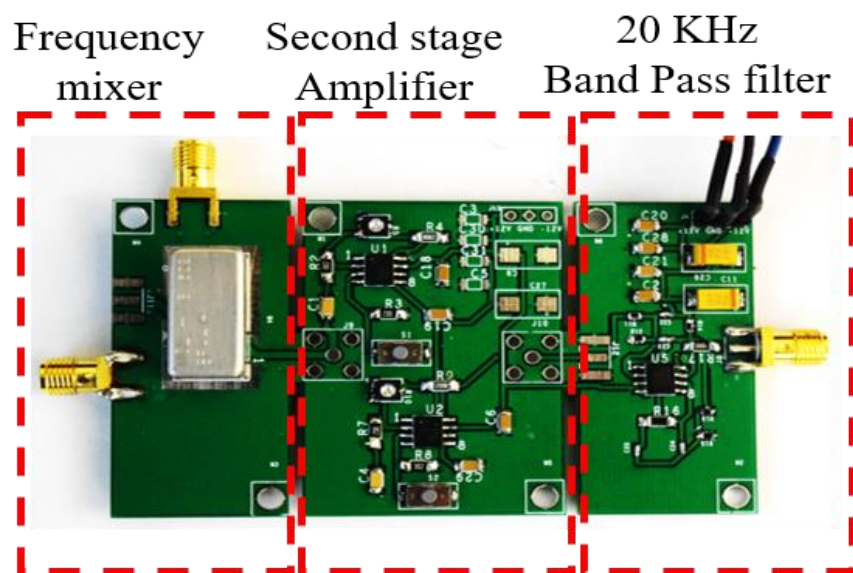
Figure 2. 3 Combined mixer, amplifier and filter was used in each detector channel

This combined board replaced three separate components (mixer, amplifier, and filter) of the detection channel of the 3rd generation DOT system. While the three components in the previous system occupied 22.5 cm X 3.0 cm X 5.5 cm in total, this combined board occupies only 10 cm X 3 cm X 5.5 cm. Therefore, 2887.5 cm^3 volume was reduced using this new combined board design for 14 detection channels. The lab designed filter also reduced the cost by $200 per channel. This new combined board design not only reduces the cost and size, but it also provides comparable noise performance. Noise performance has been measured after inserting this combined box for several days with different combinations of the system state. Overall, recorded single-channel noise was 7±8 mV, which is the same as the 3rd generation DOT system.
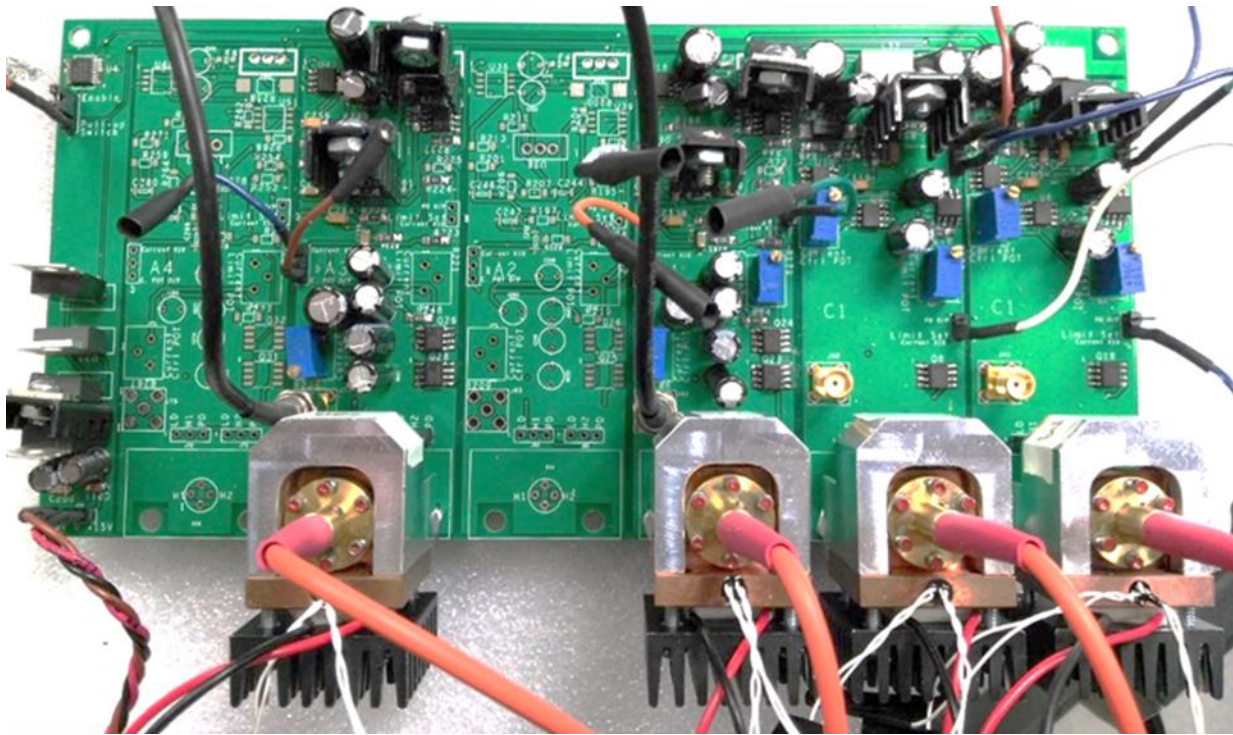
Figure 2. 4 Laser diode current driver for DOT source

Laser Diode Current Driver

The DOT system has two main blocks, source and detection subsystems. In our earlier prototypes, we used four units of Thorlab's DC current driver boards and four units of temperature-controlled

laser diode mounts with an AC modulation port to drive four laser diodes. These units were bulky and expensive. A custom-made laser diode driver board was designed to reduce the volume and cost of these components. This board can accommodate up to six laser diodes of type A or C with stable feedback control of DC current for each laser diode. Six built-in bias-tees, each with a radio frequency (RF) input provides AC modulation to each laser diode output. The outputs of the laser diodes were multiplexed via two optical switches (piezosystem jena) to 9 different positions on the hand-held probe. Four miniature pigtailed laser diodes with a thermal block from OZ Optics (LDPC-T3) were used as sources, and the temperature of the diodes was controlled using four units of control modules from Thorlabs (TCM1000T TEC).

PMT Gain Controller

In this prototype, we have used PMTs for detecting reemitted signals for their superior sensitivity and noise performance. Each PMT requires different gains to provide the same signal amplification in all receiving channels. In the older versions, a potentiometer was used for each PMT to provide different voltage to obtain the same signal output at each channel. This method makes data acquisition slow and reduces the user-friendliness of the system. This limitation was eliminated by designing a PMT gain controller board. This gain controller was designed using a 16-channel digital to analog converter (DAC), which accepts a digital signal from the control software through the custom designed data acquisition board, converted that signal into an analog voltage, and provides desired gains to each PMT.

2.3.2 Light Delivery and Probe Design

The ultrasound probe was located in the center of the probe to localize the lesion. In order to use PMT detectors in their maximum dynamic range and prevent the saturation when the source and

detection positions are very close, the source-detector distances have been optimized by locating nine sources on one side of the probe and the 14 detectors on the opposite side of the probe. Figure 2.2 insert shows the close-up view of the hand-held probe. A US transducer can be easily inserted into the combined probe holder before coregistered imaging and then unplugged after imaging. This handheld probe was designed and manufactured by an external contractor named Nexus LLC.

Figure 2. 5 PMT gain controller provides different gains to each PMT through control software

2.3.3 Data Acquisition Board

Same as the 3rd generation DOT system, we have used a custom-made Field Programmable Gate Array (FPGA) based DAQ board to reduce the DAQ size and improve its robustness. This miniaturized DAQ can accommodate up to 16 detection channels with two 8-channel ADC chips. In addition to data acquisition, this board is used for controlling the optical switches, laser diodes, and PMT gains. A laptop PC is used to communicate with the FPGA via a USB port. This customized data acquisition board was designed for the third generation DOT system by an external contractor. For the fourth generation system, it's FPGA firmware has been modified to add the control of laser diode diver and PMT gain control.

2.3.4 PC Based Control Software

Improvements in robustness and user-friendliness of the software for DOT are among the most critical steps toward extensive use in clinics. A new graphical user interface was developed using C++ with three modules. The first module is DAQ as discussed above. The second module consists of an automated system calibration [16]. The third module is for imaging reconstruction which incorporates our recently developed outlier removal and data selection method before reconstruction to eliminate the need for time-consuming data preprocessing [17]. It also includes a semi-automated method to select the region of interest (ROI) from co-registered ultrasound images and then uses the ROI for DOT image reconstruction [18]. This PC based control software was updated with the help of other lab members and reported in ref. [15].
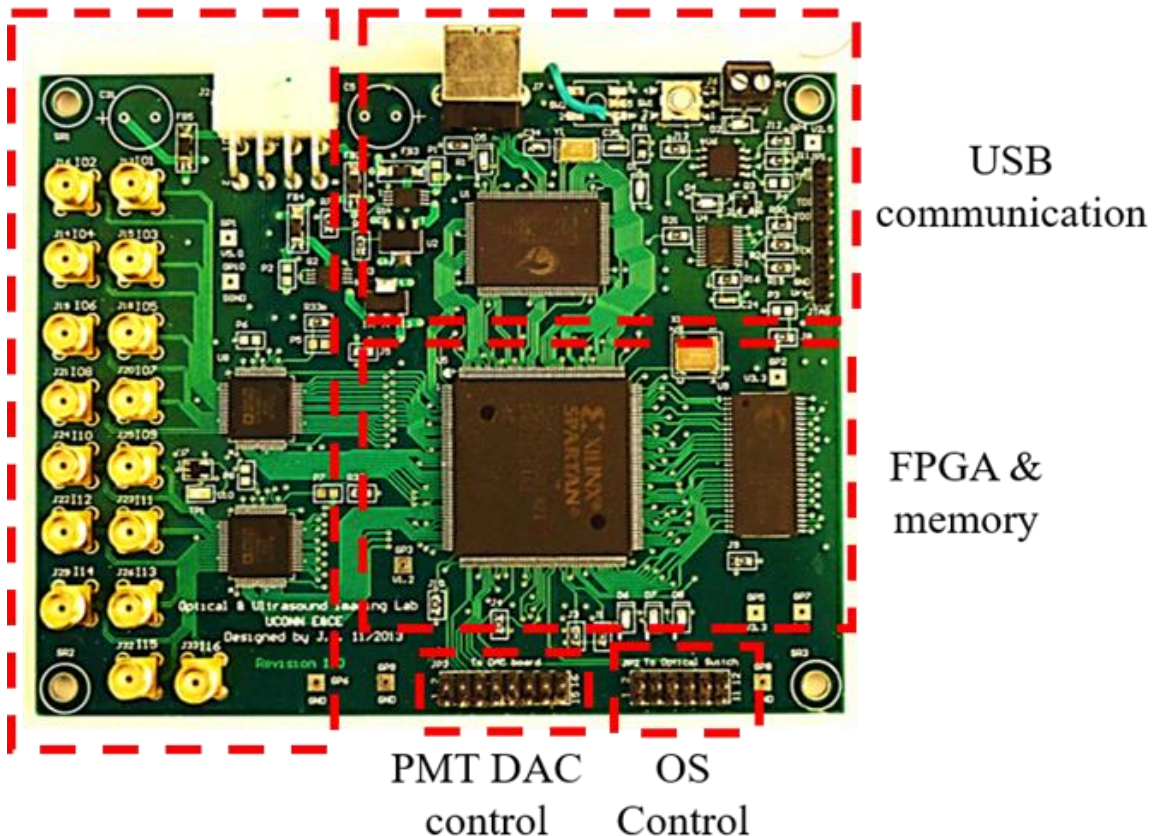
Figure 2. 6 Custom made 16 channel data acquisition board

2.3.5 System Evaluation

Several phantom studies have been performed to evaluate the performance of the newly developed system. These phantom studies were performed with the help of other lab members and reported in ref. [15]. After obtaining satisfactory performance, the system was moved to Washington University, School of Medicine for neoadjuvant chemotherapy monitoring. In the next two sections, system evaluation methods and results have been provided in details.

Phantom Study

Multiple phantom experiments have been designed to evaluate the performance of the system. Phantoms were placed in the Intralipid solution with an absorption coefficient of 0.015-0.02 cm^{-1} and reduced scattering coefficient of 7-8 cm^{-1}. In the first sets of experiments, the sensitivity of the system to differentiating high contrast and low contrast phantoms has been tested. Two sets of solid phantoms with an absorption coefficient of 0.11 and 0.23 cm^{-1} and reduced scattering coefficient the same as the Intralipid medium measured at 780 nm have been used. These phantoms of three different sizes (diameters of 1, 2, 3 cm) located at different depths include two small (1 cm) high and low contrast balls (SHC, SLC), two medium (2 cm) high and low contrast balls (MHC, MLC), and two large (3 cm) high and low contrast balls (LHC, LLC).

Figure 2.7 shows an example of reconstructed images of an SHC ball located at the 1.5 cm depth inside the Intralipid solution. The reconstructed maximum absorption coefficients of four wavelengths (730, 785, 808 and 830 nm) are 0.233, 0.238, 0.216, 0.211 respectively.

Figure 2.8 shows the reconstruction accuracy (in %) of the maximum reconstructed absorption coefficient of six solid high-contrast and low-contrast phantoms located at different depths. The

absorption coefficient at the top depths of the phantoms are shown in the Figure. For high contrast phantoms, our DOT system is accurate (89.4%) in the depth range of 1 to 2 cm for 1 cm diameter phantom (89.4%, SHC), and 1 to 2.5 cm for 2 cm (97.2%) and 3 cm (87.6%) diameter phantoms (MHC, LHC) . For low contrast phantoms, DOT system is accurate in the depth range of 0.5 cm to 2 cm for 1 cm diameter phantom (73%), (SLC), and 0.5 to 2.5 cm for 2 cm (69.5%) and 3 cm (72.1%) diameter phantoms (MLC, LLC). For high contrast phantoms located too close to the surface for less than 1 cm, the accuracy of reconstruction is lower (64.4%) due to lacking central sources in the combined probe.
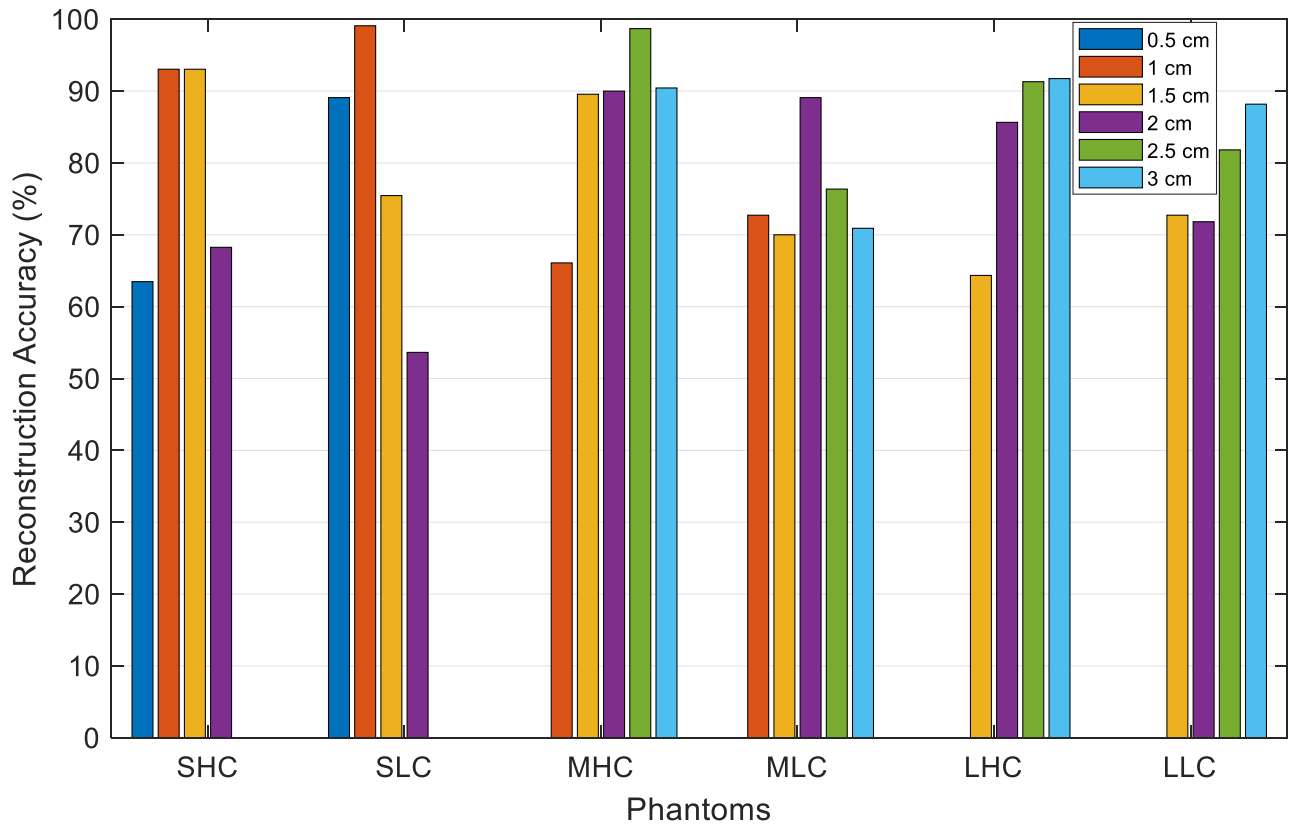
Figure 2. 7 Reconstruction accuracy (%) for six different phantoms located at different depths (depth of the top phantom positions are marked in the figure).
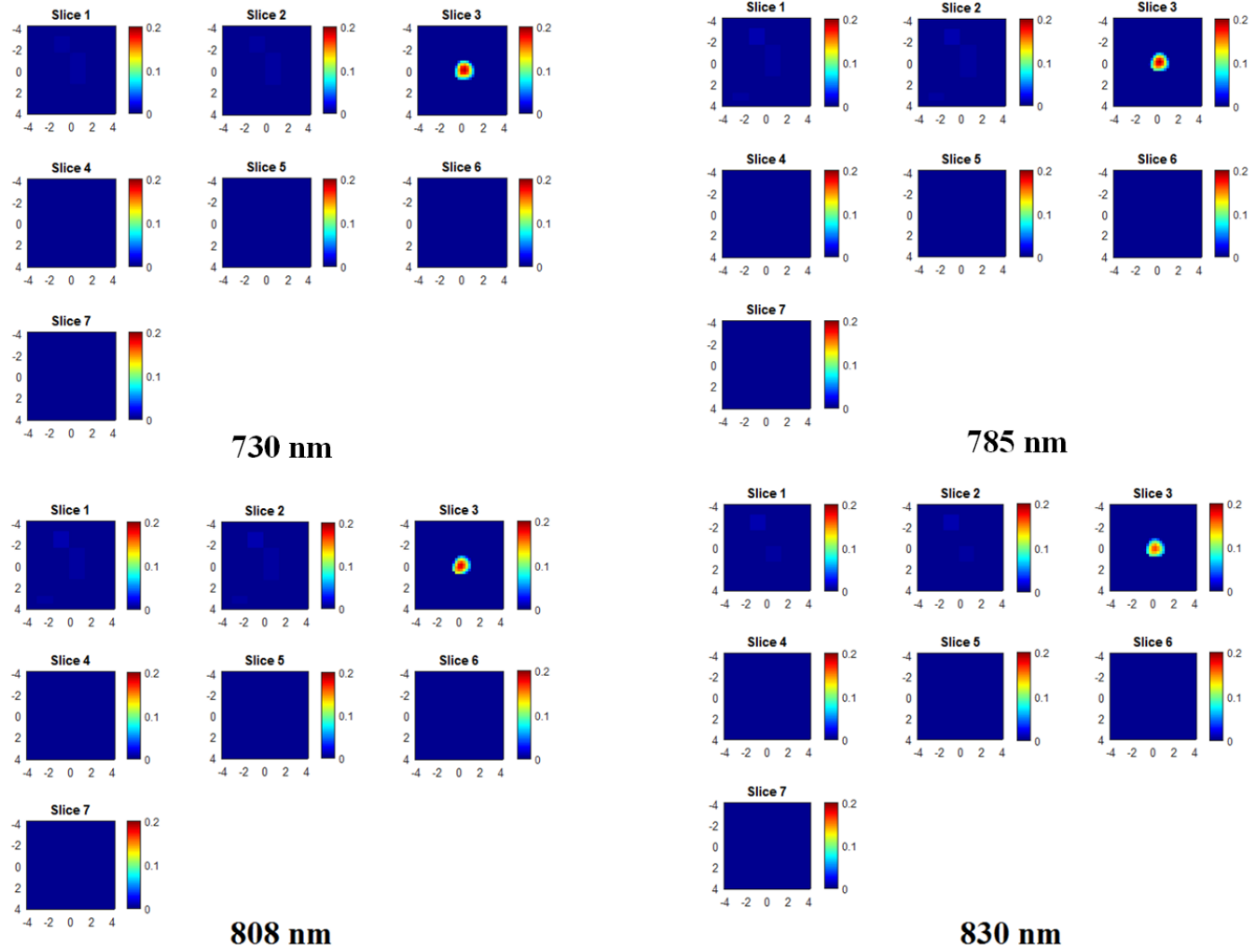
Figure 2. 8 Target absorption maps (730nm, 785nm, 808nm, 830nm) of a SHC phantom located at 1.5 cm depth. For each absorption map, 7 slices from 0.5 cm to 3.5 cm depth with 0.5 cm increment have reconstructed. The spatial dimensions of each slice are 9 cm by 9 cm. Color bar is the absorption coefficient in the unit of cm^{-1}.

To further evaluate the stability of the system over time, a series of experiments of multiple phantoms were measured at different days. One example of the stability result is presented in Figure 2.9. It shows the maximum reconstructed absorption coefficients of the 1 cm diameter high-contrast target measured at four optical wavelengths over time. The target was located at 1.0 cm in depth (target surface). The experiments have been repeated for five days and one measurement per day was performed. The average error for four wavelengths over five days was 5.4%, which is negligible considering the measurement errors of locating the targets precisely inside the Intralipid solution at the desired depths.
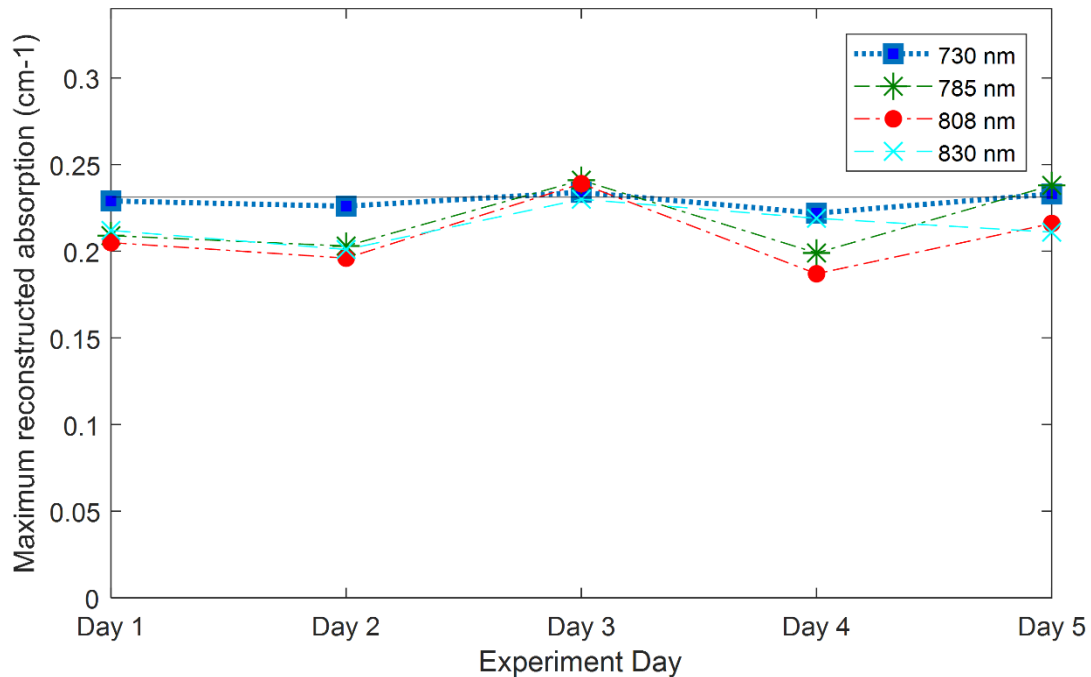
Figure 2. 9 Maximum reconstructed absorption coefficient of the small high-contrast phantom located at 1.0 cm depth (phantom top position) and imaged on different dates. The reconstructed absorption coefficients at 730,785, 808 and 830 nm are presented. The black dashed line represents the calibrated (true) absorption of the phantom.

Next, to evaluate the sensitivity of the system to oxygenated and deoxygenated hemoglobin, a hollow glass bulb filled with oxygenated and deoxygenated hemoglobin was used as a blood phantom. Hemoglobin solution was purchased from Instrumentation Laboratory (Multi-4, Level 2, Instrumentation Laboratory, MA) as the oxy-Hb sample. The Multi-4, Level 2 product

specification provided by Instrumentation Laboratory is total hemoglobin 139 g/L, with HbO2 percentage of approximately 97%. The de-oxygenated hemoglobin (Hb) solution is prepared by adding Sodium dithionite ($Na_2S_2O_4$) solution into the diluted oxygenated hemoglobin (HbO2). 0.05 g Sodium dithionite is dissolved in 0.5 mL, phosphate buffer saline (PBS) solution (with 10 μL mixed solution corresponding to 1 mg Sodium dithionite) with a pH of 7.4. We then add the Sodium dithionite solution into 3.5 mL HbO2 solution to prepare an Hb solution. Solution preparation and mixing were carried out on top of dry ice to keep the temperature at around 0 °C and slow down the speed of de-oxygenated Hb reacting with O_2. After sealing the glass ball, we incubated it at around 37 °C for 6 minutes for the Sodium dithionite to be effective. We calibrated the de-oxygenating process with a standard UV-Vis spectrometer (Varian Cary®, Agilent, US). For each ball and Hb solution, we finished our DOT measurements in less than 10 minutes. Figure 2.10 presents the experimental setup for the hemoglobin phantom experiments.
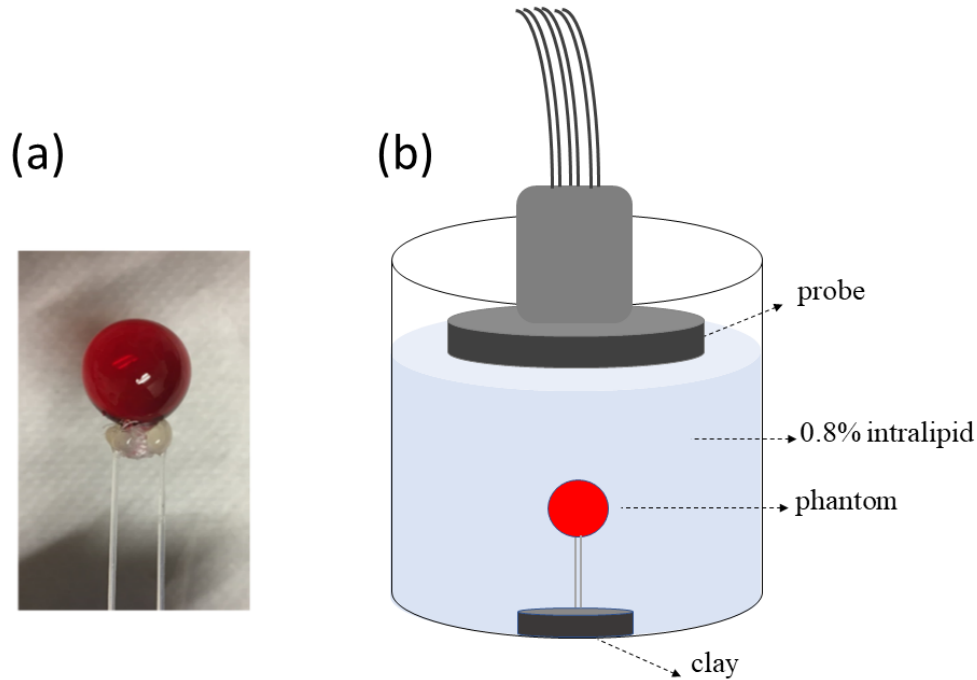
Figure 2. 10 (a) Glass ball (0.9 cm radius) filled with HbO2 solution and connected to holding fibers. (b) Sketch of the experimental setup

The images were reconstructed from measured data and the maximum reconstructed μ_a were compared with the calibrated values with the spectrometer. We used the maximum reconstructed μ_a to compute SO2. We analyzed the DOT-measured SO2 of the hemoglobin target at different calibrated SO2 values (~5-10% and ~97%) and Figure 2.11 shows the calculated spectrum from our US-guided DOT system which follows the literature data [18]. The results of the DOT system with four wavelengths are comparable with the data obtained from the spectrometer.
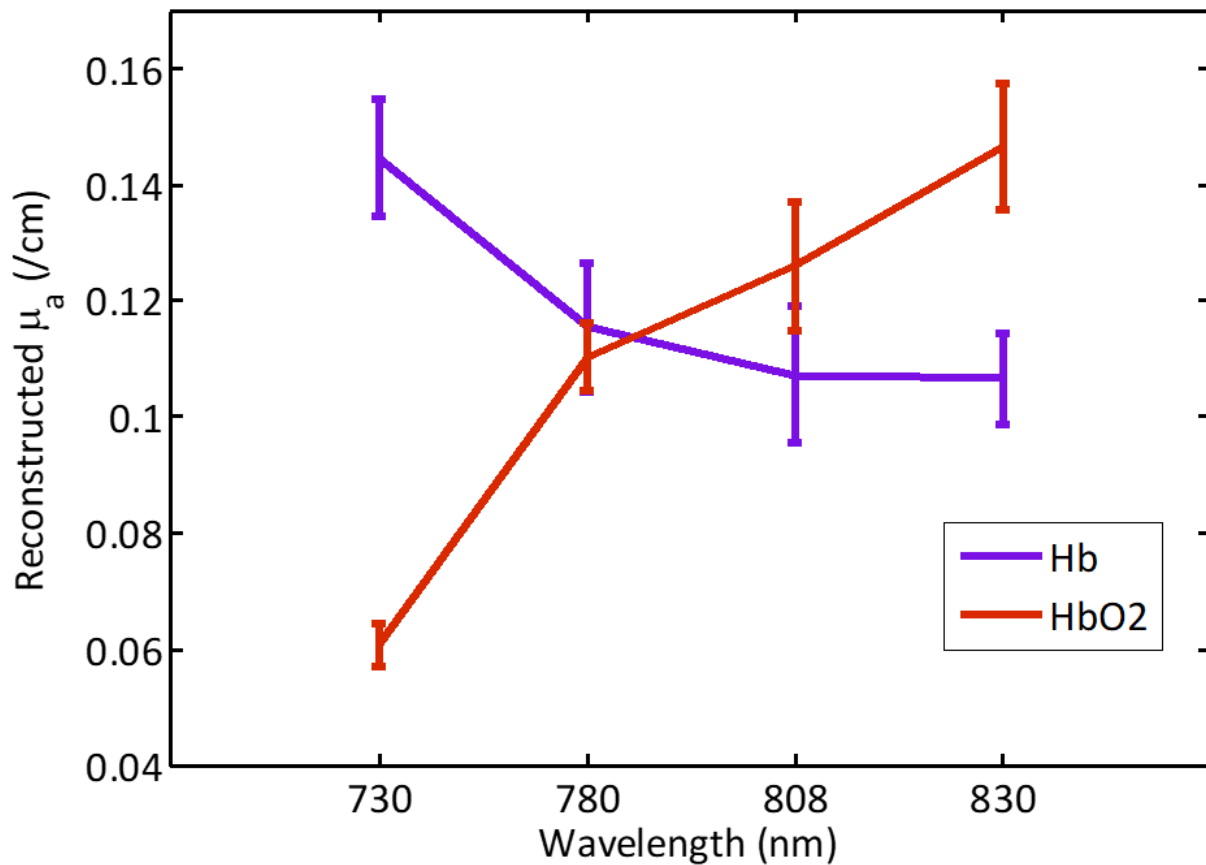
Figure 2. 11 Oxygenated and deoxygenated hemoglobin spectrum; reconstructed absorption coefficients using the DOT system.

To evaluate the performance of the system sensitivity to oxygenated and deoxygenated hemoglobin over time, five samples of oxygenated hemoglobin and five samples of deoxygenated

hemoglobin were prepared separately on different dates and each sample was measured with the spectrometer and then imaged with the ultrasound-guided DOT system.

Figure 2.12 shows the comparison of these five oxygenated and deoxygenated samples of calibrated value with the spectrometer and calculated value with the DOT system. It can be seen that the DOT measurements follow the spectrometer results closely.
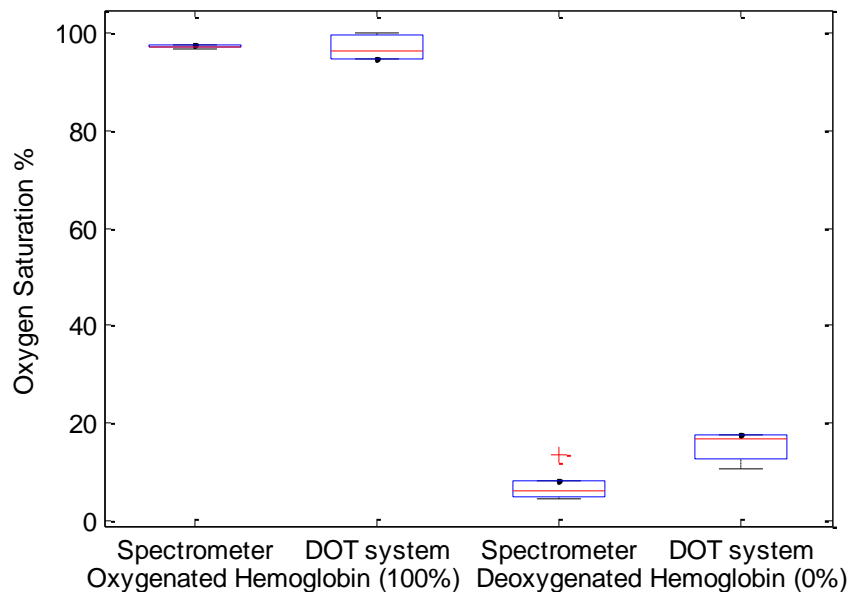
Figure 2. 12 Oxygenated and deoxygenated hemoglobin calibrated with the spectrometer and measured with the DOT system.

Clinical Results

The system is currently being used in patients undergoing neoadjuvant treatment at Washington University in St Louis. The study protocol was approved by the institutional review board and was HIPPA compliant. Written informed consent was obtained from patients. The final pathologic response was evaluated by the Miller-Payne system. In the Miller-Payne (MP) system, the patient pathologic response is divided into five grades based on a comparison of tumor cellularity between pre-neoadjuvant core biopsy and definitive surgical specimen. MP 1 and 2 are considered non-

responders, MP 3 judged to be partial responders, MP 4 regarded as the almost complete

pathological response (pCR), and MP 5 deemed a complete pathological response (pCR).
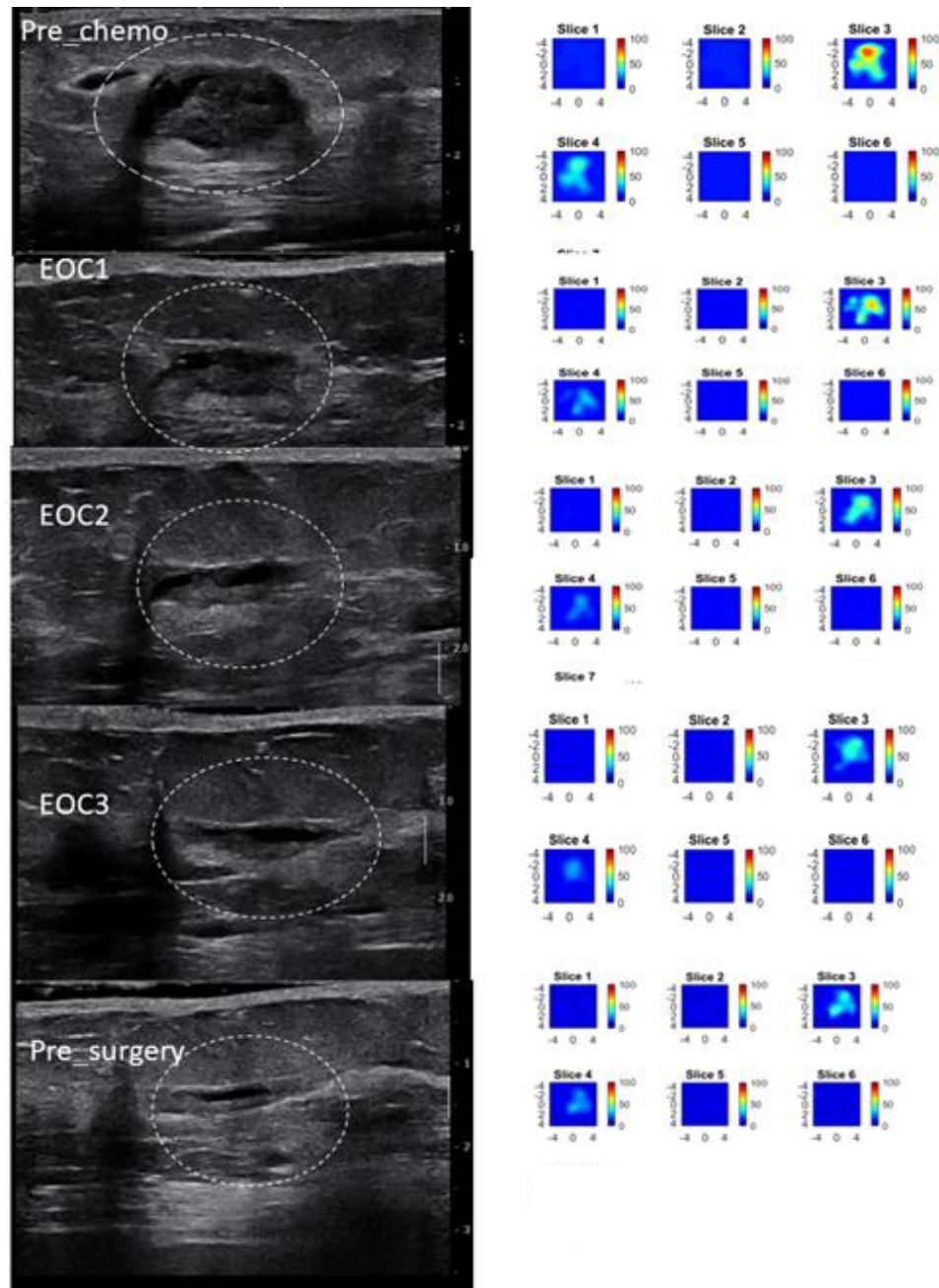
Figure 2. 13 pCR of a triple receptor negative breast cancer of a 51-year-old woman with a high grade invasive ductal carcinoma treated with carboplatin and docetaxel every three weeks for 6 cycles. Left panel: US images obtained at pretreatment, at the end of cycle 1 (EOC1), 2 (EOC2), 3 (EOC3), and before surgery. On US, the tumor manifest as an oval mass with well-defined margins, measuring 2.02 cm maximally before treatment, decreased mildly to 1.49 cm at the completion of cycle 1, but was unchanged in size from the end of cycle 2 to before surgery. Right panel: tHb concentration maps obtained at the corresponding time points. Each map shows six sub-images marked as slice 1 to

6 and each sub-image shows spatial x and y distribution (9 cm by 9 cm) of tHb concentration reconstructed from 0.5 cm to 3.0 cm depth range from the skin surface. The spacing between the sub-images in depth is 0.5 cm. The color bar is tHb in micromoles per liter. The tHb reduced from 83.3 mol/L measured before treatment to 69.0, 55.3, 37.9 mol/L measured before completion of cycle 1, cycle 2, and cycle 3. A reduction of 17.2%, 33.6%, 54.5% occurred at the end of cycle 1, 2 and 3, respectively. The hemoglobin level remains unchanged to the end of the treatment before surgery. This patient had a complete pathologic response with no residual tumor, Miller-Payne grade 5.

An example of conventional US and US-guided DOT generated Hb maps acquired throughout neoadjuvant treatment in a 51-year-old woman with a pCR is shown in Figure 2.13. The patient presented with a high grade (Nottingham Histologic Score 9/9) triple-receptor-negative, (i.e., ER-,PR-,Her2Neu-) invasive ductal carcinoma and was treated with carboplatin and docetaxel every three weeks for six cycles. US and US-guided NIR DOT was obtained prior to treatment, at the completion of cycles 1, 2, 3 and before surgery. US image showed a substantial decrease from baseline to the end of cycle 1, with more subtle size reduction during the remainder of neoadjuvant treatment. US-guided NIR DOT shows a progressive decline in total hemoglobin (tHb) concentration during the first three cycles, which correlated with a complete pathologic response of MP grade of 5.

2.4 Algorithm Improvement for US-guided Diffuse Optical Tomography

In the US-guided DOT approach, co-registered US images are captured and measurements of size and depth are then incorporated in DOT reconstruction as a Region of Interest (ROI). A dual-zone mesh image reconstruction is used to segment the ROI and background region with finer and coarse mesh sizes. This scheme effectively reduces the total number of voxels with unknown optical absorption for imaging reconstruction. Additionally, total absorption of each voxel is reconstructed and the total is then divided by the voxel size to provide absorption distributions. Because lesion absorption is higher than background in general, the total absorption, which is the product of voxel size and lesion absorption, of a lesion in a smaller voxel is about the same scale

of total absorption of background in a larger voxel. Therefore, the inversion is well-conditioned and converges in fewer iterations. Thus, US identified ROI is critical to guide dual-zone mesh DOT reconstruction.

Extraction of tumor size and location from US images has been done manually, which requires experienced users to make these measurements and slows down the DOT reconstruction. Similar to other medical imaging techniques, automatic US image segmentation is a challenging task, because US image contrast is low and boundaries are often not clear due to speckle. Researchers have explored several methods to obtain a reliable segmentation from medical images, which includes operator assisted region growing techniques [19], rule-based segmentation where some known image primitives are used for an unsupervised segmentation [20], atlas-based image segmentation where a known structure is searched in the image for segmentation [21], and neural network and c-mean clustering which generate statistical models to classify pixels into different segments. In this manuscript, we introduce a simple adaptive threshold based method [22], which is fast on data processing and easy for implementation; moreover, it also provides comparable accuracy for DOT reconstruction as compared with manual processing. This method utilizes image histogram to obtain an adaptive threshold for each input image. For some US images, the posterior shadow of a tumor extends to the chest wall and make the segmentation difficult. To avoid this problem, Hough Transform based line detection is used to determine the chest wall location and use it as the deep boundary of the tumor.

20 patients (10 benign and 10 malignant cases) are used to evaluate the performance of the segmentation method. Reconstructed absorption images are compared with manual processing method and similar results are obtained. To the best of our knowledge, this is the first report of an

automated segmentation method of using a US image to guide DOT image reconstruction. The method can be implemented into MIR or x-ray guided DOT imaging reconstruction.

2.4.1 Extract Tumor Size and Location

To automatically detected lesion size and location for DOT reconstruction, an adaptive threshold based segmentation method is used. For some cases, the posterior shadow of the tumor is extended to the chest wall in the US images. In those cases, it is difficult to determine the tumor size because the deeper boundary of the tumor cannot be accurately determined. Under these circumstances, locations of the chest wall are determined and used as estimates of the deeper boundary of the tumor. To determine the chest wall, Hough Transform [23] is used together with an edge detection method.
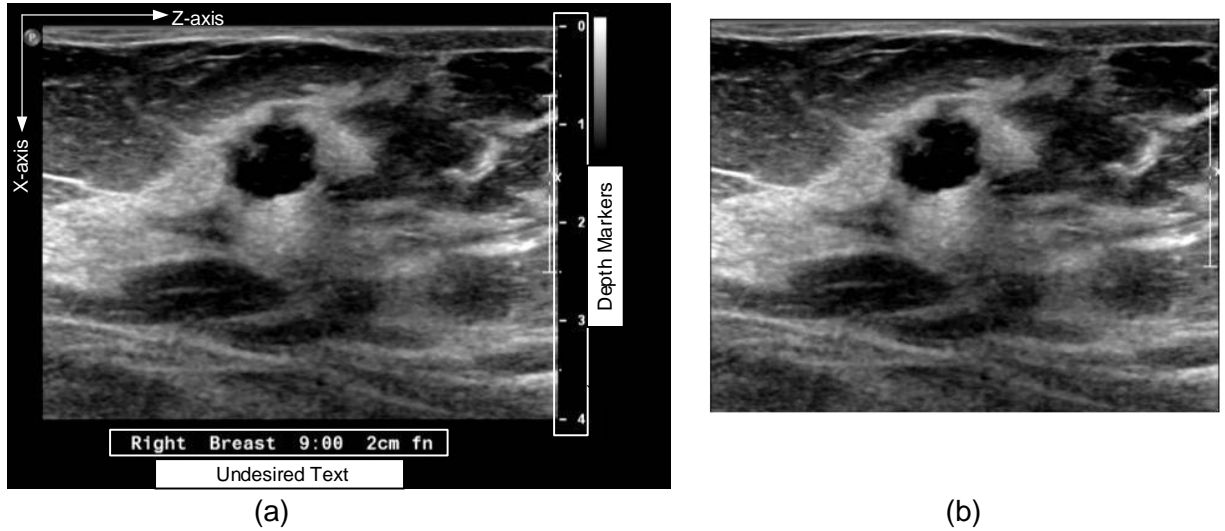
Figure 2. 14 (a) A typical US image captured in co-registration mode (b) Cropped US image

Pre-processing

A typical co-registered US image acquired by an image capture card is given in Figure 2.14 (a). For reference, the horizontal axis is marked as z-axis and the vertical axis is marked as the x-axis. Measurement in the y-axis is considered the same as the x-axis, assumed that lesions are symmetric

in x and y-axis. Since the pixel intensity is the critical information needed in the segmentation algorithm, the US grayscale image is automatically cropped first from the captured image using Hough Transform and Sobel [24] edge detection method. Figure 2.14(b) shows the cropped US image.
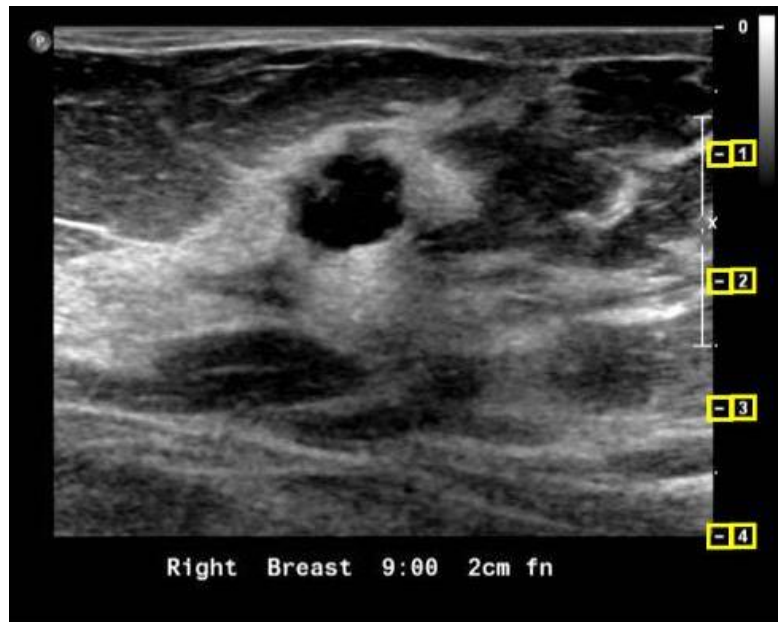
Figure 2. 15 Depth markers detected on US image

Depth marker detection is the next step before applying segmentation procedure because the markers vary with depth range, which depends on the user selection from the front panel of US machine. To determine the depth markers, a binary image is generated using a fixed pixel intensity of 150 out of 256 gray scale levels as the threshold. Since the depth markers are mainly white, this pixel intensity will help to separate them from the background. Then all the white regions consist of 3 to 50 pixels and located outside of the right border of the US image are marked as depth markers. This pixel range is obtained by examining the available US images collected from different manufacturers. This depth marker detection procedure detects horizontal ticks along with numbers which makes it suitable to use for images collected from a wide range of US machines.

Figure 2.15 shows the captured image with automatically detected depth markers. When positions of those depth markers are known, the difference between two markers in x-axis provides the number of pixels per centimeter, which are then used to convert the measured tumor size and depth into centimeter.

Adaptive Threshold-based Segmentation

To extract the required information from the US image, the first step is to segment the lesion from the rest of the image. Then the radius and center of the lesion can be measured from the segmented lesion. A single threshold point is used to separate the two zones, i.e., lesion and background. This threshold point is determined adaptively for each input images. Because US images have speckle noise, some complex segmentation techniques, such as fuzzy c-mean clustering, active contour model [25] do not provide any improvement while demanding computation resources due to complex processing. Moreover, DOT does not require precise segmented information. Thus, instead of using a complex segmentation algorithm, threshold-based segmentation is used here to obtain tumor information.

Lesions in breast US images usually appear as hypoechoic masses, which separate them from the background tissue. To segment a hypoechoic mass, a threshold point is set to separate the tumor from the rest of the image. US images usually have very low contrast. Histogram equalization is applied on the grey scale image. Histogram equalization stretches the input histogram over the available range which is 0 to 255 in greyscale and thus increases the contrast. Then a simple procedure is followed to detect the threshold point adaptively. Since the intensity varies significantly between different images, it is the best to use an adaptive threshold point for every input images.

This adaptive threshold point detection procedure starts with obtaining the histogram of the US image. Figure 2.16 (a) shows the histogram of an input image. The histogram shows a peak and a hump with a notch between them as indicated in the figure. This histogram shape is obtained from all US images after histogram equalization because of the presence of a significant amount of black (provides the peak) and grey pixels (the hump) in a US image. This notch shows the threshold for separating the grey background from the black tumor. To detect this point automatically, the slope of the histogram envelope is calculated. Pixel intensity of the point when the sign of the slope has changed is considered as the threshold value. In the next step, this threshold value is used to generate a binary image.
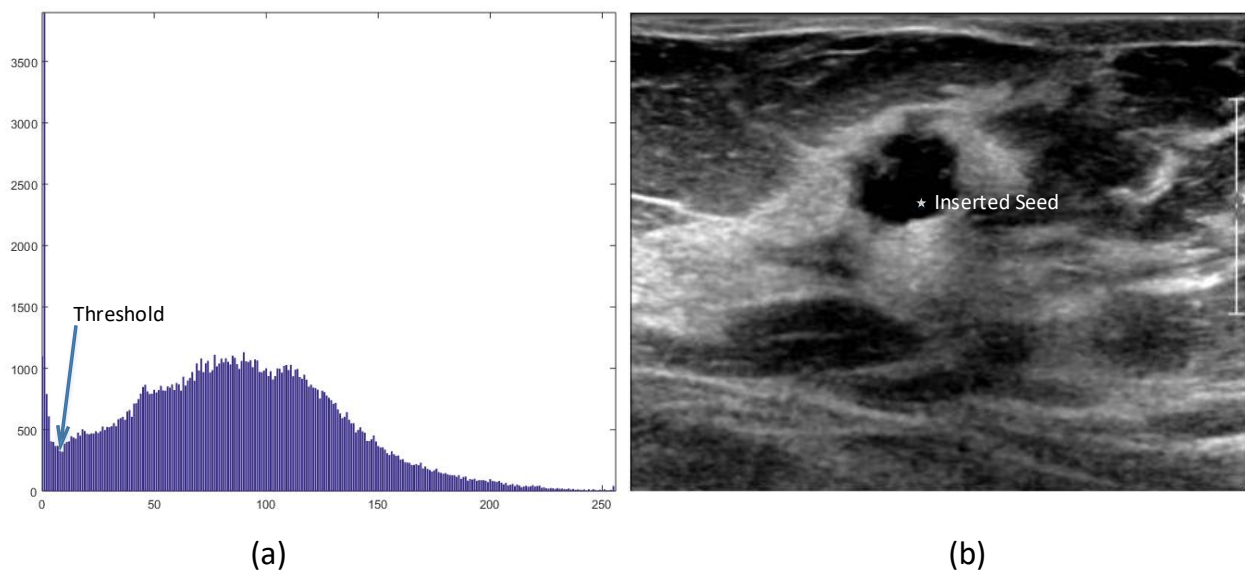
Figure 2. 16 (a) Histogram of a US image; threshold is marked with an arrow (b) Inserted seed on the cropped image by user

After obtaining the threshold for the US image, a binary image is generated where the tumor region is marked as black and background are white. However, the tumor is not the only black zone in the binary image. To remove the unwanted black regions user needs to insert a seed in the approximate tumor location by clicking the tumor in US image as shown in Figure 2.16 (b). If

there exist multiple tumors, then multiple seeds are required to be inserted in the probable locations. Any region that is not containing the seed is discarded. Finally, only the tumor region is survived. Then the MATLAB function 'regionprop' is used to measure the tumor center and radius automatically. This information is then passed to the optical reconstruction code. The flow diagram in fig. 2.17 shows the steps for the entire procedure.

```
┌─────────────┐   ┌─────────────┐   ┌─────────────┐   ┌─────────────┐   ┌─────────────┐
│ Input Image │ → │   Enhance   │ → │  Adaptive   │ → │    Tumor    │ → │   Measure   │
│             │   │   contrast  │   │  threshold  │   │  boundary   │   │tumor center │
│             │   │             │   │             │   │  Detection  │   │ and radius  │
└─────────────┘   └─────────────┘   └─────────────┘   └─────────────┘   └─────────────┘
```
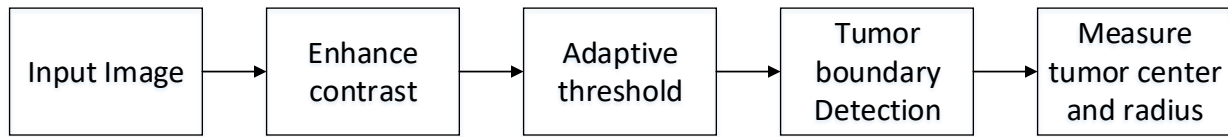
Figure 2. 17 Flow diagram of the tumor boundary detection procedures

2.4.2 Chest Wall Detection Using Hough Transform

Detection of chest wall depth is not essential to obtain tumor location and size. However, for some cases when the posterior shadow extends to the bottom of the US image, it is difficult to define the bottom of the tumor. In such cases, chest wall location is considered as the bottom of the tumor. We defined chest wall depth as the distance from the skin to the top layer of chest wall muscle. An automated chest wall depth detection method was developed and applied to the co-registered US images. Detection of the chest wall is based on the fact that chest wall muscles appear as line structures in US images (see Figure 2.18 (a)) [26]. Therefore, line detection algorithms can be used for automatic detection. We chose Hough Transform as a line detection method because it is robust and straightforward when combined with an edge detection method. Here, Canny edge detection [27] is used as an edge detection method. The binary image generated by the Canny edge detection is shown in Figure 2.18 (b).

It is clear from Figure 2.18 (b) that if Hough transform is applied to the edge detected image without any restriction, it will detect several unnecessary structures. For example, due to

37

subcutaneous fat and breast tissue interfaces, some linear structures appear at the top of the US image. There are other linear structures also visible in the image. Hough transform detects all these linear structures. To avoid these unnecessary line structures, we modeled chest as a linear structure which is mainly horizontal with a small slope and it should appear at the lower half of the image. After applying Hough transform and restrictions mentioned above, survived linear structures are marked in green lines as shown in Figure 2.18 (c). Finally, the mean value of all the points of these detected lines is considered as the chest wall depth. A flow diagram of the entire procedure is given in Figure 2.19.
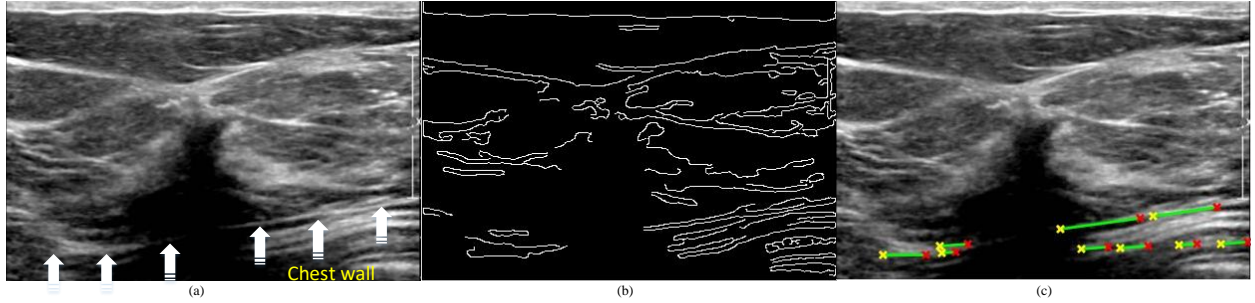
Figure 2. 18 (a) Breast US image with chest wall marked with arrows. (b) Edge detected binary image from (a). (c) Detected chest wall location on the original input image. The yellow and red stars indicate the separation points between line pieces. Green lines indicate the detected linear structures after restriction applying.
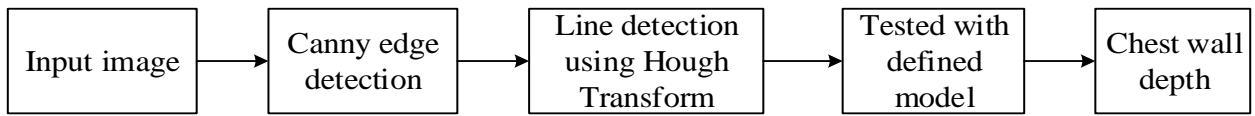
Figure 2. 19 Flow diagram of the chest wall detection method

2.4.3 Results

The proposed US segmentation method is evaluated in two steps. First, the US segmented reconstruction results are obtained and deviation is calculated against manually segmented reconstruction results. Second, both automated and manually segmented results are used to generate absorption maps and the corresponding hemoglobin concentration maps and compared.

38

Validation of US Segmentation

To evaluate the performance of the US segmentation algorithm, tumor boundary for all 20 cases were delineated by an experienced US image examiner. These readings are taken as standard in this study. Then the experimental results were compared with those manual measurements.

Two input images with manually marked tumor boundaries are presented in Figure 2.20 (a) and 2.23(a). In Figure 2.20 (b) and 2.23(b), segmented images using the proposed method are presented. It is clear from these figures that the segmented tumor by the proposed algorithm is comparable to the manual measurement. To obtain a quantitative evaluation of the US segmentation procedure, US images from 10 benign and 10 malignant cases are collected. The center coordinate of the tumor and radius in both axes are measured manually. The same information is also collected from the proposed segmentation method. The deviation is calculated between the two methods for 20 images. Comparison of the average measurements from these 20 images is given in Table 2.1. From the table, we found that manual measurements are slightly smaller than the proposed measurement. However, deviation from different measurements never exceeds 0.25 cm, which is the resolution of the optical reconstruction. So, optical reconstruction will not be affected by this small deviation.

<div align="center">(a)   (b)</div>

Figure 2. 20 (a) US image with manual markers to measure sizes of the tumor.   The measurements were 3.1cm in spatial direction x and 1.6 cm in depth direction z using manual measurements. (b) Segmented US image using the semi-automated procedure and the measurements were 3.3 cm in spatial x direction and 1.6 cm in depth direction.
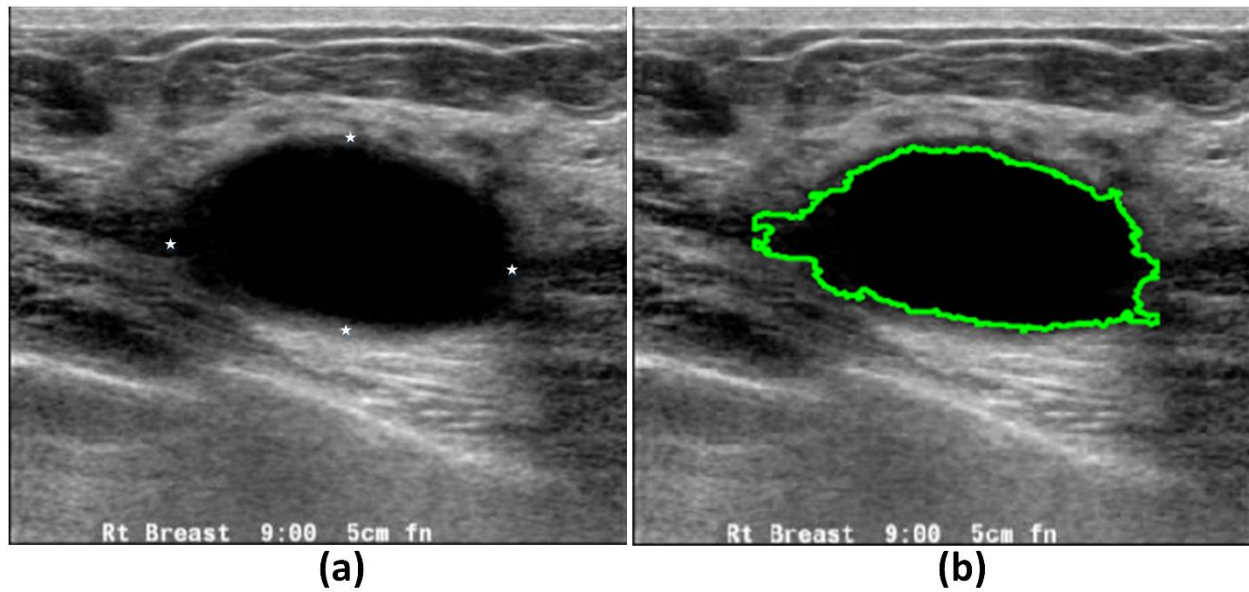
<div align="center">Table 2. 1 Comparison between manually and semi-automatic extracted information from US images</div>

		Manual Segmentation (cm)	Proposed Segmentation (cm)	Deviation =Manual-proposed (cm)
Benign **Cases**	z center position	1.49	1.56	-0.07
	x center position	0.14	0.19	-0.02
	z-radius	0.95	0.97	-0.1
	x-radius	1.55	1.65	-0.05
Malignant **Cases**	z center position	1.9	1.98	-0.07
	x center position	0.13	0.15	-0.03
	z-radius	1.15	0.99	-0.06
	x-radius	1.34	1.4	-0.03

To evaluate the repeatability of the proposed US segmentation algorithm, we have measured four parameters (lesion depth, z-radius, x-radius, x-center) from three different sets of US images and reconstructed the corresponding total hemoglobin maps. For each case, these images were collected from the same lesion location; however, some deviation was expected because the operator intended to hold the probe still for each data set and may move little between different data sets to obtain best US images. For each case, mean and standard deviation are given in Table 2.2. This deviation for depth is less than 1.5 mm and for other three spatial measurements is smaller than 0.25 cm (image grid size) and thus does not have any significant effect on optical reconstruction. As shown from the table, the maximum deviation obtained from benign cases is 4.45 µM and 2.06 µM for the malignant case.
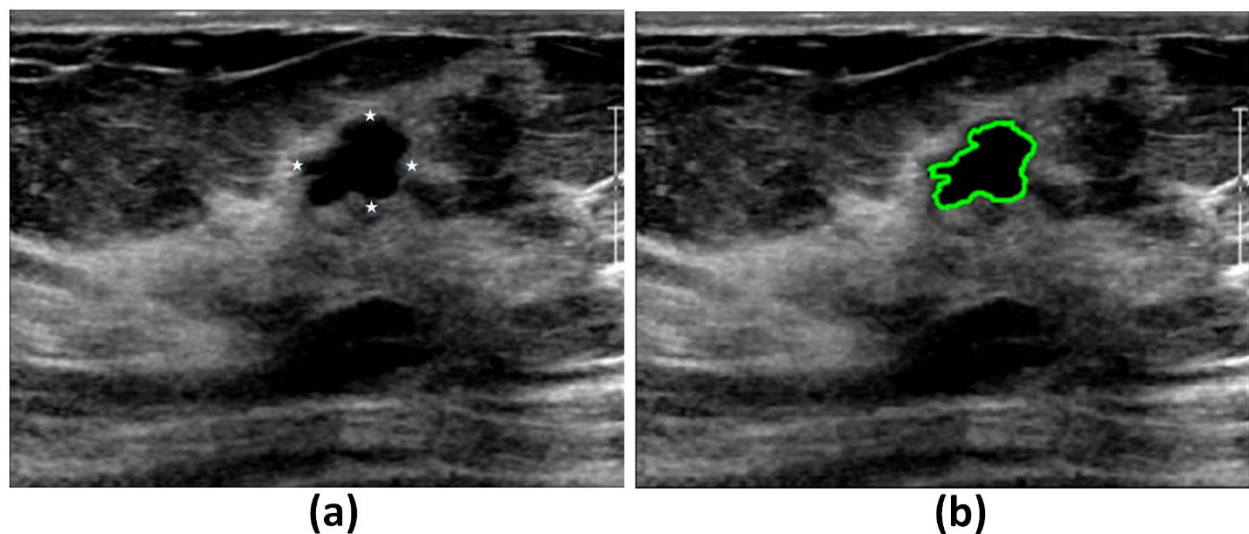
Figure 2. 21 (a) US image with manual markers to measure sizes of the tumor. The measurements were 0.88 cm in spatial direction x and 0.77 cm in depth direction z using manual measurements. (b) Segmented US image using the semi-automated procedure and the measurements were 0.9 cm in spatial x direction and 0.73 cm in depth direction.

Validation of Optical Reconstruction

The ultimate goal of the US segmentation algorithm is to assist DOT reconstruction. In this section, the performance of optical reconstruction is evaluated using tumor information extracted from both

Table 2. 2 Evaluation of the repeatability of the proposed method

	Depth (cm)	z-radius (cm)	x-radius (cm)	x center (cm)	Total Hemoglobin (µM)
	1.86 ± 0.042	1.48 ± 0.074	2.02 ± 0.233	0.47 ± 0.048	23.66 ± 0.905
	1.78 ± 0.001	1.57 ± 0.006	3.45 ± 0.189	0.3 ± 0.014	62.81 ± 0.384
	1.69 ± 0.013	1.44 ± 0.079	3.07 ± 0.118	0.45 ± 0.124	50.25 ± 4.452
	2 ± 0.006	0.4 ± 0.006	0.53 ± 0.006	0.58 ± 0.143	62.69 ± 0.362
	1.08 ± 0.003	0.39 ± 0.019	1.03 ± 0.070	-0 ± 0.026	42.33 ± 0.001
Benign	1.18 ± 0.006	0.56 ± 0.009	1.12 ± 0.166	0.09 ± 0.051	28.26 ± 0.022
Cases	1.61 ± 0.036	0.75 ± 0.024	1.61 ± 0.046	-0.1 ± 0.297	67.15 ± 0.018
	1.16 ± 0.009	0.24 ± 0.009	0.49 ± 0.024	0.15 ± 0.116	123.58 ± 0.317
	1.8 ± 0.040	2.52 ± 0.083	3.46 ± 0.114	-0.01 ± 0.079	64.11 ± 0.002
	1.32 ± 0.020	0.26 ± 0.004	0.48 ± 0.042	0 ± 0.013	83.98 ± 0.002
	1.35 ±0.019	0.72 ± 0.012	0.93 ± 0.027	0.21 ± 0.117	109.78 ± 0.129
	2.55 ± 0.031	1.92 ± 0.029	2.84 ± 0.065	0.16 ± 0.077	172.66 ± 0.000
	2.97 ± 0.018	1.45 ± 0.036	2.34 ± 0.016	-0.63 ± 0.243	198.14 ± 1.734
	1.66 ± 0.008	0.88 ± 0.009	1.07 ± 0.031	0.48 ± 0.106	93.36 ± 2.061
Malignant	2.03 ± 0.029	0.65 ± 0.078	0.43 ± 0.009	-0.49 ± 0.035	95.73 ± 0.038
Cases	1.45 ± 0.027	1.09 ± 0.009	1.45 ± 0.024	0.52 ± 0.079	107.23 ± 1.375
	2.59 ± 0.001	0.3 ± 0.030	0.55 ± 0.014	0.19 ± 0.028	135.49 ± 0.060
	1.94 ± 0.073	1.34 ± 0.137	2.76 ± 0.219	0.53 ± 0.082	77.77 ± 0.556
	1.79 ± 0.014	0.77 ± 0.026	0.81 ± 0.037	0.46 ± 0.099	156.49 ± 0.992
	1.57 ± 0.016	0.65 ± 0.000	0.97 ± 0.015	0.24 ± 0.010	88.84 ± 0.001

manual and proposed segmentation process. Optical data of the same 20 patients were used to generate absorption maps for four different wavelengths. Then the absorption information is used to obtain hemoglobin concentration. Both manual and semi-automatic features are used to generate different absorption maps. In Figure 2.21 and 2.22, absorption maps for a benign case are compared and a malignant case is presented in Figure 2.24 and 2.25. It is clear from these figures that the reconstructed map is almost similar. Average maximum absorption from 20 cases is compared in Table 2.3. From the table, we can see that mean optical absorption obtained from manual measurement was $0.21\pm.06$ cm^{-1} for malignant and $0.12\pm.06$ cm^{-1} for benign cases, where for the proposed method it was $0.24\pm.08$ cm^{-1} for malignant and $0.12\pm.055$ cm^{-1} for benign tumors.

Finally, Figure 2.26 shows boxplots for oxygenated, de-oxygenated and total hemoglobin concentrations for the same 20 cases for both manual and proposed automated procedure. We can see from this figure that results for both techniques are almost similar. For benign cases, mean total hemoglobin concentration for all 10 cases is 58.95 ± 27.76 µM from manual segmentation and 58.64 ± 27.93 µM for the proposed automated segmentation. For malignant cases, this measurement is 115.23 ± 39.62 µM from manual segmentation and 114.64 ± 49.66 µM for the automated segmentation. Values for oxygenated hemoglobin, for benign cases, is 35.73 ± 20.67 µM for manual segmentation method and 38.32 ± 21.67 µM for proposed segmentation method. For malignant cases, this measurement is 72.30 ± 23.07 µM and 75.27 ± 27.92 µM for manual and proposed segmentation method respectively. Deoxygenated hemoglobin concentration is 35.41 ± 15.31 µM and 37.13 ± 16.21 µM for benign cases using manual and proposed segmentation method respectively. For malignant cases, this measurement increases to 50.26 ± 19.63 µM and 48.04 ± 22.88 µM for manual and proposed segmentation method. Thus, the performance of the proposed feature extraction technique is quite acceptable.
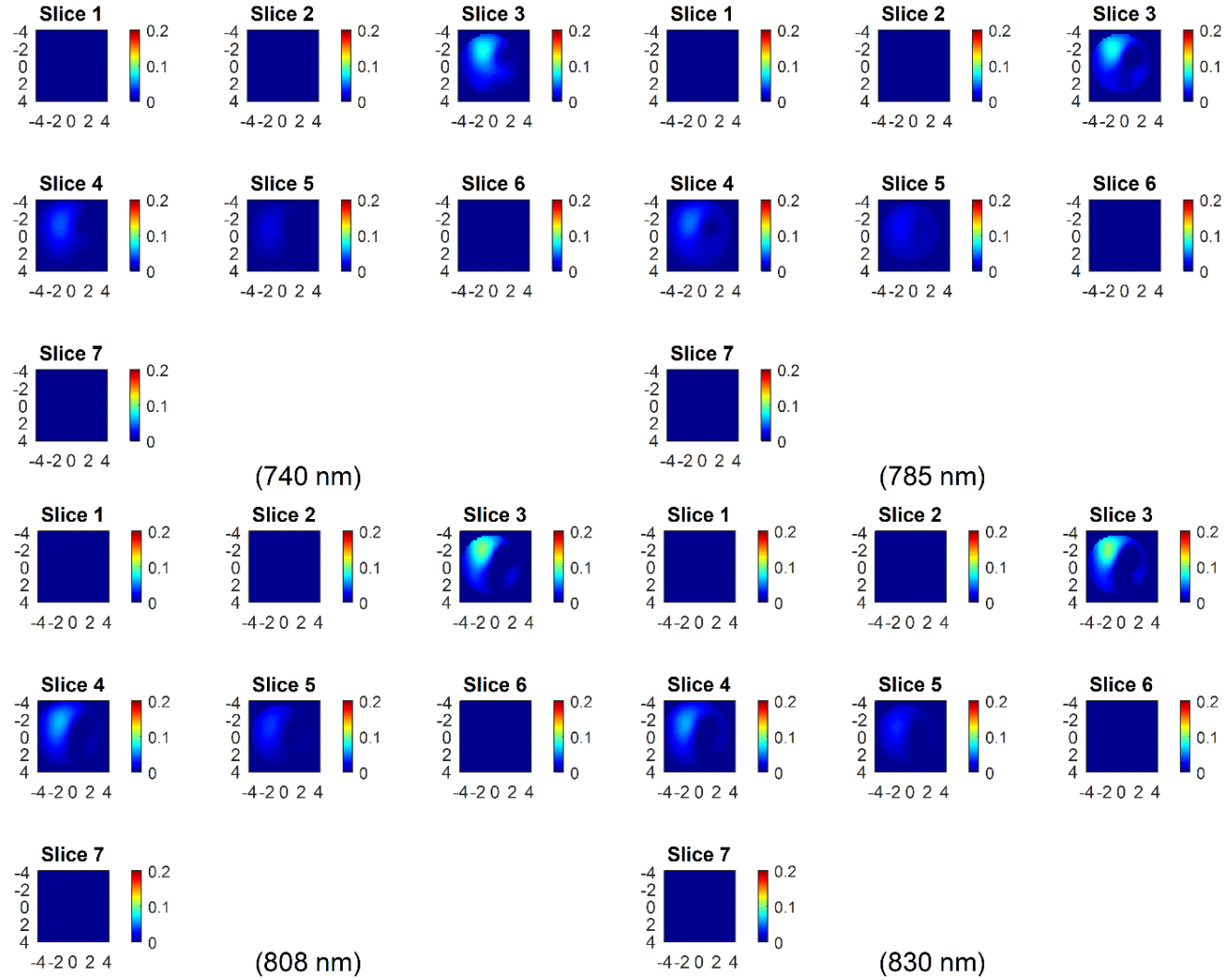
Figure 2. 22 Optical absorption maps of four wavelengths using three times of the size measured by US in x-dimension. Depth used in optical reconstruction is the same as US measurement. Each optical absorption map has seven image slides of 0.5 cm from the skin surface to the chest wall with 0.5 cm step in depth. Manually measured tumor information from 2.20 (a) is used in these maps
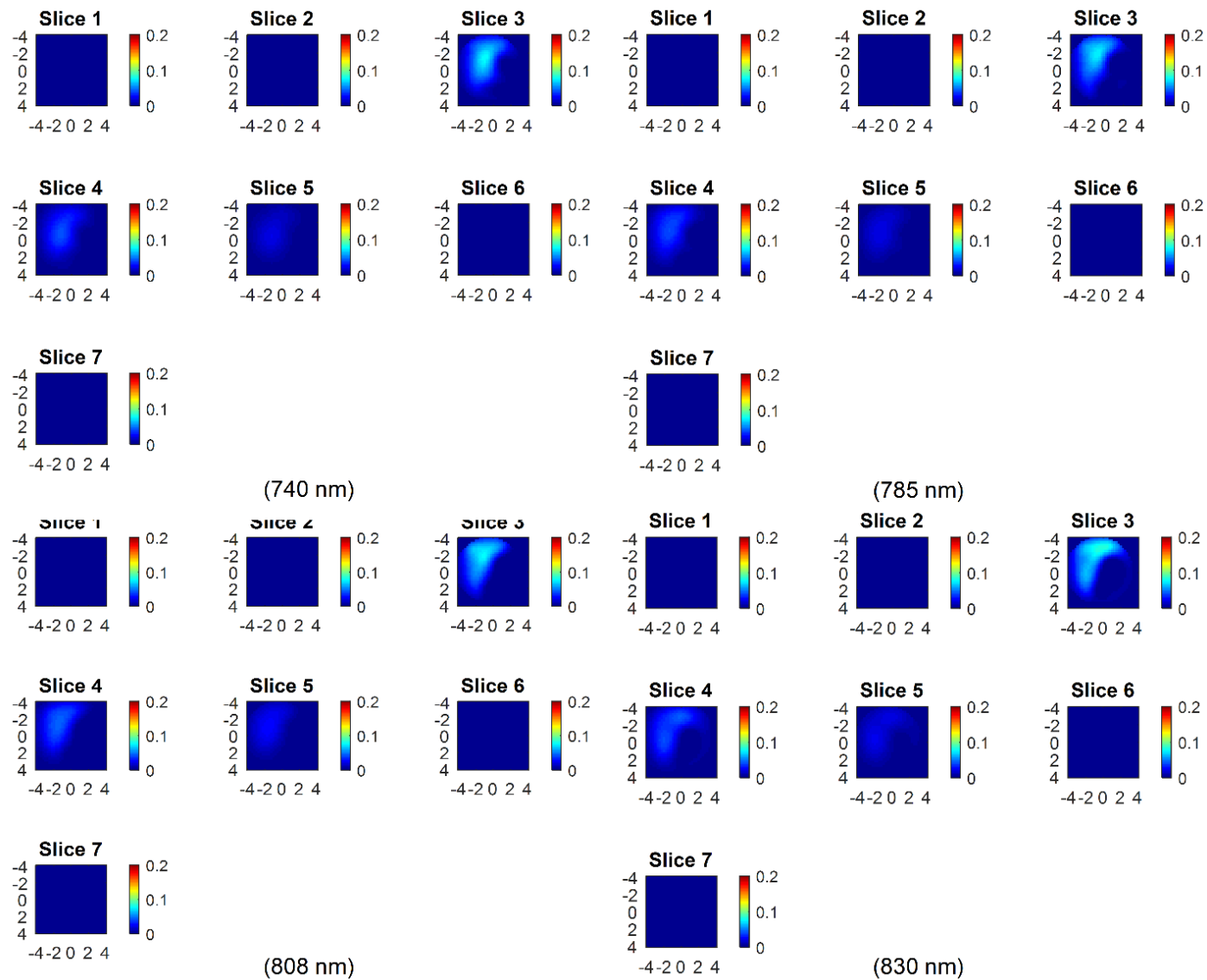
Figure 2. 23 Optical absorption maps using three times of the size identified by US in x-dimension. Depth used in optical reconstruction is the same as US measurement. Tumor information for these maps was extracted from 2.20 (b)

45
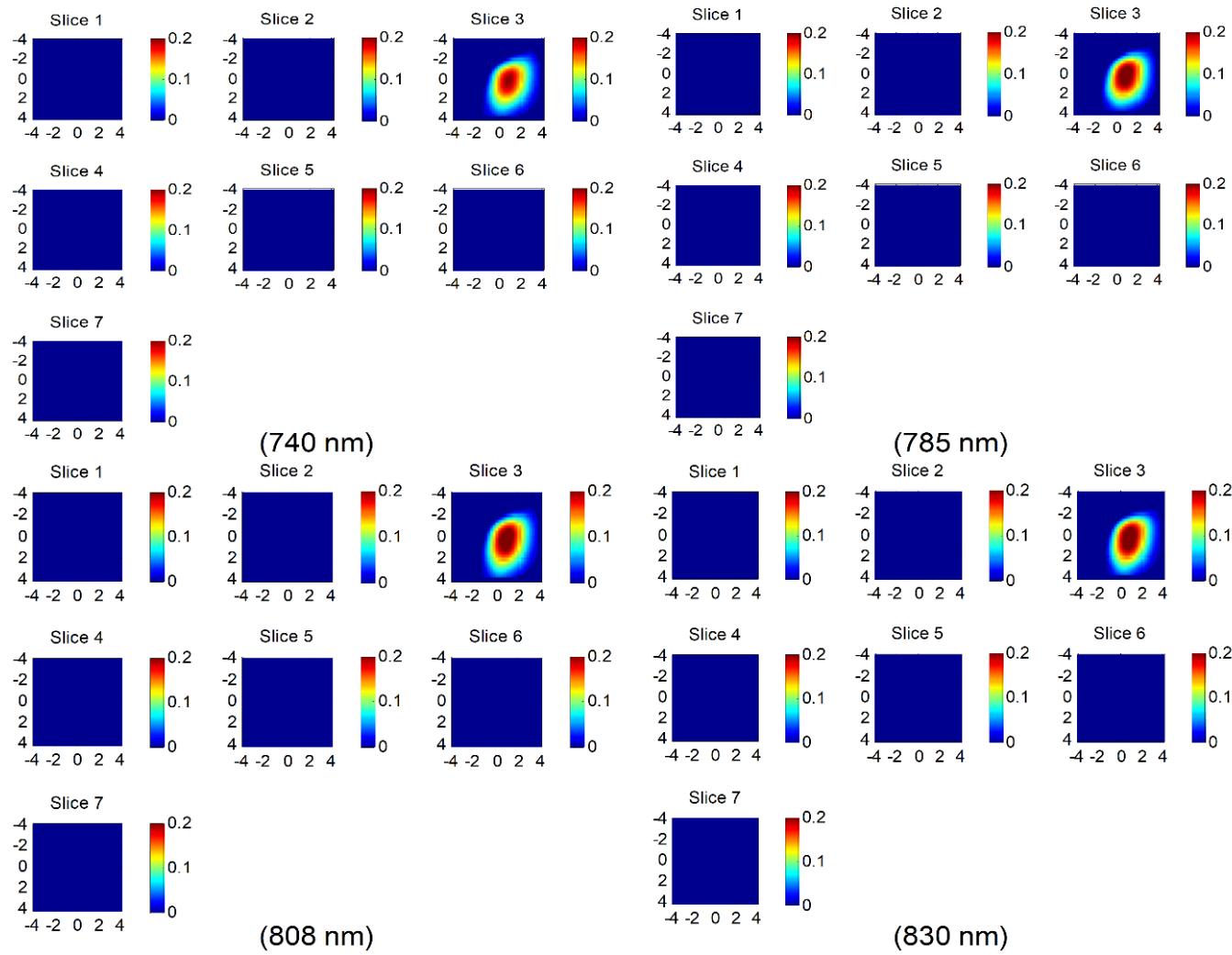
Figure 2. 24 Optical absorption maps of four wavelengths using three times of US measured size in x and same size as US measurement in z. Tumor dimension and location was extracted from 2.23 (a) to generate these maps

46
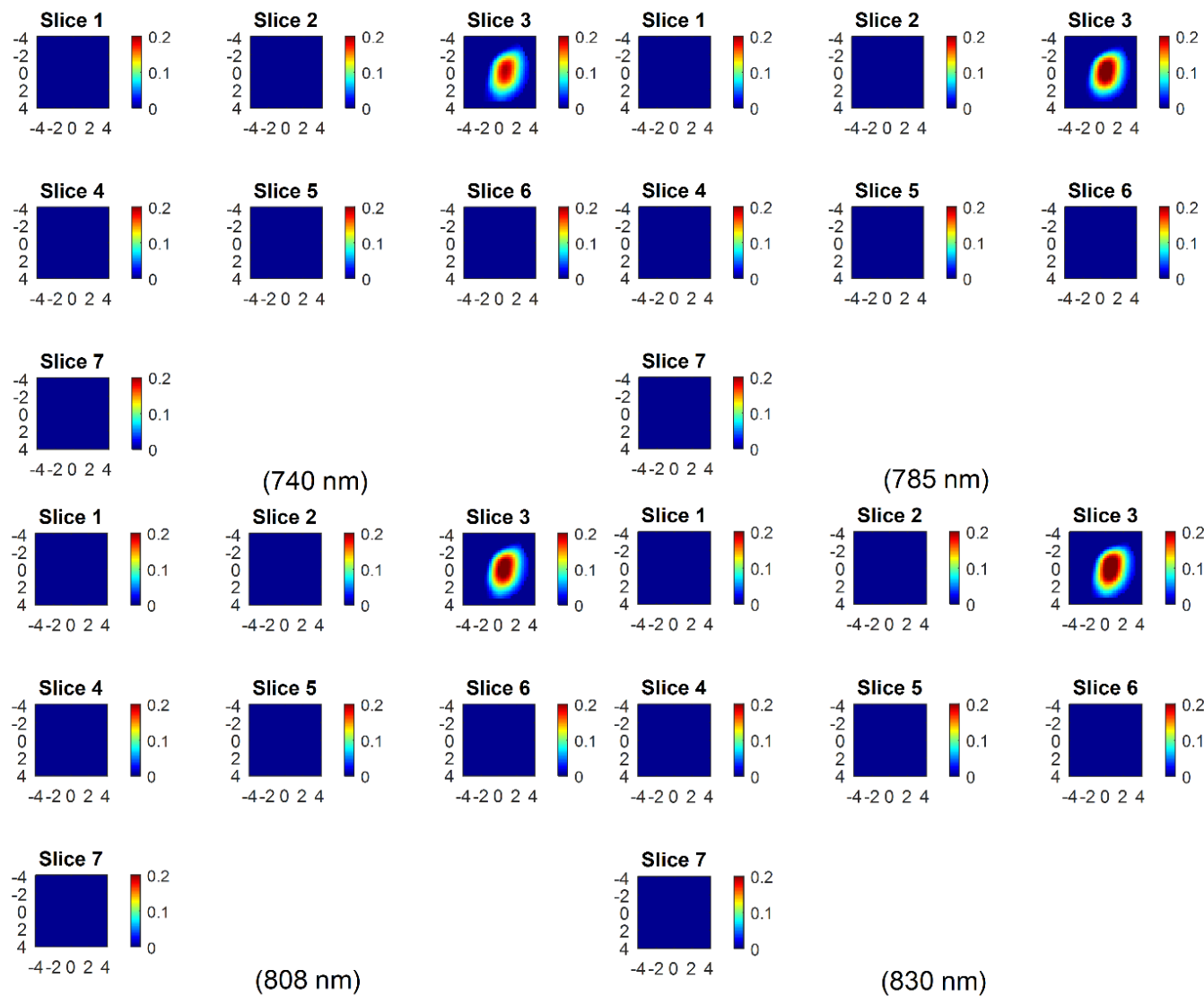
Figure 2. 25 Optical absorption maps using three times of US measured size in x and same size as US measurement in z. To generate these maps tumor information was extracted from 2.23 (b).

47

Table 2. 3 Average absorption coefficient using manual and automatically segmented tumor information

Average (Standard Deviation) of maximum reconstructed absorption

with manual tumor segmentation(cm^{-1})

	Malignant	**Benign**	**Ratio**
740 nm	0.19 (0.08)	0.11 (0.06)	1.72
780 nm	0.22 (0.07)	0.12 (0.06)	1.83
808 nm	0.22 (0.05)	0.14 (0.08)	1.57
830 nm	0.22 (0.05)	0.13 (0.05)	1.69

Average (Standard Deviation) of maximum reconstructed absorption

with proposed tumor segmentation(cm^{-1})

	Malignant	**Benign**	**Ratio**
740 nm	0.21 (0.08)	0.14 (0.05)	1.5
780 nm	0.25 (0.09)	0.12 (0.05)	2.08
808 nm	0.24 (0.08)	0.12 (0.06)	2
830 nm	0.24 (0.08)	0.12 (0.06)	2
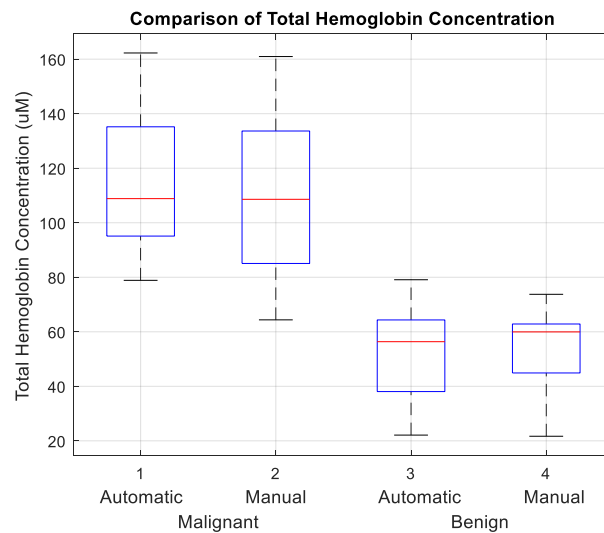
Figure 2. 26 Comparison of total hemoglobin concentration for 10 benign and 10 malignant cases.

2.5 Summary

System and algorithm development for diffuse optical tomography was one of two aims of this PhD research. To make the ultrasound-guided diffuse optical tomography technology suitable for clinical applications several design modifications have been done. Probe holder for the system was redesigned to accommodate the optimized source and detector locations. Instead of purchasing the commercial laser current drivers and heat sink, custom designed current driver was used which reduced the cost and area requirements as well as added flexibility in component placement and spacing. In the detector side, combined mixer, amplifier and filter board design make the detector more compact than the previous prototype, significantly reduced the cost and provided a similar performance in terms of signal integrity. Software controlled PMT gain setting was an important step to make the system more suitable for clinical technicians. After all these system modifications, users now can control the system using the graphical interface of the software and thus satisfied the critical goal of this research which is making the ultrasound-guided diffused optical system suitable for clinical application.

Semi-automatic segmentation of tumor in the ultrasound image was another component that makes the optical image reconstruction less operator dependent. This segmentation procedure requires minimum input from the users, which make this image reconstruction procedure suitable for anyone with little knowledge about breast ultrasound images. A part of this segmentation algorithm was automatic chest wall detection, which proved suitable for another study where the chest wall height of several hundreds of breast ultrasound images was determined using this chest wall detection algorithm. Current DOT image reconstruction is providing meaningful optical reconstructed images from over 90% cases. Improvement is going on to make it more effective.

Reference

[1]   D. A. Boas *et al.*, "Imaging the body with diffuse optical tomography," *IEEE Signal Process. Mag.*, vol. 18, no. 6, pp. 57–75, 2001.

[2]   X. Wu, J. P. Culver, A. T. Eggebrecht, S. L. Ferradal, and H. Dehghani, "Fast and efficient image reconstruction for high density diffuse optical imaging of the human brain," *Biomed. Opt. Express*, vol. 6, no. 11, p. 4567, 2015.

[3]   T. Durduran, R. Choe, W. B. Baker, and A. G. Yodh, "Diffuse optics for tissue monitoring and tomography," *Reports Prog. Phys.*, vol. 73, no. 7, p. 76701, 2010.

[4]   B. Chance *et al.*, "Breast Cancer Detection Based on Incremental Biochemical and Physiological Properties of Breast Cancers: A Six-Year, Two-Site Study1," *Acad. Radiol.*, vol. 12, no. 8, pp. 925–933, 2005.

[5]   A. Torricelli *et al.*, "Estimate of tissue composition in malignant and benign breast lesions by time-domain optical mammography," *Biomed. Opt. Express*, vol. 5, no. 10, p. 3684, 2014.

[6]   E. L. Miller *et al.*, "Parametric estimation of 3D tubular structures for diffuse optical tomography," *Biomed. Opt. Express*, vol. 4, no. 2, p. 271, 2013.

[7]   Q. Zhu *et al.*, "Assessment of Functional Differences in Malignant and Benign Breast Lesions and Improvement of Diagnostic Accuracy by Using US-guided Diffuse Optical Tomography in Conjunction with Conventional US," *Radiology*, vol. 280, no. 2, pp. 387–397, 2016.

[8]   L. V. Wang and H. Wu, "Biomedical Optics: Principles and Imaging," 2012, pp. 249–281.

[9]   B. E. Schaafsma *et al.*, "Optical mammography using diffuse optical spectroscopy for monitoring tumor response to neoadjuvant chemotherapy in women with locally advanced breast cancer," *Clin. Cancer Res.*, vol. 21, no. 3, pp. 577–584, 2015.

[10]   B. J. Tromberg, B. W. Pogue, K. D. Paulsen, A. G. Yodh, D. A. Boas, and A. E. Cerussi, "Assessing the future of diffuse optical imaging technologies for breast cancer management," *Med. Phys.*, vol. 35, no. 6, pp. 2443–2451, 2008.

[11]   C. Xu *et al.*, "Ultrasound-Guided Diffuse Optical Tomography for Predicting and Monitoring Neoadjuvant Chemotherapy of Breast Cancers: Recent Progress," *Ultrasound Imaging*, vol. 38, no. 1, pp. 5–18, 2016.

[12]   M. Huang and Q. Zhu, "Dual-mesh optical tomography reconstruction method with a depth correction that usesa prioriultrasound information," *Appl. Opt.*, vol. 43, no. 8, pp. 1654–1662, 2004.

[13]   N. Chen, P. Guo, S. Yan, D. Piao, and Q. Zhu, "Simultaneous near-infrared diffusive light and ultrasound imaging," *Appl. Opt.*, vol. 40, no. 34, pp. 6367–6380, 2001.

[14]   Q. Zhu *et al.*, "Optimal probing of optical contrast of breast lesions of different size

located at different depths by US localization," *Technol. Cancer Res. Treat.*, vol. 5, no. 4, pp. 365–380, 2006.

[15] H. Vavadi *et al.*, "Compact ultrasound-guided diffuse optical tomography system for breast cancer imaging," *J. Biomed. Opt.*, vol. 24, no. 2, pp. 021203-1–9, 2018.

[16] F. Zhou, A. Mostafa, and Q. Zhu, "Improving breast cancer diagnosis by reducing chest wall effect in diffuse optical tomography," *Diagnosis Treat. Dis. Breast Reprod. Syst.*, vol. 22, no. 3, pp. 036004-1–10, 2017.

[17] H. Vavadi and Q. Zhu, "Automated data selection method to improve robustness of diffuse optical tomography for breast cancer imaging," *Biomed. Opt. Express*, vol. 7, no. 10, p. 4007, 2016.

[18] A. Mostafa, H. Vavadi, K. M. S. Uddin, and Q. Zhu, "Diffuse optical tomography using semiautomated coregistered ultrasound measurements," *J. Biomed. Opt.*, vol. 22, no. 12, pp. 121610-1–12, 2017.

[19] S.-Y. Wan and W. E. Higgins, "Symmetric region growing," in *Proceedings 2000 International Conference on Image Processing*, 2000, vol. 2, pp. 96–99.

[20] Y. Xia, K. Bettinger, L. Shen, and A. L. Reiss, "Automatic Segmentation of the Caudate Nucleus From Human Brain MR Images," *IEEE Trans. Med. Imaging*, vol. 26, no. 4, pp. 509–517, 2007.

[21] B. Fischl, M. I. Sereno, and A. M. Dale, "Cortical Surface-Based Analysis: II: Inflation, Flattening, and a Surface-Based Coordinate System," *Neuroimage*, vol. 9, no. 2, pp. 195–207, 1999.

[22] E. R. Davies, *Computer and Machine Vision: Theory, Algorithms, Practicalities*. Elsevier, 2004.

[23] D. H. Ballard, "Generalizing the Hough transform to detect arbitrary shapes," *Pattern Recognition*, vol. 13, no. 2, pp. 111–122, 1981.

[24] M. James, *An introduction to edge detection: The sobel edge detector*. 2002.

[25] D. J. Withey and Z. J. Koles, "A Review of Medical Image Segmentation: Methods and Available Software," *Int. J. Bioelectromagn.*, vol. 10, no. 3, pp. 125–148, 2008.

[26] J. H. Youk, E.-K. Kim, M. J. Kim, and K. K. Oh, "Imaging Findings of Chest Wall Lesions on Breast Sonography," *J. Ultrasound Med.*, vol. 27, no. 1, pp. 125–138, 2017.

[27] J. Canny, "A computational approach to edge detection," *IEEE Trans. Pattern Anal. Mach. Intell.*, pp. 679–698, 1986.

3 Ultrasound Guided Photoacoustic Tomography

Alexander Graham Bell first reported photoacoustic effect in the late 1800s [1]. However, photoacoustic imaging was not feasible for clinical diagnosis until the advances made in ultrasound transducers, computers, and laser systems. Wang et al. [2] reported some early experiments demonstrating the efficacy of photoacoustic tomography for medical imaging. In photoacoustic tomography, acoustic waves are generated by shining the tissue with short duration NIR laser pulses. The amplitude of the acoustic wave depends on the number of photons absorbed by the tissue. Conventional ultrasound transducers can be used to detect this acoustic wave, which makes this technology suitable to use in clinical settings. Since human tissue is highly scattering medium for photons, photons cannot reach deeper than 5 cm inside an organ; thus, PAT has depth limitation of 5 cm, which is suitable for many applications including ovarian cancer detection.

Ovarian cancer is the deadliest among all gynecological cancers. It has five years survival rate of less than 30% when detecting at stage III or IV. However, survival change can dramatically increase to 80-90% when it is discovered in stage I or II [3]. Unfortunately, most of the time this cancer can develop inside the human body without expressing any significant symptoms. Thus, make it very hard to detect at an early stage. Lack of suitable tools to early diagnose of ovarian cancer makes the diagnosis even harder. Therefore, any patient with ovarian abnormality has to go through oophorectomy, which significantly reduces the quality of life of the patient. Currently used methods, i.e., CA125 screening, CT, ultrasound, MRI still struggling to improve the sensitivity and specificity [4]–[9]. Our newly developed PAT system has demonstrated huge potential for early detection of ovarian cancer in a convenient way.

This chapter will present the image reconstruction principles of US and PAT followed by their application is an ovarian cancer diagnosis. It consists of the description of our newly developed system, evaluation report, and solution for a practical problem.

3.1 Imaging Principle

For ovarian cancer diagnosis, we are using co-registered ultrasound and PAT images and RF data. Following two sections will briefly describe the relationship between the Co-registered US/PAT images and ovarian cancer diagnosis.

3.1.1 Ultrasound Imaging

Compressional waves are used in ultrasound imaging to image tissue mechanical properties. Particles inside the medium compress and extend to propagate the wave through the medium. Ultrasound transducers are generating a propagating wave by vibrating at the tissue surface. This vibration creates a local pressure p, which propagates along the z-axis. Thus, the pressure wave equation can be expressed by:

$$\frac{\partial^2 p}{\partial^2 z^2} - \frac{1}{v_s^2}\frac{\partial^2 p}{\partial t^2} = 0$$

3. 1

Where v_s is the speed of sound in medium (about 1500 m/s in human tissue). This equation will take the following form when expressing the equation for the 3D space.

$$\nabla^2 p - \rho K \frac{\partial^2 p}{\partial t^2} = 0$$

3. 2

Where ρ is the density of the medium and K is the compressibility constant which is related to the pressure-velocity using the following equation,

$$v_s = \sqrt{\frac{1}{\rho K}}$$

When ultrasound wave propagates through the medium, its velocity is affected by the acoustic impedance of the medium which can be expressed by the following equation,

$$Z = \frac{p}{v} = \rho v_s = \sqrt{\frac{\rho}{K}}$$

When the propagating US wave enters from one type of tissue to another type of tissue with different acoustic impedance, then some portion of the wave is reflected from the tissue boundary. The reflection coefficient of the tissue determines the portion of the incident wave enters the second medium, and the portion is reflected the first medium. The incident angle of the wave and the acoustic impedance of the mediums determine the reflection coefficient of the tissue. When the wave propagates from medium 1 to medium 2, the reflection coefficient can be expressed using equation 3.5,

$$R = \frac{\left(\frac{Z_2}{cos\theta_t}\right) - \left(\frac{Z_1}{cos\theta_i}\right)}{\left(\frac{Z_2}{cos\theta_t}\right) + \left(\frac{Z_1}{cos\theta_i}\right)}$$

Where θ_t and θ_i are the transmission angle and incident angle respectively, and Z_1 and Z_2 are the acoustic impedance of medium 1 and medium 2 respectively. As shown in Figure 3.1, the incident ultrasound wave is reflected from different tissue boundaries as they have different acoustic impedances. This recorded signal is called A-line. Multiple A-lines are combined to reconstruct a US image.

Other than the transmission and reflection, the acoustic wave is also affected by the attenuation of the tissue. Thus, as the wave propagates deeper in the tissue its amplitude attenuates and soon goes below the noise level. This attenuation is inversely proportional to the frequency of the incident

wave. The attenuation for the softest human tissue is between 1.35 and 1.68 $dBcm^{-1}MHz^{-1}$. All medical US image reconstruction procedure tries to estimate the pressure distribution inside the human body from the reflected waveform, which is captured by the transducer. This pressure distribution is related to the internal structure of the subject, which may reveal significant clinical information. Since the ovarian tumor has a different structure than the background, using US images, it can be readily separable from the background. Some extracted features from US beams can be used for diagnosing benign and malignant tumors as they are related to the structure of the subject [10].
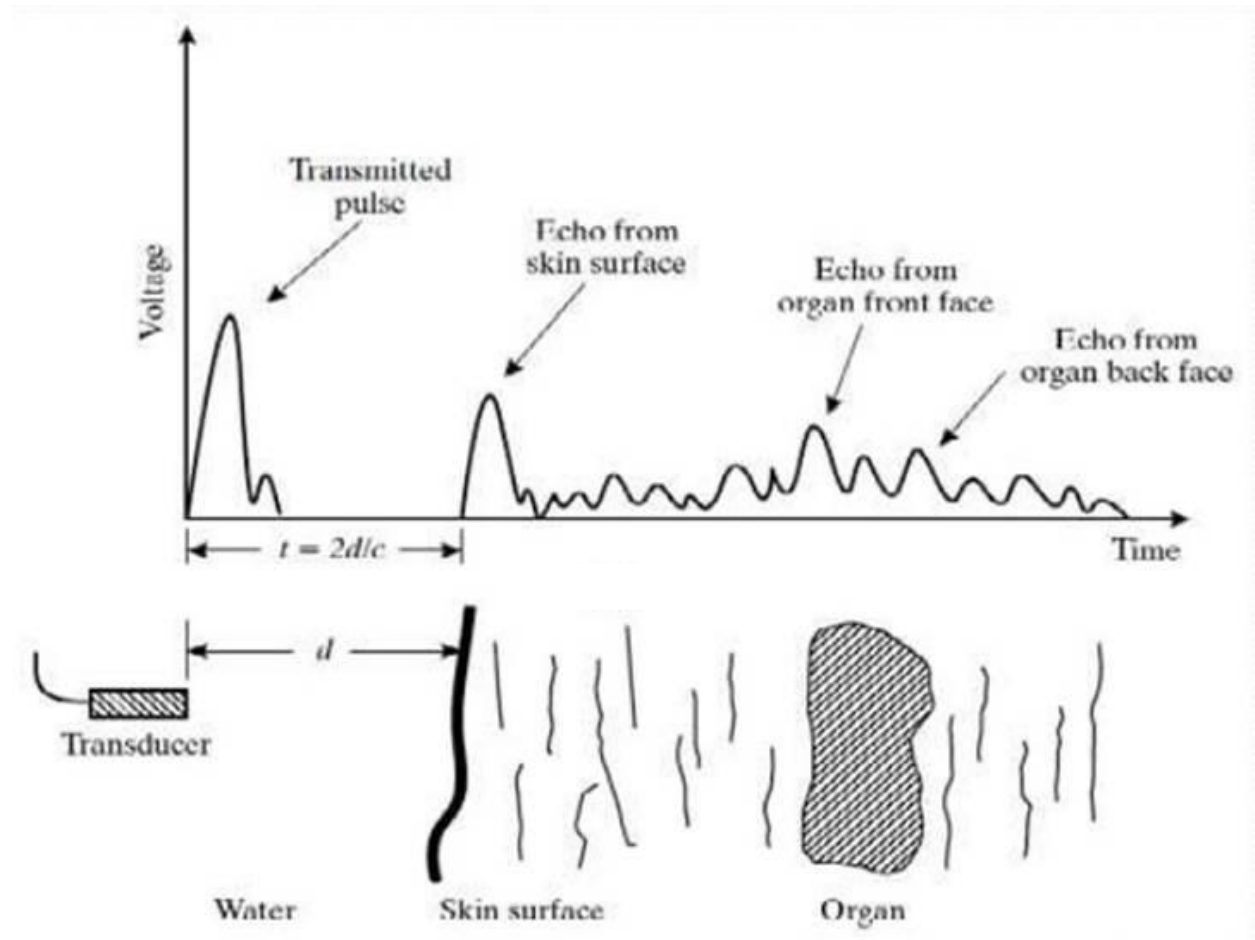
Figure 3. 1: Ultrasound wave reflected from different tissue boundaries [11]

Two types of US images can be generated using the US system. Stacking multiple A-lines at different times will produce M-mode images, which reveals the pressure change with time. On the contrary, stacking a-lines collected at different locations generates B-mode images. For ovarian cancer detection, we are interested in B-mode imaging because ovarian tumor changes its shape very slowly thus collecting meaningful information from M-mode images will take a long time, which is not feasible in the clinical setting. In the rest of the chapters, B-mode US image will be referred to as US image, since in our experiments we never work with M-mode images.

B-mode ultrasound images can be collected by shifting a single transducer in space to collect a-lines at various locations. However, this method is not fast enough to obtain good quality images. In our applications, we have used an ultrasound transducer array, which consists of multiple ultrasound transducers at close spacing. By applying electric pulses at a variable delay, a focused steering wavefront can be generated. When the reflected signal came back, they can be added after delay correction to obtain a focused beam. This method is shown in Figure 3.2 and 3.3.

Several features related to the mechanical properties of the tissue can be derived from US beams. After the beamforming, demodulating the carrier signal provides an envelope signal. After scan conversion, a B-mode US image is obtained from this envelope signal. These steps of US image reconstruction is presented in Figure 3.4.
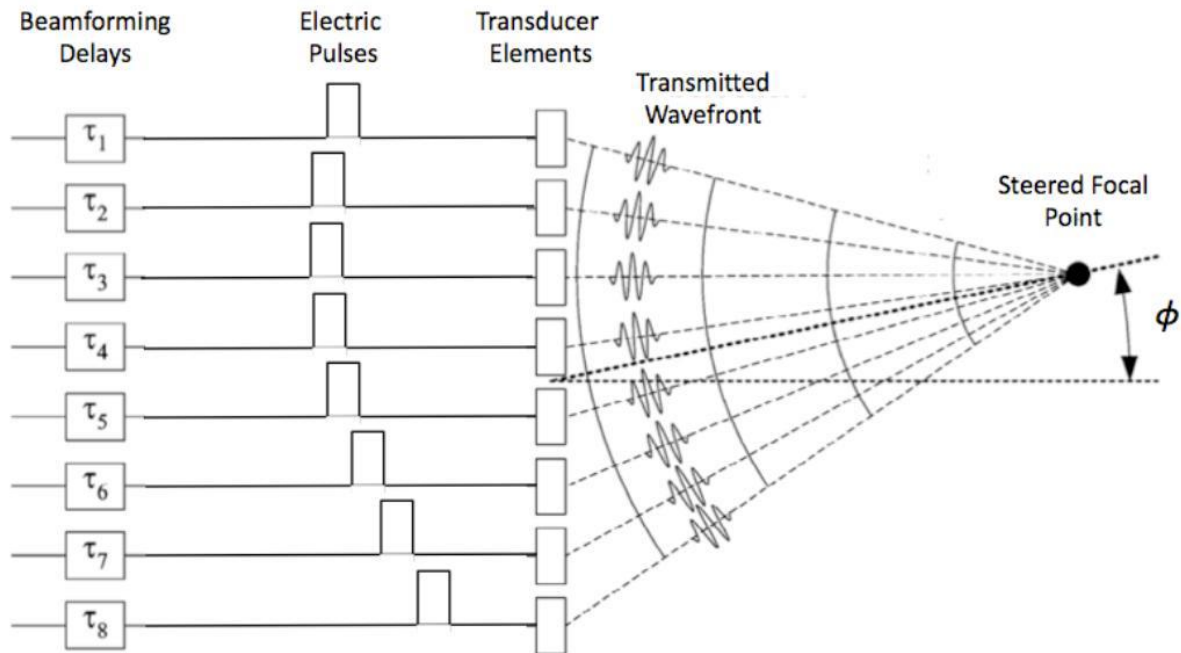
Figure 3. 2 Transmission focusing and steering in US mode [11]
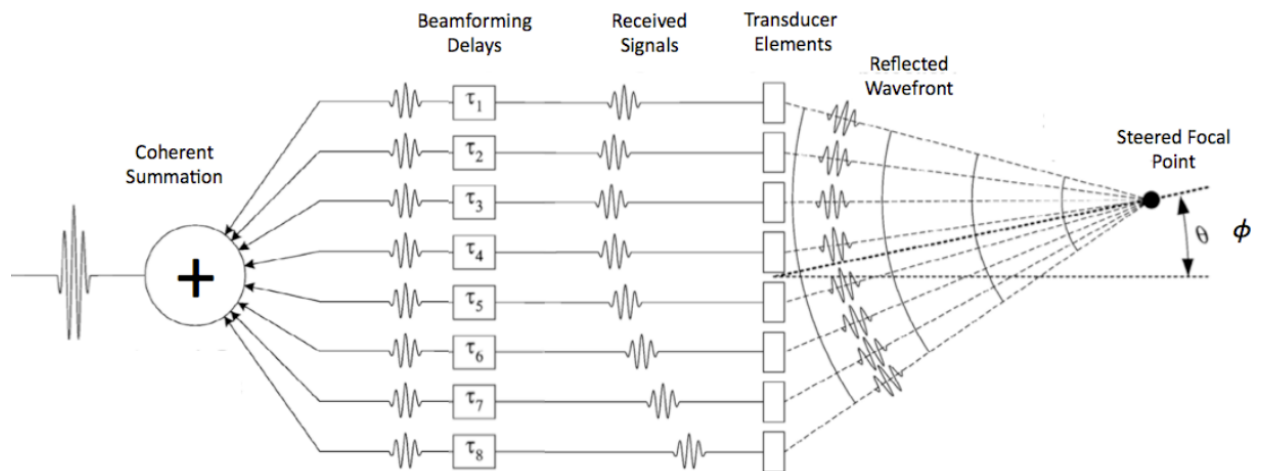
Figure 3. 3 Receiving Beamforming in US mode [11]
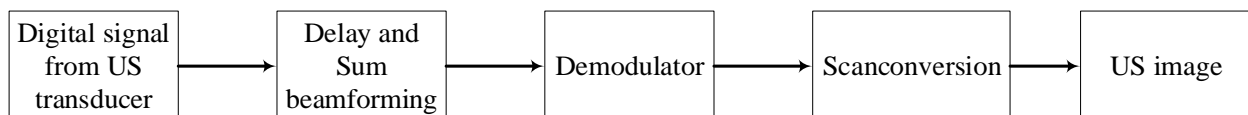
Figure 3. 4 High-level block diagram for US image reconstruction

3.1.2 Photoacoustic Imaging

Obtaining functional information from the target location is the primary motivation for photoacoustic imaging. In PAT mode, short laser pulses are applied to the tissue to produce acoustic waves, which is detected by ultrasound transducers. During PAT imaging, effect of intense light scattering inside the human tissue is reduced by using the acoustic detection, at the same time information related to the light absorption is preserved by using light to generate acoustic waves. Thus, PAT combines the advantages of optical and US imaging.

When the short laser pulses shine the tissue surface, it creates acoustic pressure as expressed by the following equation,

$$p_0 = \frac{\beta}{\kappa \rho C_V} \eta_{th} A_e$$

3. 6

Here, β is the thermal coefficient of the volume expansion, C_V denotes the specific heat capacity at constant pressure, A_e is the specific optical absorption and η_{th} is the heat conversion efficiency of the target. Optical absorption is the product of the absorption coefficient of the target μ_a and the incident fluence F. After replacing the optical absorption and the constants with Grueneisen parameter, equation 3.6 can be expressed as,

$$p_0 = \Gamma \eta_{th} \mu_a F$$

3. 7

This is the initial pressure that we want to image in PAT images. This pressure wave propagates in 3D space following the forwarding wave equation, which is expressed in equation 3.8

$$\left(\nabla^2 - \frac{1}{v_s^2 \partial t^2} \right) p(\vec{r}, t) = -\frac{\Gamma}{v_s^2} \frac{\partial H(\vec{r}, t)}{\partial t}$$

3. 8

$$H(\vec{r}, t) = \eta_{th} \mu_a F(\vec{r}, t) \qquad\qquad 3.9$$

As we can see from equation 3.8, pressure propagation of the PAT wave follows the propagating wave equation. Thus, solving this equation can provide us the PAT distribution in 3D space. Unfortunately, pressure distribution reconstruction by solving this equation requires 3-D ultrasound transducer, which can record spherical wave, propagates from the pressure source. This type of transducer is very expensive and not suitable for clinical application. Thus, we are using an ultrasound transducer array to capture a portion of the propagating wave. Then apply the similar delay and sum algorithm describes in section 3.1.1 to reconstruct a PAT image. This is certainly not providing the exact initial pressure estimation but provides enough information to diagnose benign and malignant ovarian cancer by providing light absorption related to tissue microvasculature.

3.2 Photoacoustic System Development

PAT has already demonstrated its efficacy in deep tissue imaging [12]. To utilize the advantage of PAT imaging, several systems [13]–[19] has been developed. However, none of them provided real-time US/PAT images. Our group has developed several US/PAT systems for co-registered US/PAT imaging [17][14][20][21]. Alqasemi *et al.* have developed a 128 channel real-time US/PAT system which can provide co-registered US/PAT images at 15 frames per second [21]. This system has been used for both ex-vivo [22] and in-vivo [23] sample study. However, the image quality of the system was degraded over time due to poor connections and grounding.

In this research, we focus on developing a coregistered US/PAT system for in-vivo ovarian cancer characterization. This system utilizes the PAT modality to provide functional parameters of ovarian tumor and structural information can be obtained from US images. Along with the real-

time coregistered US/PAT images, this system can save raw data, which could be utilized to extract other spectral features during offline processing. This system was customized from a commercial US system for real-time coregistered US/PAT data acquisition and processing. A Ti:Sapphire optically pumped Q-switched Nd:YAG laser has been used as a light source. A 3D printed probe holds four optical fibers around the US transducer for shining the tissue sample. During the experiment, data obtained using four wavelengths to calculate oxygen saturation. Wavelength tuning and data saving have been synchronized using a C++ based customized control software loaded on a separate control computer. Different system parameters have been evaluated using phantoms before using it for human subject imaging.

3.2.1 Customizing Commercial Ultrasound System

A commercial US system (EC-12R, Alpinion Medical Systems, Republic of Korea) was programmed to obtain PAT data for this study. This machine can read instructions written in python; thus it is possible to operate it in US, PAT or co-registered US/PAT mode. This system can save raw PAT data, which can be acquired for offline processing and feature extraction. This US system receives ten ns trigger pulse at 15 Hz rate from the laser source and saves one PAT frame data at each trigger pulse. One US frame data was also collected with each PAT frames when operating in co-registered mode. More details regarding the system can be found in [17].

3.2.2 Automatic Wavelength Tuning

In this study, we have used four different wavelengths (740, 780, 800, 830 nm) to illuminate the same spot sequentially and saved the corresponding US and PAT data. Customized software was developed to sweep the wavelengths and collect data automatically. This software can be set to sweep over some fixed wavelengths or a user-defined range of wavelengths with a set interval. This control software was loaded on a laptop, which is connected to the US system using an

Ethernet cable and the motor driver (for wavelength tuning) using a serial port. Along with the in-vivo patient data, we have collected ex-vivo sample data. This software can also control the stage for ex-vivo data collection automatically. The whole control block is shown in Figure 3.5.
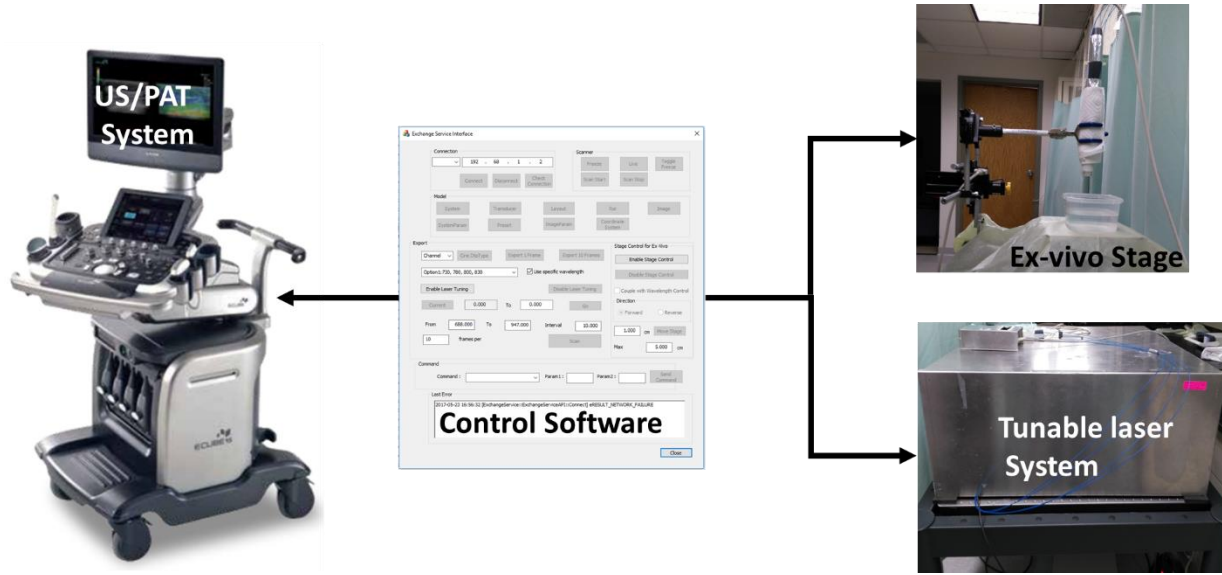
Figure 3. 5 Control block of real-time coregister US/PAT system
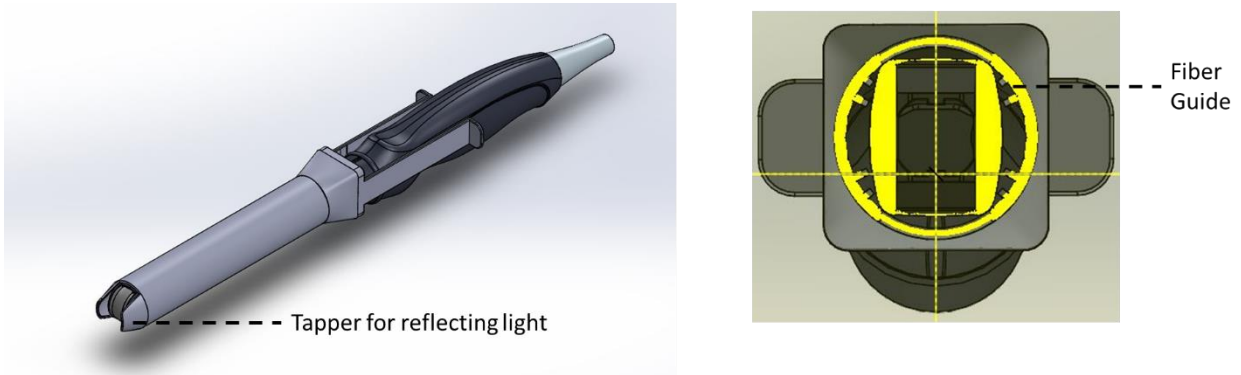
Figure 3. 6 3D printed handheld probe for holding optical fiber around ultrasound transducer

3.2.3 Probe Design

A 128-channel curved trans-vaginal US transducer was used for the study, which has a center frequency of 6 MHz with 80% bandwidth. It has an elevation height of 6 mm and 145.5-degree field of view. Four 1 mm core optical fibers were arranged around the transvaginal probe to deliver light to the sample. A 3D-printed hand-held probe (Figure 3.6) was designed to hold these optical

fibers around the US probe. Inside and outside of the 3D-printed probe was covered by thin aluminum tape with 85% reflection coefficient at 750 nm for high-intensity light output. The position of the optical fibers was determined to obtain optimum light energy at 10 mm away from the probe, which is typical vaginal muscle thickness.

3.2.4 Optical Setup

Optical setup for this system was adapted from the optical setup used in the previous version of real-time PAT system developed by our group [23]. Briefly, A Ti:Sapphire (Symphotics TII, LS-2134, Symphotics, Camarillo, California) optically pumped with a Q-switched Nd:YAG laser (Symphotics-TII, LS-2122) has been used to illuminate the sample orthogonal to the imaging plane of the transducer. The laser can deliver 8 to 12 ns trigger pulses at 15 Hz with tunable wavelength from 680 to 950 nm. A stepper motor (Sigma Koki SGSP-25ACTR-B0) was connected with a crystal to tune the wavelength automatically. A motor driver (LOTIS TII CU 2350) controls this motor, which can receive the command from external PC using a serial port.

Laser output from this system was passed to the four optical fibers through a custom-made lens array that consists of four cylindrical lenses (12.5mm H x 25mm L x 150mm FL Cylinder Lens VIS-NIR Coating, Edmund Optics PCX). This lens array split the incoming beam from the laser into four beams. A 90-10 beam splitter withdraws a portion of the output laser before the incident on the custom-made lens. This splitted laser beam is converted into electrical pulses using a single element US transducer and saved in a computer using a data acquisition card (NI PCI-5112). The saved fluence information is later used for signal normalization. The complete system with the optical setup is shown in Figure 3.7.

3.2.5 Results

System Calibration

Before collecting patient data, system performance was evaluated using phantom experiments. US transparent, opaque blood-filled Silicon tube was inserted inside the chicken breast to mimic the blood vessel inside the vagina muscle wall. Then the chicken breast was merged into 0.04% intralipid solution. Co-registered US/PAT data was collected at different depths for SNR ($20\log_{10}$(max PAT envelope/system noise)) measurements at 780 nm. PAT signal strength was measured from the blood tube location, and the noise was measured after removing the chicken breast. SNR vs. depth plot is shown in Figure 3.8. From the figure, we can see that the SNR is plummeting at 7.3 dB/cm. With this rate, we can obtain a reliable signal (3dB) up to ~3.5 cm. Noise equivalent depth (0 dB) was ~4 cm.
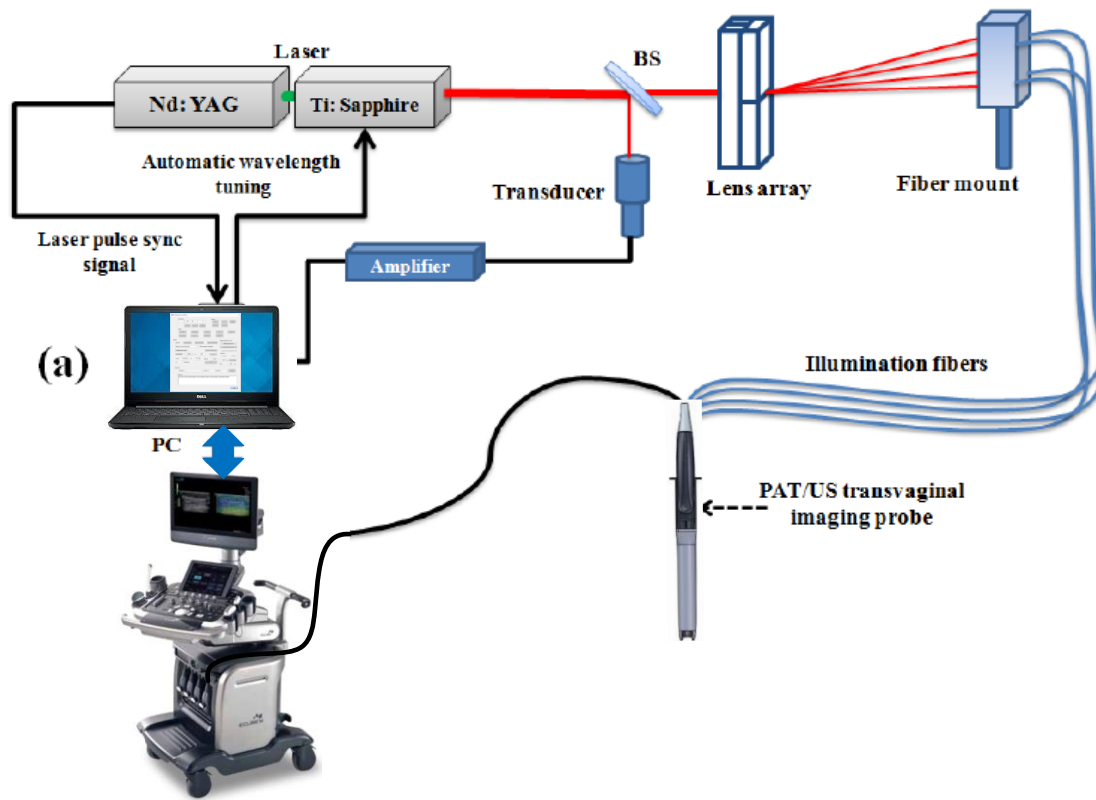
Figure 3. 7 Experimental setup for the real-time co-registered PAT system

The axial resolution of the co-registered US/PAT system is also measured using a 250 µm black thread with 780 nm light. This black thread is placed perpendicular to the imaging plane at the 0-degree position and worked as a point source. PAT signal coming from the black thread was measured after putting it inside a water tank at four different depths from 0.5 to 2 cm with 0.5 cm interval. Then FWHM was calculated from the fitted Gaussian curve after deconvolution with the transfer function of the transducer. The measured axial resolution was 250.25±44.45 µm.
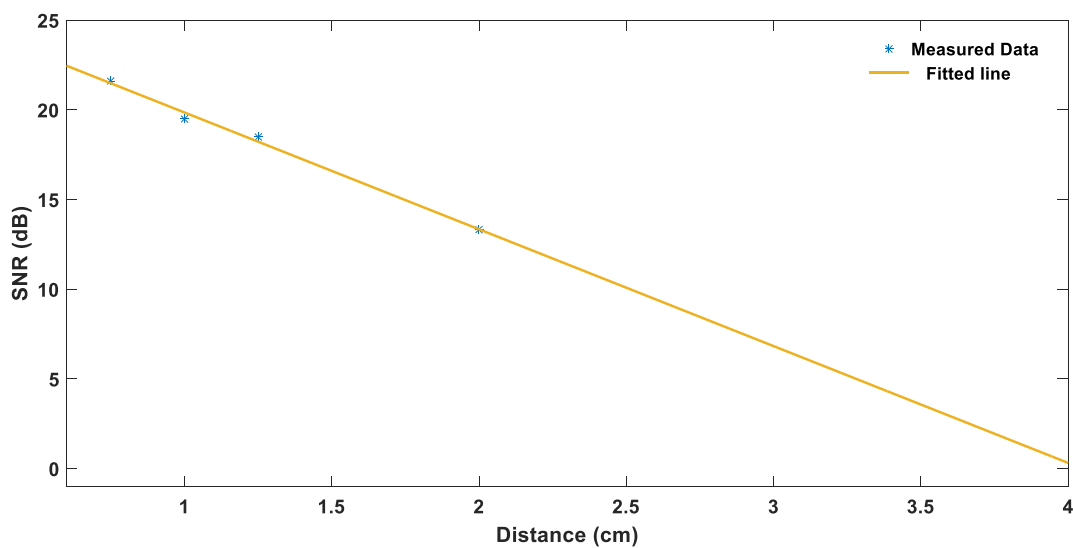
Figure 3. 8 Depth vs SNR

Clinical Results

From February 2017 to November 2017, 16 patients were enrolled for ovarian tumor imaging at the Siteman Cancer Center of Washington University in St. Louis. These patients were at risk for ovarian cancer or had an ovarian or pelvic mass suggestive of malignancy. The study protocol was approved by the institutional review board (IRB) and compliant with the Health Insurance Portability and Accountability Act (HIPAA). Written informed consent was obtained from all patients. Before imaging with the PAT/US system, all the patients were imaged by a radiologist (CS, or CR) assisted by a US technician using a commercial transvaginal US system of GE. After

examining the suspicious ovaries or pelvic mass, the commercial probe was then withdrawn, and the customized PAT/US probe was inserted transvaginally to image the suspicious masses. For each imaging location, 5-10 PAT and US frames were recorded for all four wavelengths.

Of the 16 patients, one patient did not have any ovarian mass found from US imaging prior to PAT/US imaging, and one patients' data was not recorded properly due to system related problems. For the rest 14 patients, one patient had one ovary detected by the commercial ultrasound system; however, the location was too deep (> 5 cm) for PAT/US imaging. Of the total 13 (mean age 52 years, range 37 to 63 years) patients, one patient's data was recorded only for a single wavelength (780 nm) due to laser tuning problem and this patient's data was used for spectral analysis. For the rest of 12 patients, six patients had one ovary due to prior surgeries or cannot find from the commercial US system. As a result, 18 ovaries from 12 patients were imaged with co-registered PAT/US system and consisted of high grade serous carcinomas (n=2) and endometrioid adenocarcinoma (n=3), serous borderline tumors (n=2), sex code stromal tumor (n=1), benign fibrothecoma (n=2) and normal ovaries (n=2), benign cystic ovaries (n=6). The patient information and diagnosis based on surgical pathology are provided in Table 3.1. Example of an invasive cancer and a benign ovarian mass are presented in Figures 3.9.

Table 3. 1 Patient characteristics and surgical pathology of ovaries

Patient	Age (y)	Menopausal status	Serum CA125 (U/ml)	Surgical pathology of the tubes and ovaries
001 (n=2)	37	pre	85.4	Right ovary (4.5 cm): serous borderline tumor Left ovary (9.5 cm): serous borderline tumor

002 (n=2)	55	pre	2442	Right ovary (11.5 cm): high-grade serous carcinoma, involving the ovarian parenchyma and surface Left ovary (8.5 cm): high-grade serous carcinoma, involving the ovarian parenchyma and surface
003 (n=2)	63	post	93	Right ovary (3 cm): endometrioid adenocarcinoma, well-differentiated; steroid cell tumor Left ovary: no histopathologic abnormality
004 (n=1)	61	post	16.3	Left ovary (13 cm): fibrothecoma
005 (n=2)	50	pre	116.3	Right ovary (8.3 cm): endometrioid adenocarcinoma, well differentiated, involving ovarian surface Left ovary (20 cm): endometrioid adenocarcinoma, well differentiated, not involving ovarian surface
006 (n=2)	57	post	19	Right ovary (5 cm): serous cystadenoma Left ovary (3 cm): cystic follicles
007 (n=1)	42	post	11.4	Left ovary (19.2 cm): Sertoli-Leydig cell tumor, intermediate/moderate differentiation, not present on ovarian surface)
008 (n=1)	42	pre	111.2	Right ovary (6 cm): cystic endometriosis
009 (n=2)	57	post	23.6	Right ovary (7 cm): mucinous cystadenoma Left ovary (2.1 cm): no histopathologic abnormality
010 (n=2)	47	pre	48.1	Right ovary (7.6 cm): epidermoid cyst Left ovary: epidermoid cyst
011 (n=1)	53	post	84	Right ovary (5.2 cm): cystic atretic follicles

				Left ovary (3.7 cm): benign simple cyst, focal endometriosis
012 (n=1)	43	post	N/A	Left ovary: cyst (ruptured)
013 (n=2)	49	pre	28.7	Right ovary (2.2 cm): complex cyst Left ovary: complex cyst
014 (n=2)	68	post	845.2	Right ovary (10 cm): high-grade serous carcinoma Left ovary (10 cm): high-grade serous carcinoma
015 (n=1)	34	pre	11.3	Right ovary (6 cm): mature teratoma (dermoid cyst)
016 (n=2)	60	post	161.3	Right ovary (5.5 cm): high-grade serous carcinoma Left ovary (2.8 cm): high-grade serous carcinoma

3.3 Photoacoustic Image Processing and Ovarian Cancer Diagnosis

With our customized system, we can save co-registered US and PAT images. The spread of the PAT signals overlay on top of the US image provides useful information regarding ovarian cancer diagnosis. However, the reconstructed PAT/US images only display normalized amplitude; there are other information we can extract from the raw or beamformed signals, which can be used to make a better judgment regarding ovarian tumor. After building a robust system, we focused on extracting useful features for the automatic diagnosis of ovarian tumors. From US and PAT images of 16 patients, we have extracted a total of 7 features which is then used statistically analyzed to get the significance of these features in benign and malignant tumor classification. Logistic regression classifier was trained to check the automatic diagnosis of the tumors.
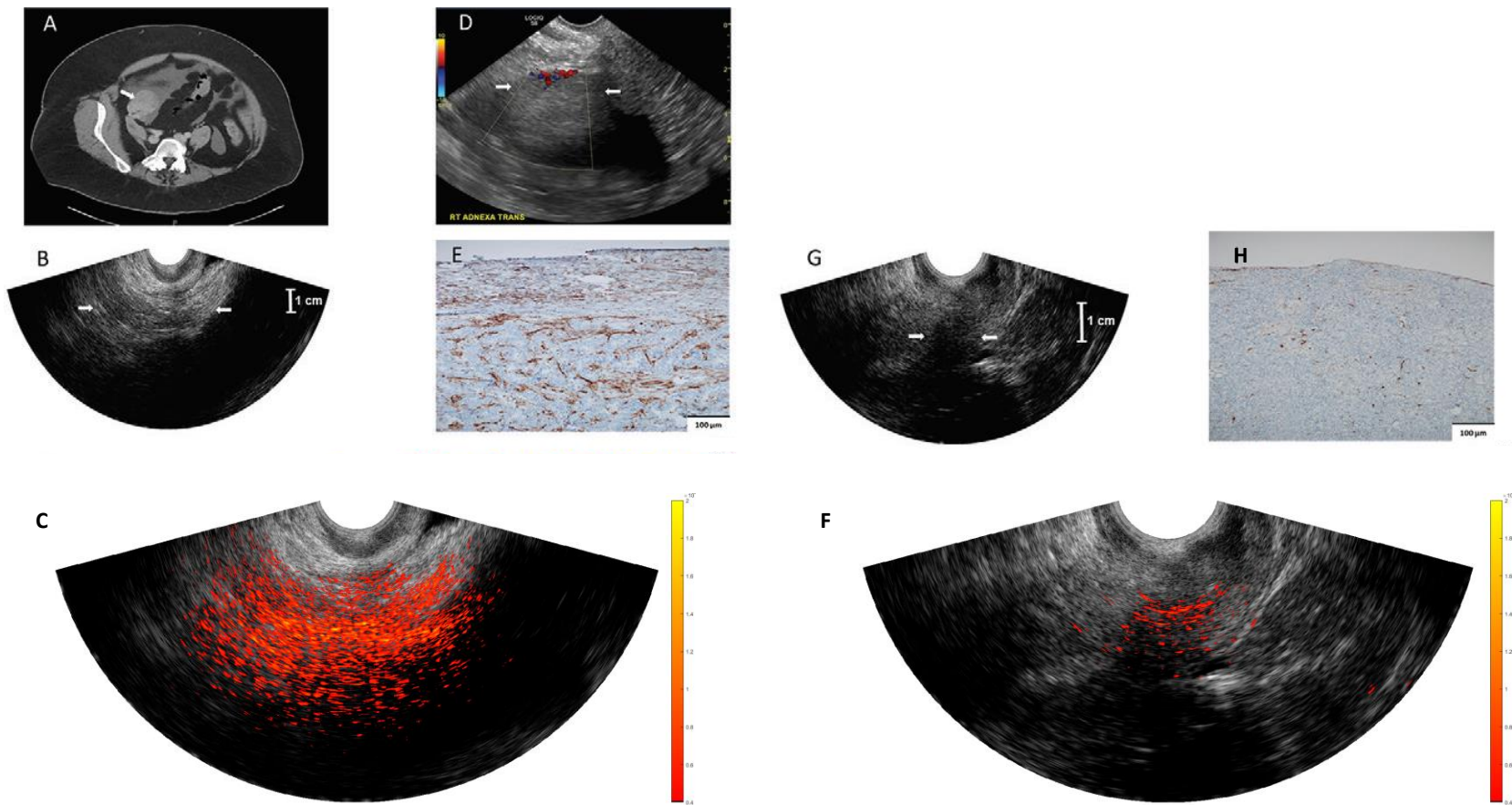
Figure 3. 9 Images in a 63-year-old woman after menopause who had a solid right adnexal mass measuring up to 4.5 cm, ascites, and a thickened endometrium at contrast-enhanced CT (patient 3). A. Contrast-enhanced CT image. Pathologic findings included a 5-cm ovary (arrow) with well-differentiated stage II endometrioid adenocarcinoma and an incidental 2.2-cm benign steroid cell tumor. B. US image (EC-12R; Alpinion Medical Systems) of the right adnexa (arrows). C. The coregistered US and photoacoustic tomography shown in color, with extensive diffused vascular distribution covering a large area of the region of interest in the depth range of 1–4 cm of a malignant tumor. D. US Doppler image (Logiq 8S; GE Healthcare) of the right adnexa shows a hypoechoic soft tissue mass with minimal peripheral flow on color Doppler images (arrows). E. CD31 immunostaining in the suture area, showing numerous and extensive microvessels; F. Coregistered US and photoacoustic tomography of benign tumor shows scattered photoacoustic tomography signals. G. US image of the left ovary (arrows). H. CD31 immunostaining of surgical sample histopathologic abnormalities.

3.3.1 Feature Detection and Classification

Independent Area Selection

For each patient, we have collected several sets of data from each view of the ovary. Before extracting features, it is necessary to find independent frames to avoid duplicating features. To select independent frames only for avoiding correlated features and potentially biased classification, the 2-D cross-correlation of the US images was measured between two data sets. Before applying the cross-correlation operator, both images were normalized within their range to avoid intensity mismatch. Finally, a hierarchical clustering method was applied to make two clusters (dependent frames and independent frames) [24]. Hierarchical clustering generates a dendrogram based on the feature distance among the samples. Dendrogam is a tree diagram used in higherarchical clustering to demonstrate the relationship between the samples to be clustered. Samples, which have lower distances according to their features, are placed close in the dendrogram, and higher distance samples are set far away. The height of their connected branches is also varied according to their feature distance. The dendrogram was then cut automatically to obtain two clusters using a threshold on 50% of the maximum distance. Dendrogram of a patient data is given in Figure 3.10. This figure shows two clusters connected with a blue line. The distance between these two clusters are maximum. One cluster has a high cross-correlation coefficient, which are dependent frames and other with low cross-correlation coefficient is considered as independent frames. Features from all dependent frames were averaged, and one feature from each independent area was introduced to the classifier. A total of 20 independent benign frames and 17 independent malignant frames from all patient data were included for classification. Flow chart of the independent area selection algorithm is presented in Figure 3.11.
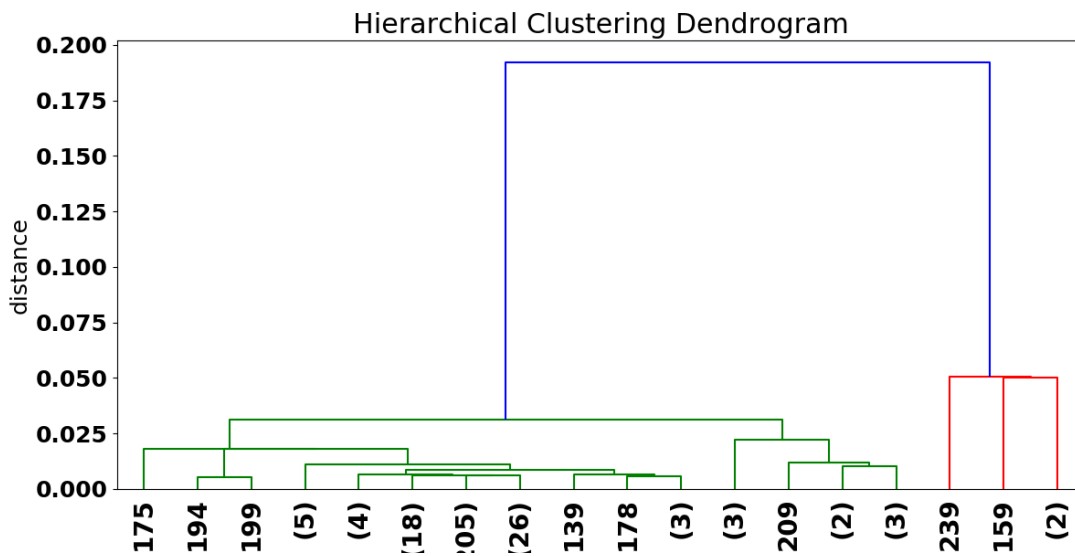
Figure 3. 10 Dendogram for applying hierarchical classifier for independent frame selection
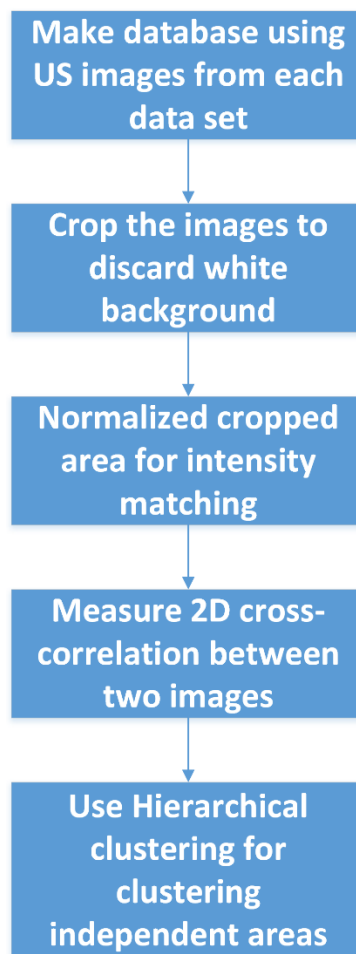
Figure 3. 11 Block diagram for independent frame selection algorithm

Feature Extraction

Three spectral features from PAT data (maximum SS, MBF and MHz intercept) and three spectral features from US data (maximum SS, MBF, and 0 MHz intercept) were quantitatively extracted. PAT spectral features such as SS, MBF, and 0 MHz intercept are related to the absorber's size and concentration and the spectral features from US signals are connected to the scatterer size, concentration and acoustic impedance [25] [26]. Menopausal condition of the patient (i.e. pre-menopausal or post-menopausal) was not considered to be a significant feature, as both pre and post-menopausal malignancies were reported in the current study (Table 1).

For calculating spectral features, an angular window was applied on the beam data to separate the region of interest (ROI) from the rest of the tissue. A Hamming window was applied on the truncated data to minimize the side lobes. The power spectrum of each beam was then calculated using a fast Fourier Transform (FFT). Any beam lower than 10 dB of the maximum beam data were discarded to reduce the effect of noise. The Power spectrum of the beams inside the ROI was normalized by the power spectrum of a known phantom at different depths (250 µm black thread for PAT and a planar reflector for the US) [21][27]. The approximate point-like target characterizes the frequency response of the transducer and the electric receiving system. Finally, a line was fitted to the average normalized spectrum within 80% bandwidth of the transducer's central frequency (6 MHz). From the fitted line, maximum SS, MBF and 0-MHz intercept were measured. Similar spectral information (maximum SS, MBF and 0-MHz intercept) is also extracted from US beam data. As the PAT spectral features for all four wavelengths were highly correlated, hence only one wavelength (780 nm) features were used for classification purpose.
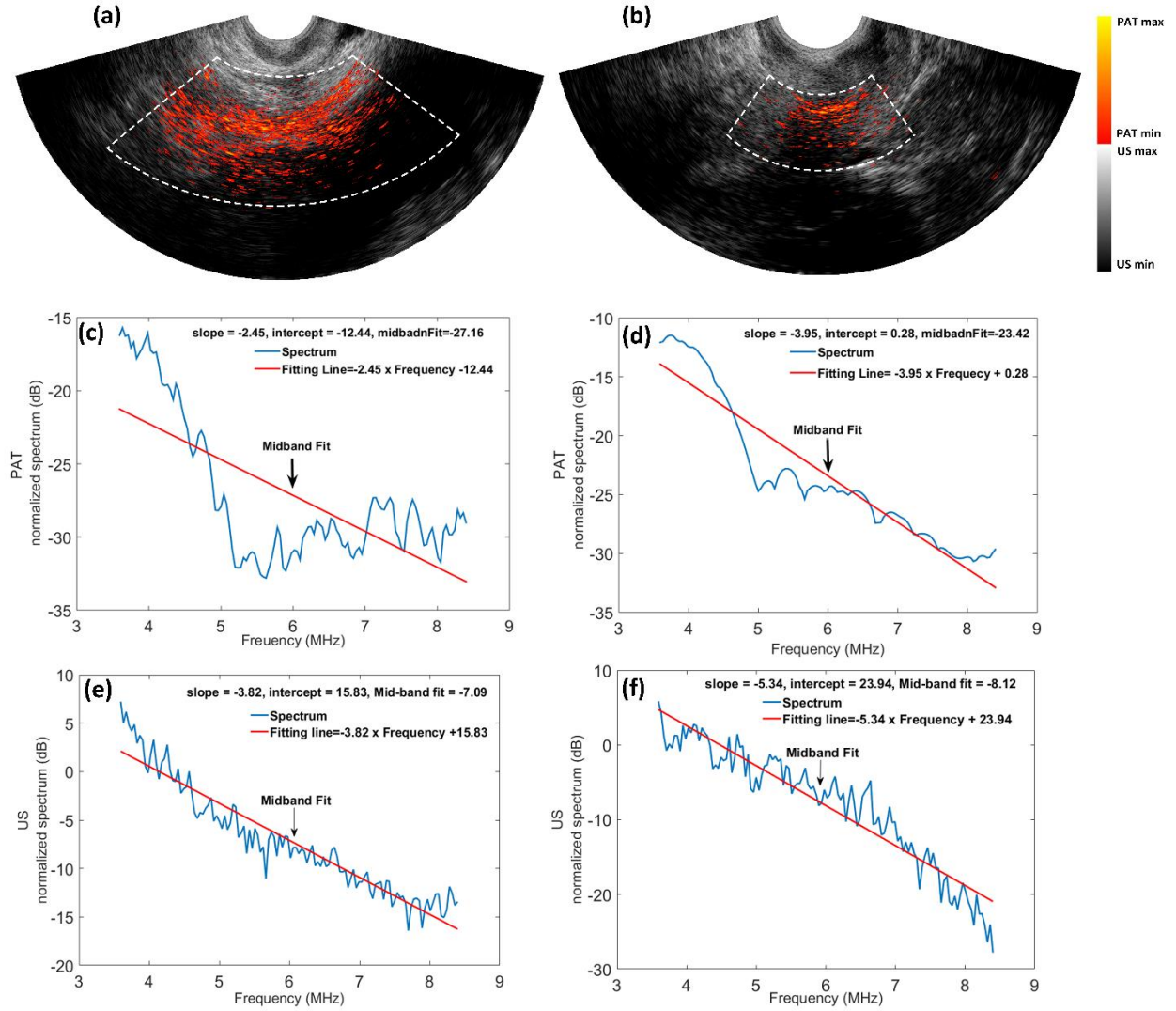
Figure 3. 12 (a) *In vivo* coregistered PAT/US image of the patient with an endometrioid adenocarcinoma of right ovary marked by ROI. (b) *In vivo* coregistered PAT/US image of the same patient with a normal left ovary marked by ROI. In (a) and (b), the angular ROI defines the region where the beam spectrum feature is extracted. (c) The spectrum (blue) and linear fitting (red) of PAT beam as well extracted parameters from (a). (d) The spectrum (blue) and linear fitting (red) of PAT beam as well as extracted spectral parameters from (b). (e) The spectrum (blue) and linear fitting (red) of US beam as well as extracted spectrum parameters from (a). (f) The spectrum and linear fitting of US beam as well as extracted spectrum parameters from (b).

Feature Selection

Some dependent features have been excluded for training and testing to avoid training with non-significant features. The Spearman's rank correlation coefficient (ρ) between two features was determined to measure their dependencies, and excluded the features with $|\rho| > 0.5$. Seven

features (3 PAT features, 3 US features, and CA-125) were initially calculated and based on the correlation coefficient, three features (PAT 0-MHz intercept, US midband fit and US maximum spectral slope) were excluded. The remaining four significant features were used for training and testing of a logistic classifier model. Table 3.2 is showing the correlation between the two pairs of features.

Table 3. 2 Cross-correlation between features

	Max. PAT SS	PAT 0-MHz intercept	PAT MBF	Max. US SS	US 0-MHz intercept	US MBF
Maximum PAT SS	1	-0.65	0.201	-0.061	0.029	-0.091
PAT 0-MHz intercept		1	0.546	0.284	-0.282	0.202
PAT MBF			1	0.122	-0.129	0.006
Max. US SS				1	-0.908	0.804
US 0-MHz intercept					1	-0.785
US MBF						1

Classification

A logistic regression model is a widely used binary classifier, which can describe the relationship between several predictor variables $X_1, X_2, \dots X_n$ and dichotomous response variable Y (0 for benign/normal and 1 for malignant). In this study, a logistic model was used for classification of benign/normal and malignant ovaries, using PAT and US features as well as CA-125 level. The logistic model was trained using the GLMFIT function in MATLAB, and the coefficients obtained from the trained model was used for testing using GLMVAL function. The accuracy of both the training and testing models were evaluated for sensitivity, specificity, positive predictive value

(PPV), negative predictive value (NPV) as well as the area under the receiver operating characteristics (ROC) curve (AUC).

Table 3. 3 Mean value of features and their t-test p values

Feature name	Mean value (malignant n=17)	Mean value (benign n=20)	p value
Maximum spectral slope (PAT) (dB/MHz)	1.06±1.49	0.61±1.47	0.378
PAT 0-MHz intercept (dB)	-19.16±5.39	-16.56±5.39	0.164
PAT mid-band fit (dB)	-20.36±10.32	-19.48±6.5	0.771
Maximum spectral slope (US) (dB/MHz)	-0.34±2.25	-0.46±1.77	0.853
US 0-MHz intercept (dB)	11.16±9.97	13.82±7.03	0.379
US mid-band fit (dB)	-4.75±2.81	-4.55±2.65	0.834
CA-125 (units/ml)	634.55±1003.17	48.53±35.55	0.033

ROC curve was calculated by varying the threshold from 0 to 1 at 0.01 interval [28]. For each threshold, sensitivity, specificity, PPV and NPV were recorded by selecting the training and testing samples 20 times. For each iteration, 20 (13 benign and 12 malignant) samples were randomly selected for training and the rest for testing. Average of these 20 iterations provide one sensitivity and specificity; we obtained 101 sensitivity and specificity from 101 thresholds. This set of sensitivity and specificity was finally used for obtaining the ROC curve for each model. We obtained 101 AUC values (each AUC value was the average of 20 AUC values from different

sample combinations for training and testing) for each threshold using the "perfcurve" function from MATLAB (2015a).

3.3.2 Results

Table 3.3 shows the mean and standard deviation of features extracted from benign/normal group and invasive epithelial ovarian cancer group and their p values. Figure 3.13 shows the box plots of four features of CA-125, PAT midband fit, US 0-MHZ intercept, PAT maximum spectral slope. Correlated features as given in Table 3.2 were not included in the box plots. Figure 3.14 shows the AUC for the combination of most significant two PAT features, one US feature and CA-125 for randomly selected testing data.
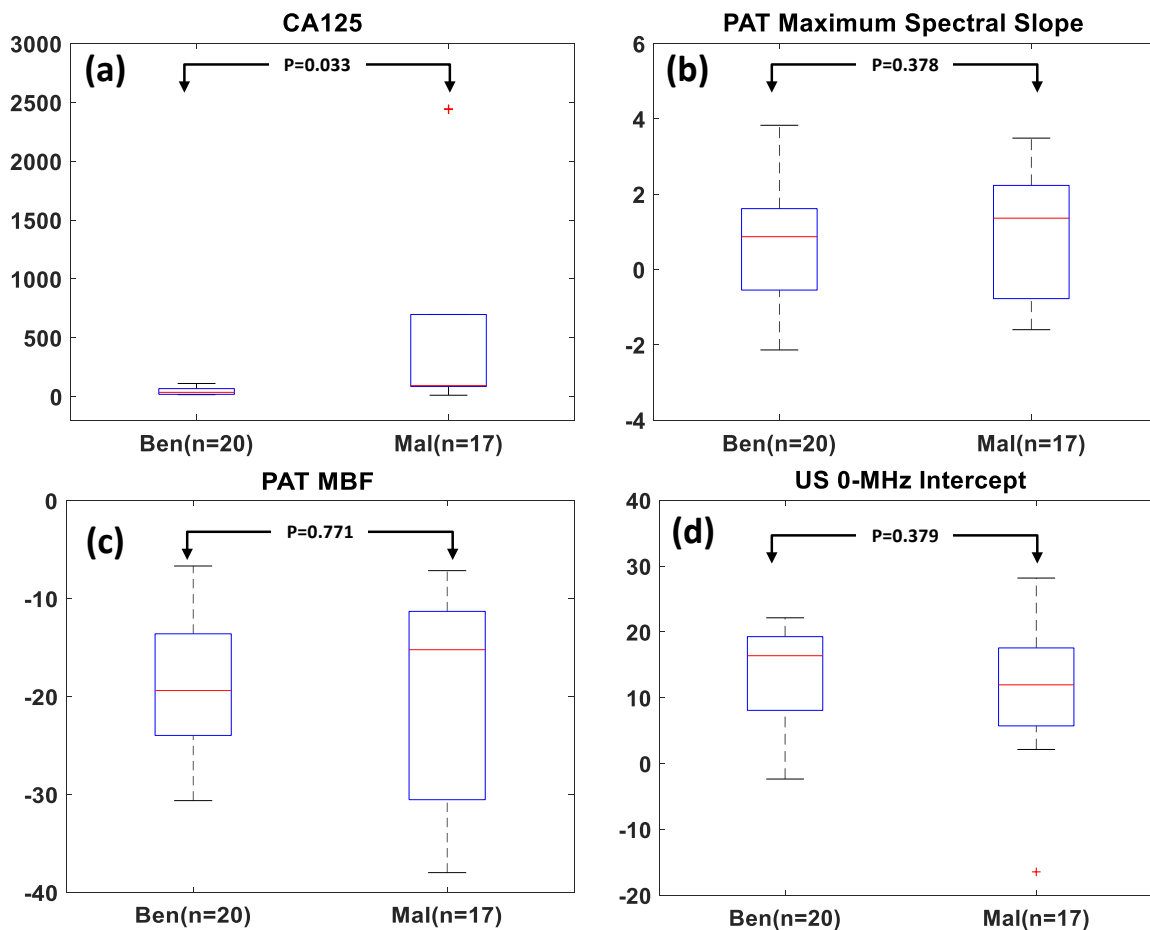
Figure 3. 13 Boxplot with p-values for selected four features
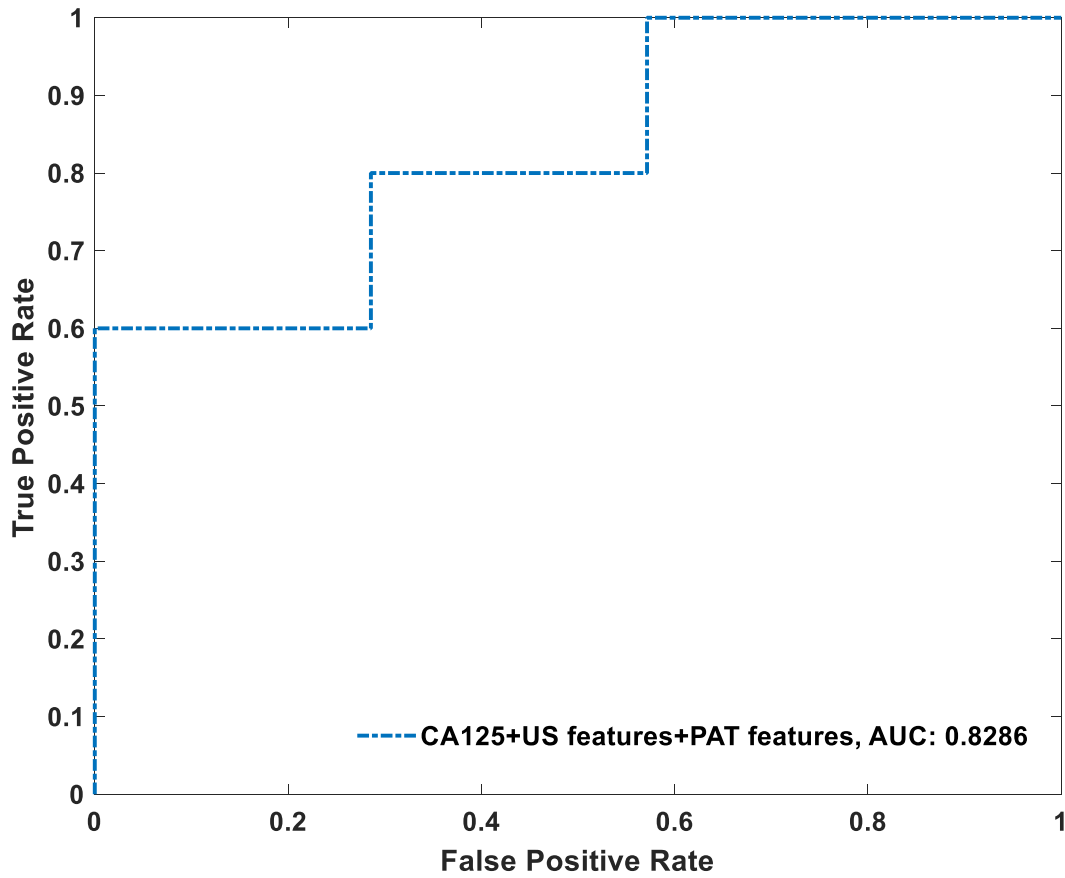
Figure 3. 14 ROC for testing logistic regression model with four features (2 PAT, 1 US and CA125)

3.4 Co-registered Doppler for Improving Region of Interest Selection of Photoacoustic Imaging

Although this system provides distinguishable PAT images and features for benign and malignant tumors, during in-vivo studies, some ovaries are difficult to identify and PAT signal origin is unclear due to the presence of large blood vessels near the target location. The celiac artery carries a large amount of blood and often shows up near the ovary. Figure 3.15 shows a co-registered US-PAT image of a benign ovary marked by the circle. However, strong PAT signals (overlays in red on top of grey US images) are coming from the side and bottom of the ovary. For this type of image, it is difficult to select the region of interest (ROI) for PAT data analysis. In this work, we

have provided a solution for this problem by reconstructing the Doppler images using the co-registered US data. Since the Doppler signal is only coming from the large blood vessels, using high US frame rate (1200 Hz), we can identify PAT signals coming from the blood vessels. Finding of a phantom study is presented here to prove the efficacy of this technique.
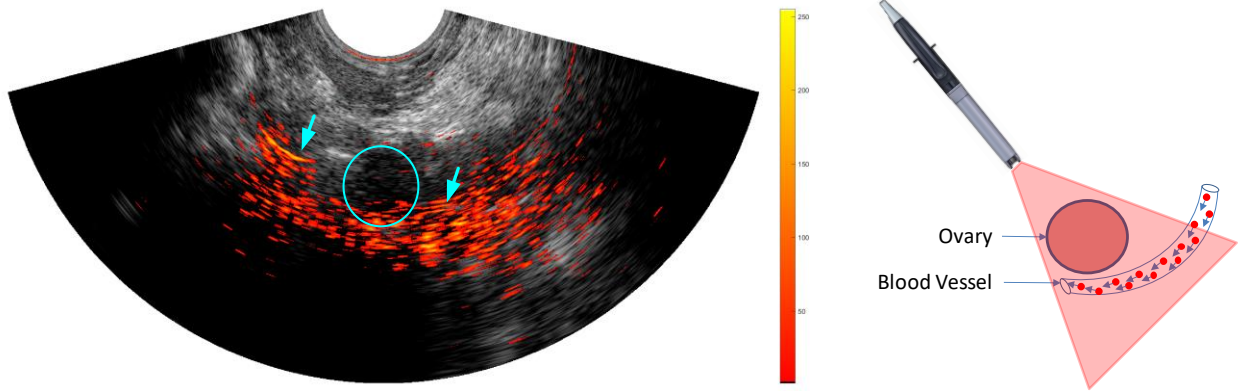
Figure 3. 15 PAT Signal coming from surrounding the blood vessel

3.4.1 Experimental Setup

For demonstrating the performance of the proposed solution, we have used a silicon phantom with an absorption coefficient of 0.2 cm^{-1} to emulate a malignant ovary. Indian ink was used to add the absorption to the phantom, and the amount was controlled to obtain the desired absorption coefficient. Details phantom fabrication procedure can be found in [29]. Blood mimicking fluid was created by mixing 1.7×10^4 cm^{-3} 30 µm glass spheres (Model 3000E, Poterrs Industries LLC, Valley Forge, PA, USA) with water and glycol mixer with a specific gravity of 1.043 g/cm^3. A small amount of Indian ink was mixed with this solution to add absorption. US scattering was coming from the glass spheres, and Indian ink provides the PAT absorption as was expected in blood. This mixed fluid was then pass through a transparent polyethylene tube of inner diameter of 500 µm. A variable speed peristaltic pump (Masterflex, Cole-Parmer, Vernon Hills, IL, USA) was used to pump the blood mimicking fluid through the polyethylene tube. Ovary mimicking

phantom was attached on top of the tube during the experiment. The schematic of the experiment is given in Figure 3.16.
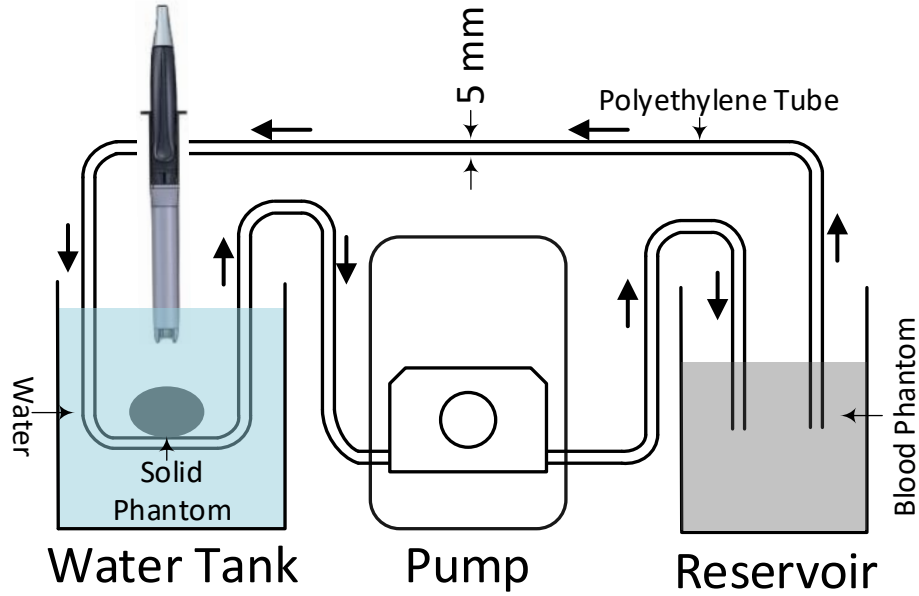
Figure 3. 16 Schematic of the experimental setup

3.4.2 Doppler Image Reconstruction

The flow velocity of the blood mimicking fluid through the tube was calculated by estimating the phase difference between two consecutive frames. Ideally, only two frames are enough to obtain US Doppler images. However, in practice, it is not feasible. We have saved 12 frames for each Doppler frame estimation. During the experiment, RF data of one PAT frame and 12 ultrasound frames are saved for each location. US data was saved at 1200 frames per second. This frame rate is fast enough to estimate the velocity of ±16 cm/s. Though celiac artery can have blood flow at around 40 cm/s, we keep this low velocity because of the speed limit of the pump. These channel data are used to estimate US envelope data for these US frames. Finally, the phase map is estimated using the cross-correlation method to obtain Doppler images after delay line cancellation. This delay line canceller discarded the signal coming from the stationary or slow moving artery wall

movement, which provides a strong reflection in US images. 2nd order Butterworth IIR filter was used to implement the delay line canceller. Block diagram of the Doppler flow reconstruction is presented in Figure 3.17.
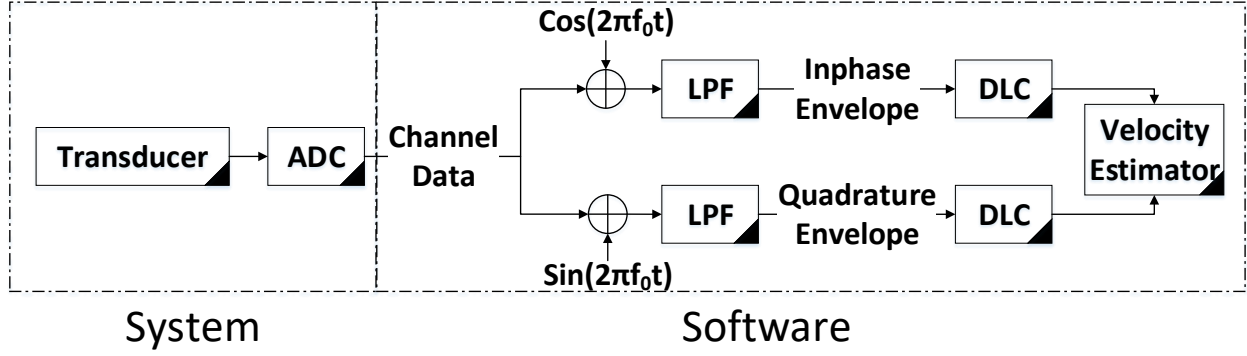
Figure 3. 17 Doppler image reconstruction flow

3.4.3 Results

To validate the Doppler algorithm, we have passed the blood mimicking fluid through the polyethylene tube at various speed from 6 cm/s to 14 cm/s at 1 cm/s interval using the pump. The actual average speed of the fluid was recorded using the power Doppler mode of the ultrasound system. The average velocity was also calculated from the reconstructed flow map. Figure 3.18 shows the comparison between estimated velocity from the Doppler images and original velocity set by the pump. In the test setup described above, the silicon phantom works as a stationary absorber and the tube full of blood mimicking fluid works as a blood vessel. PAT signal is originated from both stationary phantom and fluid, but the Doppler signal is only coming from the fluid mixer. Thus, comparing both we can conveniently locate the ovary location and select our region of interest as demonstrated in Figure 3.19.
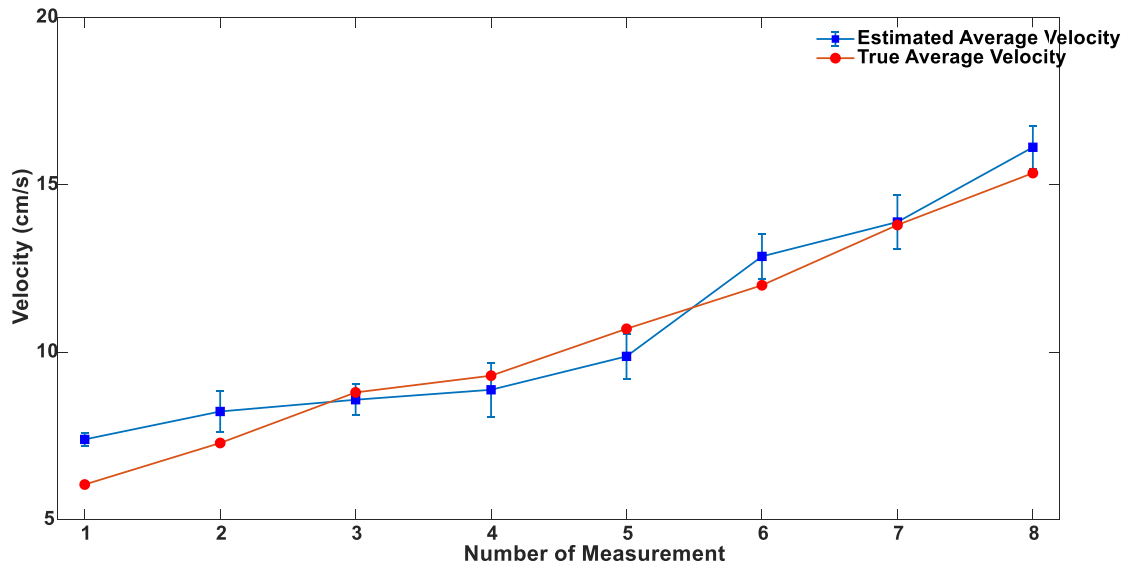
Figure 3. 18 Velocity comparison between true velocity and estimated velocity

Co-registered US/PAT Image   US Doppler Image
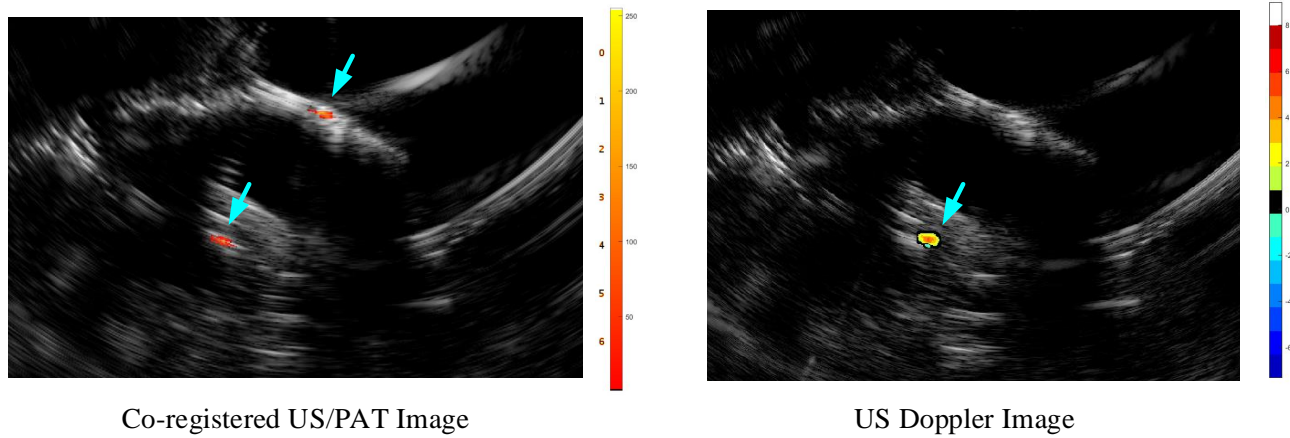
Figure 3. 19 Doppler assisted ROI selection for coregistered US/PAT image

3.5 Summary

This chapter described the technology developments that I have accomplished in the field of photoacoustic tomography during my Ph.D. research. Developing a robust and stable system for PAT application in the clinical setting was a big challenge for advancing this technology. This has been done by customizing a commercial ultrasound system. The custom designed control software was able to coordinate several systems for obtaining the most stable outcome during in-vivo and

ex-vivo study. This system has created the opportunity to study the performance of PAT not only for ovarian cancer diagnosis but also for other organs (colon, rectum, cervix, etc) [30].

After developing the system, a pilot study with 16 ovarian tumor patients was performed using this system. Reconstructed images and extracted features show significant difference thus validates the performance of this system. Though the reported features in this dissertation do not show the best statistical significance, further improvement has been achieved by using better calibration method. One practical problem related to PAT feature extraction was improved by using co-registered US Doppler information. Necessary software modifications were done to automatic scan and store multiple modality data during the study. This automatic storage capability made the system very easy to use in clinical settings. US Doppler image reconstruction will be extended in the future for PAT Doppler reconstruction which will provide additional information (oxygen consumption [31]) regarding ovarian cancer detection.

Reference

[1]   A. G. Bell, "The Production of Sound by Radiant Energy," *Science (80-.).*, vol. 2, no. 48, pp. 242–253, 1881.

[2]   X. Wang, Y. Pang, G. Ku, X. Xie, G. Stoica, and L. V Wang, "Noninvasive laser-induced photoacoustic tomography for structural and functional in vivo imaging of the brain," *Nat. Biotechnol.*, vol. 21, p. 803, Jun. 2003.

[3]   "American Cancer Society - Cancer Facts & Statistics," *American Cancer Society*, 2019. [Online]. Available: https://cancerstatisticscenter.cancer.org/#/.

[4]   V. Nossov *et al.*, "The early detection of ovarian cancer: from traditional methods to proteomics. Can we really do better than serum CA-125?," *Am. J. Obstet. Gynecol.*, vol. 199, no. 3, pp. 215–223, 2008.

[5]   J. Tammela and S. Lele, "New modalities in detection of recurrent ovarian cancer," *Curr. Opin. Obstet. Gynecol.*, vol. 16, no. 1, pp. 5–9, 2004.

[6]   M. Goozner, "Personalizing ovarian cancer screening.," *J. Natl. Cancer Inst.*, vol. 102, no. 15, pp. 1112–1113, 2010.

[7]   A. Shaaban and M. Rezvani, "Ovarian Cancer: Detection and Radiologic Staging," *Top. Magn. Reson. Imaging*, vol. 21, no. 4, pp. 247–259, 2010.

[8]   S. Funt and H. Hricak, "Ovarian Malignancies," *Top. Magn. Reson. Imaging*, vol. 14, no. 4, pp. 329–338, 2003.

[9]   R. E. Bristow, R. L. Giuntoli, H. K. Pannu, R. D. Schulick, E. K. Fishman, and R. L. Wahl, "Combined PET/CT for detecting recurrent ovarian cancer limited to retroperitoneal lymph nodes," *Gynecol. Oncol.*, vol. 99, no. 2, pp. 294–300, 2005.

[10]   E. J. Feleppa *et al.*, "Typing of prostate tissue by ultrasonic spectrum analysis," *IEEE Trans. Ultrason. Ferroelectr. Freq. Control*, vol. 43, no. 4, pp. 609–619, 1996.

[11]   J. L. Prince and J. M. Links, *Medical imaging signals and systems*. Pearson Prentice Hall Upper Saddle River, NJ, 2006.

[12]   M. Xu and L. V Wang, "Photoacoustic imaging in biomedicine," *Rev. Sci. Instrum.*, vol. 77, no. 4, p. 41101, 2006.

[13]   S. A. Ermilov *et al.*, "Development of laser optoacoustic and ultrasonic imaging system for breast cancer utilizing handheld array probes," in *Proc.SPIE*, 2009, vol. 7177.

[14]   A. Aguirre *et al.*, "Coregistered three-dimensional ultrasound and photoacoustic imaging system for ovarian tissue characterization," *J. Biomed. Opt.*, vol. 14, no. 5, p. 054014, 2009.

[15]   T. Harrison, J. C. Ranasinghesagara, H. Lu, K. Mathewson, A. Walsh, and R. J. Zemp, "Combined photoacoustic and ultrasound biomicroscopy," *Opt. Express*, vol. 17, no. 24,

pp. 22041–22046, Nov. 2009.

[16] R. G. M. Kolkman, P. J. Brands, W. Steenbergen, and T. G. C. van Leeuwen, "Real-time in vivo photoacoustic and ultrasound imaging," *J. Biomed. Opt.*, vol. 13, no. 5, pp. 1–4, Sep. 2008.

[17] P. Guo, J. Gamelin, S. Yan, A. Aguirre, and Q. Zhu, "Co-registered 3-D ultrasound and photoacoustic imaging using a 1.75D 1280-channel ultrasound system," in *Proc.SPIE*, 2007, vol. 6437.

[18] S. Sethuraman, S. R. Aglyamov, J. H. Amirian, R. W. Smalling, and S. Y. Emelianov, "Development of a combined intravascular ultrasound and photoacoustic imaging system," in *Proc.SPIE*, 2006, vol. 6086, no.

[19] J. J. Niederhauser, M. Jaeger, R. Lemor, P. Weber, and M. Frenz, "Combined ultrasound and optoacoustic system for real-time high-contrast vascular imaging in vivo," *IEEE Trans. Med. Imaging*, vol. 24, no. 4, pp. 436–440, Apr. 2005.

[20] U. Alqasemi, H. Li, A. Aguirre, and Q. Zhu, "FPGA-based reconfigurable processor for ultrafast interlaced ultrasound and photoacoustic imaging," *IEEE Trans. Ultrason. Ferroelectr. Freq. Control*, vol. 59, no. 7, pp. 1344–1353, 2012.

[21] U. Alqasemi, H. Li, G. Yuan, P. Kumavor, S. Zanganeh, and Q. Zhu, "Interlaced photoacoustic and ultrasound imaging system with real-time coregistration for ovarian tissue characterization," *J. Biomed. Opt.*, vol. 19, no. 7, p. 076020, 2014.

[22] H. Li, P. Kumavor, U. Salman Alqasemi, and Q. Zhu, "Utilizing spatial and spectral features of photoacoustic imaging for ovarian cancer detection and diagnosis," *J. Biomed. Opt.*, vol. 20, no. 1, p. 16002, Jan. 2015.

[23] H. S. Salehi *et al.*, "Coregistered photoacoustic and ultrasound imaging and classification of ovarian cancer: ex vivo and in vivo studies," *J. Biomed. Opt.*, vol. 21, no. 4, p. 46006, Apr. 2016.

[24] S. C. Johnson, "Hierarchical clustering schemes," *Psychometrika*, vol. 32, no. 3, pp. 241–254, 1967.

[25] W. D. W. Heston *et al.*, "Typing of prostate tissue by ultrasonic spectrum analysis," *IEEE Trans. Ultrason. Ferroelectr. Freq. Control*, vol. 43, no. 4, pp. 609–619, 2002.

[26] G. Xu, I. A. Dar, C. Tao, X. Liu, C. X. Deng, and X. Wang, "Photoacoustic spectrum analysis for microstructure characterization in biological tissue: A feasibility study," *Appl. Phys. Lett.*, vol. 101, no. 22, 2012.

[27] H. Tadayyon *et al.*, "A priori Prediction of Neoadjuvant Chemotherapy Response and Survival in Breast Cancer Patients using Quantitative Ultrasound," *Sci. Rep.*, vol. 7, p. 45733, Apr. 2017.

[28] D. J. Hand and R. J. Till, "A Simple Generalisation of the Area Under the ROC Curve for Multiple Class Classification Problems," *Mach. Learn.*, vol. 45, no. 2, pp. 171–186, 2001.

[29]   H. Vavadi *et al.*, "Compact ultrasound-guided diffuse optical tomography system for breast cancer imaging," *J. Biomed. Opt.*, vol. 24, no. 02, p. 1, 2018.

[30]   G. Yang *et al.*, "Co-registered photoacoustic and ultrasound real-time imaging of colorectal cancer: ex-vivo studies," in *Proc.SPIE*, 2019, vol. 10878.

[31]   Y. Jiang, A. Forbrich, T. Harrison, and R. J. Zemp, "Blood oxygen flux estimation with a combined photoacoustic and high-frequency ultrasound microscopy system: a phantom study," *J. Biomed. Opt.*, vol. 17, no. 3, p. 036012, 2012.

4 Summary

4.1 Summary

The goal of this research was to improve the design of optical imaging technologies for cancer monitoring and diagnosis. Improvement has been achieved in both system design and algorithm development, making diffuse optical tomography and photoacoustic tomography potentially more user-friendly and suitable for clinical use.

To improve diffuse optical tomography, several system-level designs were altered to reduce the cost and space required by the previous design. These modifications also improved system control, which enhanced system performance and user-friendliness. Implementing advanced interference reduction techniques enabled the same system performance as before, even after different components were closely spaced for compactness. Homemade electronics not only reduced the cost of the system development but also accommodated other requirements necessary for achieving a compact system. The FPGA firmware of the data acquisition board and computer software was modified to allow controlling the system through a single computer interface.

Optical image reconstruction in diffuse optical tomography is dependent on tumor size and location measurements from the co-registered ultrasound images, which used to extract manually. This manual procedure was replaced with a semi-automatic image segmentation algorithm. This simple and light computation algorithm can provide accurate tumor size and location information with minimum user input, thus reconstructing the optical images faster. The algorithm also estimates the chest wall depth, which can be used in further improving the absorption coefficient estimation.

All these improvements make diffuse optical tomography a more useful tool for breast cancer diagnosis and monitoring. Benefitting from the new improvements in user-friendliness, clinicians themselves can now directly reconstruct co-registered images, which was impossible with the previous versions. Once validated in large clinical trials and further improved, this technology will help to reduce unnecessary biopsies and provide for treatment monitoring in the near future.

In this work, a new version of photoacoustic tomography system was developed to improve ovarian cancer diagnosis in patients with ovarian abnormalities. The previous version demonstrated considerable potential by providing encouraging results from ex-vivo studies and a very limited number of in-vivo samples. However, that system's performance deteriorated over time and made it unusable for clinical trials. We proceeded to customize a commercial ultrasound system for photoacoustic applications; indeed, half of this Ph.D. research focused on system and data processing improvements for photoacoustic tomography. Python scripts were written to save co-registered US/PAT image and data from a customized commercial ultrasound system. Intuitively interfaced control software was developed to co-ordinate the functionalities of the US system, laser system, and ex-vivo sample holder. A customized probe holder was designed to accommodate optical fibers to illuminate the target and US transducers to record PAT signals. This system is easy to use and saves data and images for offline processing.

Data and images saved by the system were later processed to extract useful features for the automatic diagnosis of benign and malignant ovarian cancers. A robust classifier was obtained from several features extracted mainly from the saved RF data and combined with pathological information (CA-125). Promising results were obtained from the first 16 patient's data of a trial of total 40 patients.

4.2 Future Work

Several improvements have been achieved to make diffuse optical tomography and photoacoustic tomography more accessible for full clinical use. However, in the course of the clinical trials, we identified opportunities for future improvements.

In the diffuse optical tomography system, the control software does not receive any feedback regarding hardware states, e.g., the status of the laser light or PMT gain. Such hardware feedback is essential for the safe operation of the system, because the protocol requires that the laser light be turned on only when the probe is placed on the breast. However, a crash makes the software lose all track of the laser light's state, after which bad data could be collected or the light could remain on after the probe is removed from the breast. Because of the lack of hardware feedback, it also may be possible to turn off the system when the PMT gain is on, or when the laser light is turned on. Both actions are harmful to these expensive components. In the future, a firmware update will provide hardware feedback for safe operation.

Improvements are also required in the semi-automated segmentation algorithm. Although this algorithm works well for the available set of ultrasound breast tumor images, it may fail to correctly identify the tumor area for some complex cases. Because breast tumors can take any shape and size, conventional image segmentation may not be very successful in collecting tumor size and location information. Work is going on to apply machine learning to identify hidden patterns and thus to segment the tumor from the background with better accuracy. Applying machine learning will also make the algorithm fully-automated, and thus more user-friendly.

In the photoacoustic realm, PAT Doppler information will be collected using high-frequency laser pulses. This information will enable us to estimate the oxygen consumption in the tumor area,

which will be a diagnostic advantage because aggressive cancer cells require more oxygen than benign tumors. Therefore, high oxygen consumption in the tumor region will provide a good indication of tumor malignancy. Necessary software modifications have already made for data collection. Soon, the reconstruction algorithm will be ready for PAT Doppler estimation. Other features will be improved by using a better reference object to get better separation from the trained classifier. The resulting automated cancer diagnosis will assist radiologists in better detecting ovarian cancer.

List of Publication:

[1]   A. Mostafa, Q. Zhu, and C. Siegel, "Co-registered ultrasound Doppler with ultrasound and photoacoustic imaging to improve delineation of ovarian lesion for photoacoustic imaging," in *Photons Plus Ultrasound: Imaging and Sensing 2019*, 2019, p. 192.

[2]   G. Yang, E. Amidi, S. Nandy, A. Mostafa, and Q. Zhu, "Optimized light delivery probe using ball lenses for co-registered photoacoustic and ultrasound endo-cavity subsurface imaging," *Photoacoustics*, vol. 13, pp. 66–75, 2019.

[3]   A. Mostafa, S. Nandy, E. Amidi, and Q. Zhu, "Dual-mode photoacoustic and ultrasound system for real-time in-vivo ovarian cancer imaging," *Photons Plus Ultrasound Imaging Sens. 2018*, no. February, p. 158, 2018.

[4]   H. Vavadi *et al.*, "Compact ultrasound-guided diffuse optical tomography system for breast cancer imaging," *J. Biomed. Opt.*, vol. 24, no. 02, p. 1, 2018.

[5]   S. Nandy *et al.*, "Evaluation of Ovarian Cancer: Initial Application of Coregistered Photoacoustic Tomography and US," *Radiology*, no. 18, p. 180666, 2018.

[6]   H. Vavadi *et al.*, "A calibration method for diffuse optical tomography based on extracted target depth and size from Ultrasound images," in *Optics InfoBase Conference Papers*, 2018, vol. Part F90-O.

[7]   A. Mostafa, S. Nandy, E. Amidi, and Q. Zhu, "Dual-mode photoacoustic and ultrasound system for real-time in-vivo ovarian cancer imaging," in *Progress in Biomedical Optics and Imaging - Proceedings of SPIE*, 2018, vol. 10494.

[8]   H. Vavadi *et al.*, "Compact ultrasound-guided diffuse optical tomography system for breast cancer imaging," *J. Biomed. Opt.*, vol. 24, no. 2, pp. 021203-1–9, 2018.

[9]   F. Zhou, A. Mostafa, and Q. Zhu, "Improving breast cancer diagnosis by reducing chest wall effect in diffuse optical tomography," *J. Biomed. Opt.*, vol. 22, no. 3, p. 036004, 2017.

[10]   H. Vavadi *et al.*, "Preliminary results of miniaturized and robust ultrasound guided diffuse optical tomography system for breast cancer detection," *Prog. Biomed. Opt. Imaging - Proc. SPIE*, vol. 10059, pp. 2–7, 2017.

[11]   A. Mostafa, H. Vavadi, K. M. S. Uddin, and Q. Zhu, "Diffuse optical tomography using semiautomated coregistered ultrasound measurements," *J. Biomed. Opt.*, vol. 22, no. 12, p. 1, 2017.

[12]   F. Zhou, A. Mostafa, and Q. Zhu, "Improving breast cancer diagnosis by reducing chest wall effect in diffuse optical tomography," *J. Biomed. Opt.*, vol. 22, no. 3, p. 036004, 2017.

[13]   K. M. S. Uddin, A. Mostafa, M. Anastasio, and Q. Zhu, "Two step imaging reconstruction using truncated pseudoinverse as a preliminary estimate in ultrasound guided diffuse optical tomography," *Biomed. Opt. Express*, vol. 8, no. 12, p. 5437, 2017.

[14]   H. Vavadi *et al.*, "Preliminary results of miniaturized and robust ultrasound guided diffuse optical tomography system for breast cancer detection," in *Progress in Biomedical Optics and Imaging - Proceedings of SPIE*, 2017, vol. 10059.

[15]   A. Mostafa, H. Vavadi, K. M. S. Uddin, and Q. Zhu, "Diffuse optical tomography using semiautomated coregistered ultrasound measurements," *J. Biomed. Opt.*, vol. 22, no. 12, 2017.

[16]   F. Zhou, A. Mostafa, and Q. Zhu, "Improving breast cancer diagnosis by reducing chest wall effect in diffuse optical tomography," in *Progress in Biomedical Optics and Imaging - Proceedings of SPIE*, 2017, vol. 10043.

[17]   C. Xu *et al.*, "Ultrasound-guided diffuse optical tomography for predicting and monitoring neoadjuvant chemotherapy of breast cancers: Recent progress," *Ultrason. Imaging*, vol. 38, no. 1, pp. 5–18, 2016.

[18]   S. Nandy, A. Mostafa, P. D. Kumavor, M. Sanders, M. Brewer, and Q. Zhu, "Characterizing optical properties and spatial heterogeneity of human ovarian tissue using spatial frequency domain imaging," *J. Biomed. Opt.*, vol. 21, no. 10, p. 101402, 2016.

[19]   A. Mostafa, H. Vavadi, and Q. Zhu, "Extraction of tumor features from ultrasound images for diffused optical tomography reconstruction," in *Optics InfoBase Conference Papers*, 2016.

[20]   H. Vavadi, C. Xu, A. Mostafa, and Q. Zhu, "Automated data selection method for diffuse optical tomography to improve the robustness of breast cancer detection," in *Optics InfoBase Conference Papers*, 2016.

[21]   S. Nandy, A. Mostafa, P. D. Kumavor, and Q. Zhu, "Application of spatial frequency domain imaging for characterizing wide field tissue optical heterogeneity," in *Optics InfoBase Conference Papers*, 2016.

[22]   A. Mostafa, T. Khan, and K. Wahid, "An improved YEF-DCT based compression algorithm for video capsule endoscopy," in *2014 36th Annual International Conference of the IEEE Engineering in Medicine and Biology Society, EMBC 2014*, 2014.

[23]   S. Nandy, A. Mostafa, P. D. Kumavor, and Q. Zhu, "Application of spatial frequency domain imaging for characterizing wide field tissue optical heterogeneity," in *Optics InfoBase Conference Papers*, 2014.

[24]   A. Mostafa, H. Vavadi, and Q. Zhu, "Extraction of tumor features from ultrasound images for diffused optical tomography reconstruction," in *Optics InfoBase Conference Papers*, 2014.

[25]   H. Vavadi, C. Xu, A. Mostafa, and Q. Zhu, "Automated data selection method for diffuse optical tomography to improve the robustness of breast cancer detection," in *Optics InfoBase Conference Papers*, 2014.